Stony Brook University

SAPHIRE (Scintillator Avalanche Photoconductor with High Resolution Emitter Readout) for low dose x-ray imaging

A Dissertation Presented

by

Dan Li

to

The Graduate School

in Partial Fulfillment of the Requirements

for the Degree of

Doctor of Philosophy

in

Physics

Stony Brook University

MAY 2009

STONY BROOK UNIVERSITY

The Graduate School

Dan Li

We, the dissertation committee for the above candidate for the

Doctor of Philosophy degree, hereby recommend

acceptance of this dissertation.

Wei Zhao, Ph.D., Dissertation Advisor
Associate Professor, Department of Radiology

Thomas T.S. Kuo, Ph.D., Chairperson of Defense
Professor, Department of Physics and Astronomy

Barbara Jacak, Ph.D.
Professor, Department of Physics and Astronomy

Chris J. Jacobsen, Ph.D.
Professor, Department of Physics and Astronomy

Anthony R. Lubinsky, Ph.D.
Assistant Professor, Department of Radiology

This dissertation is accepted by the Graduate School

Lawrence Martin
Dean of the Graduate School

Abstract of the Dissertation

SAPHIRE (Scintillator Avalanche Photoconductor with High Resolution Emitter Readout) for low dose x-ray imaging

by

Dan Li

Doctor of Philosophy

in

Physics

Stony Brook University

2009

The goal of this dissertation work is to investigate the feasibility of an indirect flat-panel imager (FPI) with programmable avalanche gain and field emitter array (FEA) readout for low dose x-ray imaging with high spatial resolution. It is made by optically coupling a structured x-ray scintillator, Cesium Iodide (CsI), to a thin layer of amorphous selenium (*a*-Se) avalanche photoconductor called HARP (high-gain avalanche rushing photoconductor). The charge image created by HARP is read out by electron beams

generated by the FEA. The proposed detector is called SAPHIRE (Scintillator Avalanche Photoconductor with High Resolution Emitter readout).

Compared to existing Active Matrix FPI (AMFPI), one of the SAPHIRE's advantages is its programmable gain g_{av}, which ensures a wide dynamic range. This gain depends on both *a*-Se thickness and the applied internal electric field E_{Se}. By varying E_{Se}, high g_{av} can be applied for low dose applications (e.g., fluoroscopy or tomosynthesis) to achieve x-ray quantum noise limited performance. g_{av} can be turned off at high dose (e.g., radiography) to avoid signal saturation. Our investigation shows the detective quantum efficiency (DQE) can be enhanced to theoretical limit with proper avalanche gain.

Because of the presence of avalanche gain, a high resolution type of CsI (Tl), which has not been widely used in indirect FPI due to its low light output, can be used to improve the high spatial frequency performance. The lateral spread of the electron beam, emitted with an oblique angle from FEA, was investigated with three different electron-optical designs: mesh-electrode-only, magnetic focusing, and electrostatic focusing. The design of electrostatic focusing was found to be the best method to satisfy the requirements of small pixel size (50 μm) and excellent spatial uniformity.

The temporal performance, i.e., lag, of SAPHIRE was also investigated. It is found that dominant lag source is the energy spread of the electron beams from the FEA, i.e. beam discharge lag. Three contributing factors were analyzed. Lag calculation was performed using FEA parameters of two prototype HARP-FEA image sensors and the results were compared with experimental measurements. Excellent agreement was observed for both prototype sensors. Strategies for reducing lag in SAPHIRE were

proposed and analyzed. The first frame lag can be reduced to ~ 4%, which is comparable to state-of-the-art real-time x-ray AMFPIs.

Finally, an x-ray imaging investigation was performed using a prototype optical HARP-FEA image sensor. The dynamic range, spatial resolution and image noise were measured, and the results demonstrated the advantages of SAPHIRE.

To my grandma and my parents

Contents

List of Acronyms

2-D	Two-Dimensional
***a*-Se**	Amorphous Selenium
Al	Aluminum
AMFPI	Active Matrix Flat Panel Imager
As	Arsenic
BACC	Beam Acceptance Characteristic Curve
BSD	Ballistic electron Surface emitting Device
CCD	Charge-Coupled Device
CdZnTe	Cadmium Zinc Telluride
CeO_2	Cerium Dioxide / Cerium Oxide
CR	Computed Radiography
CsI	Cesium Iodide
CNT	Carbon Nanotube
CT	Computed Tomography
DC	Direct Current
DQE	Detective Quantum Efficiency
EHP	Electron Hole Pair
FE	Field Emitter
FEA	Field Emitter Array

FED	Field Emission Display
FPI	Flat Panel Imager
FPD	Flat Panel Detector
HARP	High Avalanche Rushing amorphous Photoconductor
HEED	High-efficiency Electron Emission Device
HgI_2	Mercuric Iodide
HR	High Resolution type
IEC	International Electro-technical Commission
ITO	Indium Tin Oxide
kVp	Peak Kilo-Voltage
LCD	Liquid Crystal Display
LiF	Lithium Fluoride
LSF	Line Spread Function
MIM	Metal-Insulator-Metal emitter
MIS	Metal-Insulator-Semiconducotr emitter
Mo	Molybdenum
MOSFET	Metal-Oxide-Semiconductor Field Effect Transistors
MRI	Magnetic Resonance Imaging
ND	Neutral Density
PbI_2	Lead Iodide
PD	Photodiode
PET	Positron Emission Tomography
PMMA	Polymethyl-Methacrylate

PSF	Point Spread Function
QE	Quantum Efficiency
Rh	Rhodium
SAPHIRE	Scintillator Avalanche Photoconductor with High Resolution Emitter Readout
Sb_2S_3	Antimony Trisulphide
SCE	Surface-Conduction electron Emitter
SHARP	Scintillator-HARP
Si	Silicon
SPECT	Single Photon Emission Computed Tomography
TFT	Thin Film Transistor
Tl	Thallium
TlBr	Thallium Bromide
TOF	Time of Flight
W	Tungsten
WSS	Wide-Sense Stationary
XRII	X-Ray Imaging Intensifier

List of Figures

List of Tables

Acknowledgments

I would like to thank my advisor, Prof. Wei Zhao. Her profound knowledge and immense creativity have been the best resource for my graduate studies at Stony Brook University. Without her patience, encouragement and guidance, I would not have been able to finish this dissertation. The high level of professionalism that she demonstrated in her teaching and research will continue to serve as a model for me in my future development.

I would also like to thank the rest of my dissertation committee – Barbara V. Jacak, Chris Jacobsen, Thomas T.S. Kuo and Anthony Rick Lubinsky - for their precious time and valuable suggestions.

I benefited much from discussions with Bo Zhao, Jennifer Segui, Joerg Lehnert, Yue-Houng Hu, Jiong Chen. I appreciate their insight. I also deeply thank A. R. Lubinsky for his valuable suggestions and extensive comments. I also gratefully acknowledge the helpful discussion from Drs. Randy Luhta, Geordi Pang and John A. Rowlands. I would also like to acknowledge the stimulating scientific discussion with Dr. N. Egami from NHK Science and Technical Research Laboratory and the help with the experimental work from Dr. Y. Takiguchi, M. Nanba, Y. Honda, Y. Ohkawa, M. Kubota and K. Tanioka from NHK Science and Technical Research Laboratory and K. Suzuki and T. Kawai from Hamamatsu Photonics. I also thank Yue-Houng Hu for proofreading the manuscript.

Finally, I deeply thank my grandma and parents for their love and support during these years I'm abroad. I dedicate this dissertation to them.

Chapter 1

Introduction

During the twentieth century, medical imaging has seen vast progress and a series of revolutionary changes, which are driven by the development of underlying sciences and technologies as well as the needs of healthcare. Besides the conventional film/screen x-ray imaging, various modalities, such as computed tomography (CT), nuclear magnetic resonance imaging (MRI), Doppler ultrasound imaging, positron emission tomography (PET) and single photon emission computed tomography (SPECT), are undergoing rapid and successful development, both technologically and commercially, and have become powerful imaging tools for radiologists. These changes are partly owed to the proliferation of more developed and widely used computational resources and data communications, which have become less expensive and more powerful.

Although these new modalities have found their positions in medical diagnosis, the classical x-ray projection radiography itself also continues a trend of tremendous progress. Commercial computed radiography (CR) has been used since the 1980s and has steadily reduced in both size and cost. Nearly one hundred years after the discovery of x-rays by

German physicist Wilhelm C. Röntgen, conventional x-ray imaging technologies are being challenged by the emerging technology of flat panel digital x-ray detectors. These digital imaging technologies have been applied to previously unexploited physical potentials as well as for practical applications such as image archiving and transmission. These revolutionary changes are driven by the expanding information technology infrastructure in medicine as well as the need to provide health care to an increasing number of people efficiently. Research is now concentrated on the development of flat panel digital detectors whose possible applications range from digital mammography (image of breast) to conventional diagnostic radiography and fluoroscopy. Further development will lower the cost of the detectors and increase the availability of diagnostic digital imaging. Therefore, the information transition in a completely digital medical imaging environment will deliver better tools for patient care.

Among these applications, digital mammography has generated extensive attentions since breast cancer is the most commonly diagnosed malignancy in American women and the second leading cause of cancer death (second to lung cancer) [4, 5]. Based on reports from American Cancer Society, in the year of 2008, there are 182,460 new cases of female cancer, which is about 27.2% of total new cases of cancer, and there are 40,480 estimated death among those females. These numbers are up from 178,480 (26.3%) and 40,460 in the year of 2007, respectively [6].

The causes for this disease are largely unknown. Therefore, early detection and treatment are the only methods for reducing mortality from breast cancer. X-ray mammography means imaging a compressed breast with a low-energy x-ray beam, which has been the standard breast screening method and currently the most effective method

for early detection of breast cancer, i.e., when the cancer is in situ or minimally invasive. Statistics have shown that although the incidence rates of invasive female breast cancer for all races combined have been consistently increased since 1980, the mortality rate has significantly decreased by 2.2% annually [7], partially thanks to the development of x-ray mammography. Statistics show that on average, mammography can detect 80 - 90 % of breast cancers in women without symptoms. Sources have shown that mammography has reduced the mortality rate due to breast cancer by 20 - 30 % [8-10].

Our research will be focused on (but not limited to) x-ray digital mammography detector. In this chapter, I will first describe x-ray production and x-ray interaction with matter as well as the typical x-ray spectrum. Then I will introduce the current status of x-ray digital mammography detectors and their limitations, as well as the basic requirements for medical imaging systems. Finally, I will propose our detector structure and describe its operating principles and present basic image quality metrics for digital systems. At the end of this chapter, a basic outline of this dissertation is given.

1.1 X-ray production and interaction

1.1.1 X-ray production

X-rays can be produced by several different methods, such as by synchrotrons, by channeling sources, by free electron lasers, etc. However, in most radiology departments around the world, the vast majority technology used for x-ray production is the standard x-ray tube, which emits both bremsstrahlung and characteristic x-rays.

Bremsstrahlung radiation is produced when an electron (or other charged particle) incident upon a target (e.g. tungsten (W)) interacts with the nuclei of that target. The

electron interacts with the electric field generated by the nucleus of target atoms and experiences a loss in velocity, which results in the radiation of electromagnetic energy. Most of electrons pass through the atomic electric field with a grazing incident angle and give off only a small fraction of their kinetic energy to the resulting x-ray photons. On occasion, an electron may interact with the atomic nucleus and give up almost all of its kinetic energy to produce x-ray photons. Thus, the theoretical energy distribution of bremsstrahlung spectrum from a target produced by a mono-energetic beam of electrons is mathematically described as

$$\Psi(E) = cZ(E_{\max} - E) \tag{1.01}$$

where $\Psi(E)$ is the energy distribution of bremsstrahlung x-ray spectrum, E is the energy of x-ray photons, c is a constant, Z is the atomic number of the target, and $E_{\max}$ is the kinetic energy of the incident electron.

Characteristic radiation occurs when electrons interact with the atomic electrons in the target material. In the classic Bohr model of the atom, when an incoming electron interacts with an inner-shell atomic electron and imparts enough energy upon it to cause ejection, an outer-shell electron will subsequently fill the vacancy with a process resulting in the emission of characteristic x-ray photons, which have an energy equivalent to the difference between the binding energies of the two electron shells. The characteristic x-rays resulting from electrons transitioning between atomic shells are unique to the target atom. For example, tungsten atom has electrons roughly at energy level of 70 keV, 11 keV, and 3 keV for K-, L-, and M-shell electrons, respectively. Target of W may give off characteristic x-rays with energy of 59 keV (called K_α, from L-shell to K-Shell) and of 67 keV (called K_β, from M-shell to K-Shell).

1.1.2 X-ray interaction with matter

There are several different types of interaction mechanisms for x-rays (and γ rays) to interact with matter. The types of interactions include the photoelectric effect, Rayleigh (coherent) scattering, Compton (incoherent) scattering, pair production and triplet production. These interaction mechanisms combine to produce attenuation of the incident x-ray photon beam as it passes through matter, as it follows the Lambert-Beers law:

$$N = N_0 e^{-\mu t}, \tag{1.02}$$

where N_0 and N are the numbers of x-ray photons before and after the interaction with matter of thickness, t. Here, the linear attenuation coefficient, μ, is the probability of interaction from all mechanisms and thus is the sum of the interaction probabilities of all the interaction types:

$$\mu = \tau + \sigma_r + \sigma_c + \pi + \gamma, \tag{1.03}$$

where τ is the attenuation coefficient for photoelectric effect, σ_r is the Rayleigh scatter attenuation coefficient, σ_c is the Compton attenuation coefficient, π is the pair-production attenuation coefficient, and γ is the triplet production coefficient. All of the above coefficients are energy-dependent. An example for carbon may be seen in Fig 1.01, which is the most common element in human body, and calcium in Fig. 1.02, which is one of the most important elements in bones. For calcium, the K edge (at 4.05 keV) is very obvious.

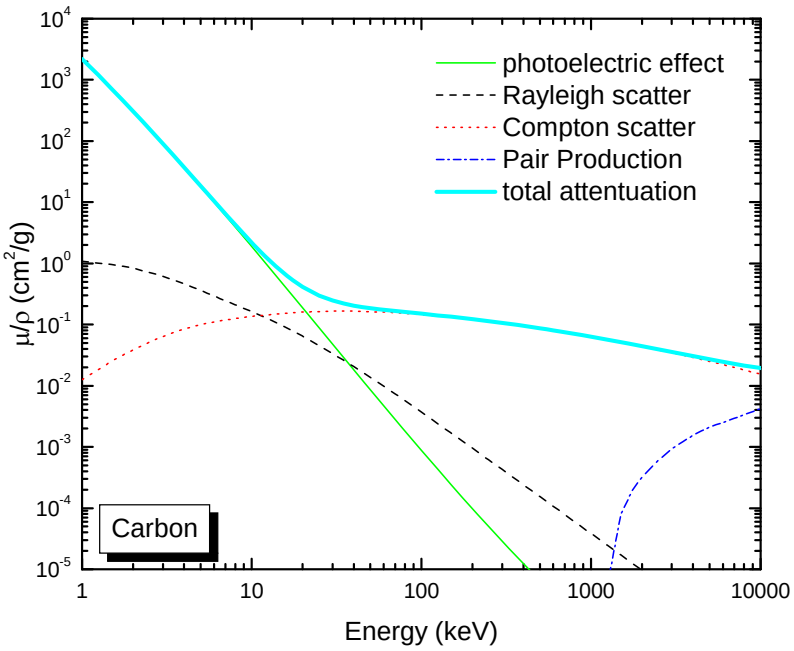

Figure 1.01: The mass attenuation coefficients for carbon as well as its components are plotted as a function of x-ray energy [11].

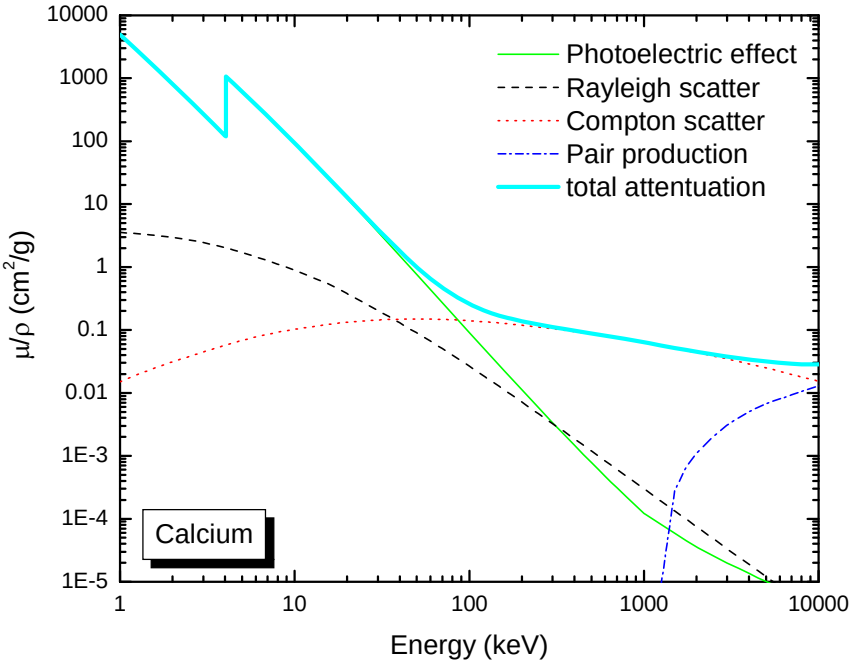

Figure 1.02: The mass attenuation coefficients for calcium as well as its components are plotted as a function of x-ray energy. The K edge (4.05 keV) is apparent [11].

1.1.3 X-ray spectrum

Both of Figs. 1.01 and 1.02 show that the attenuation coefficients generally degrade as x-ray photon energy increases. In the x-ray spectrum for medical diagnosis, which usually has x-ray energy up to 150 keV, pair production and triplet production will never happen. However, for different medical diagnosis purposes, the x-ray spectrum, determined by the x-ray tube target, peak kilo-voltage (kVp, i.e., the maximum energy of bombarding electrons), and filtration, must be carefully chosen.

To obtain a good contrast for anatomic structures, low energy x-ray photons are preferred, since the difference of x-ray attenuation coefficients for different anatomic structures are relatively large at low energies. On the other hand, low energy x-rays do not penetrate tissue as well as high energy x-rays and are easily absorbed by body tissue. A large amount of x-rays is required to obtain good contrast, which, in turn, increases the absorbed dose. Thus, the x-ray spectrum must be chosen on the type of diagnosis. Fig. 1.03 shows the measured x-ray attenuation coefficient of fibroglandular breast tissue, adipose tissue and infiltrating ductal carcinoma [8, 12] as well as bone [11] For chest radiography or fluoroscopy, W is an appropriate choice as an x-ray tube target with a kVp of 70 ~ 150 V; for mammography, the target is typically molybdenum (Mo) or rhodium (Rh) and the kVp is generally 30 ~ 40 V. The x-ray spectrum from x-ray tube is usually filtered by W, Mo, Rh, Aluminum (Al) or Polymethyl-methacrylate (PMMA). These filters absorb most low energy x-ray photons but allow the x-rays at characteristic energies to propagate, thus increasing the x-ray beam quality. This filtration is also a process of beam hardening.

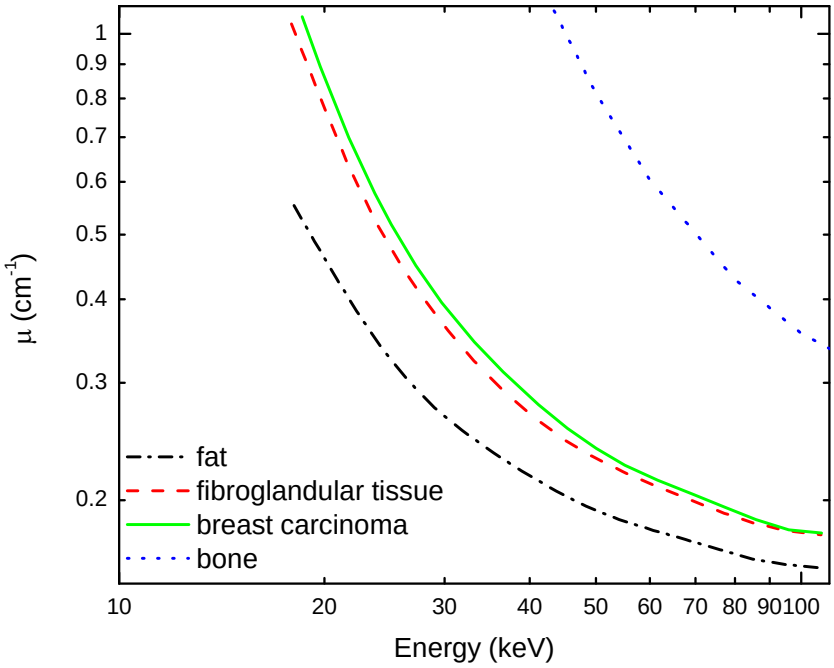

Figure 1.03: Linear attenuation coefficients of fat, fibroglandular tissue, breast carcinoma and bone, for x-ray, are plotted as function of x-ray photon energy [11, 13].

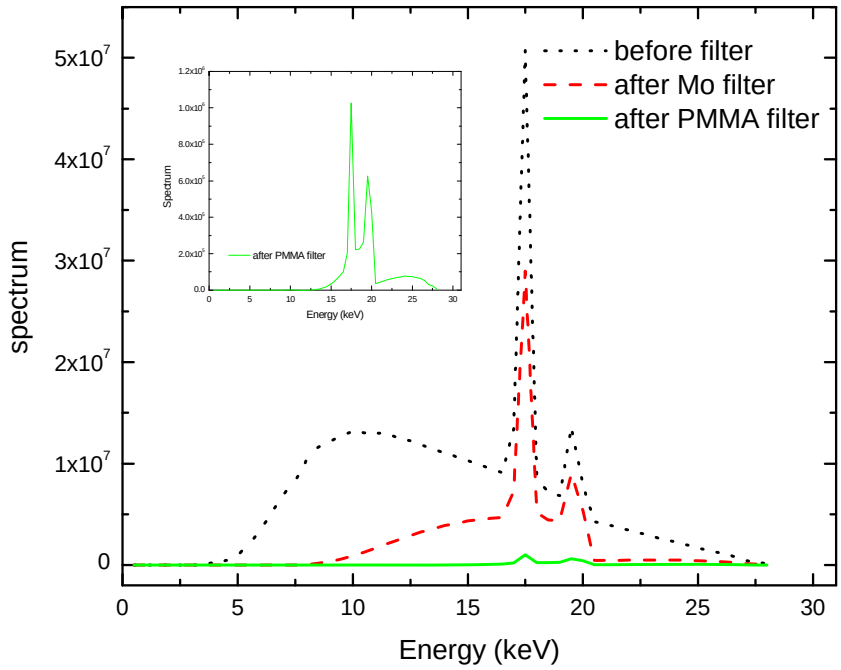

Figure 1.04: Spectrum used for mammography. The three curves show the spectrums before filtration, after 30-μm-Mo filter and final spectrum after 4-cm-PMMA filter, which is also shown the figure inside. The two peaks stand for characteristic x-rays which happen at 17.4 keV (K_α) and 19.6 keV (K_β).

For the research we focused on, we chose a spectrum of 28 kVp with a Mo/Mo target filter combination, through 4cm PMMA ("28kVp Mo/Mo, 4cm PMMA") for mammographic applications and RQA5 for general radiography/fluoroscopy (R/F). The "28kVp Mo/Mo, 4cm PMMA" for mammographic application supplies a 28 kV potential on an x-ray tube (Mo as anode) and the output x-rays are filtered by 30-μm of Mo with an additional 4-cm PMMA layer. The spectra are shown in Fig. 1.04. From the spectrum without filtration, we see most of low energy x-rays (< 10 keV) are missing, which is due to the self attenuation by metallic structures of the tube. Characteristic x-rays are shown on the spectrum as the two peaks, which occur at K_α (17.4 keV) and K_β (19.6 keV). The Mo filter reduces the bremsstrahlung radiation, especially for the x-ray photons with energy above the Mo K-edge (20 keV). The PMMA also reduces the low energy x-rays. The two electrons in the K-shell, in actuality, retain two different energies. This results in two K_α peaks, which have a slight energy difference. This is not important for medical x-ray spectrum and usually cannot be seen. RQA5 is one of the x-ray beam quality standards recommended by international electrotechnical commission (IEC). It supplies 70 kV of direct current (DC) on x-ray tube which has W as anode (target) and 23-mm Al of filtration. The spectrum is shown in Fig. 1.05. Except for the self-absorbed low energy x-ray photons, the characteristic x-rays K_α (~ 59 keV) and K_β (~ 67 keV) are not visible, since its K-edge is present at about 70 keV. These two spectrums are used to evaluate our detector SAPHIRE, particularly for signal detection.

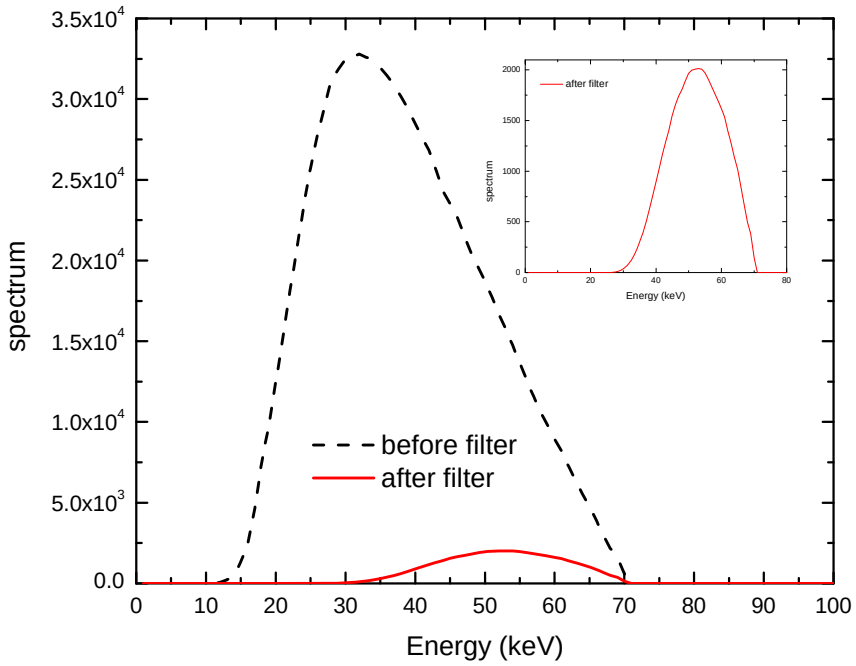

Figure 1.05: RQA5 spectrum. The two curves show the spectrum before and after 23-mm-Al filtration. RQA5 spectrum is the final one which is also shown inside the figure.

1.2 Mammography

1.2.1 Conventional screen/film mammography

Before we discuss digital mammography, it is important to note that conventional screen/film mammography is still a valuable tool for detection and radiological diagnosis of breast cancer. Conventional screen/film mammography has several advantages, including relatively inexpensive price and a high spatial resolution (20 line-pairs/mm). However, it also has limitations: (1) it has a non-linear response to x-ray exposure and the image contrast is low, particularly for patients whose breasts contain large amounts of radiographically dense, fibro-glandular breast tissue, i.e., the dense breast [14, 15]; (2) it is not x-ray quantum noise limited, especially at high spatial frequencies where the noise is dominated by film granularity and screen structure [13].

1.2.2 Digital mammography

Today screen/film systems are gradually being replaced by digital mammography detectors, which provide an electric signal proportional to the intensity of x-ray transmitted. They have received extensive investigation and demonstrated increased dynamic range and improved the diagnosis in women with dense breasts [13, 16, 17]. Except for scanning-slot digital mammography systems based on charge coupled devices (CCD) [18, 19], the majority of existing digital mammography detectors are active matrix flat-panel imagers (AMFPI) [20-22], which use a two dimensional (2-D) array of thin film transistors (TFT) to read out a charge image generated by an x-ray sensor [23]. Based on the method used for the detection of x-ray, the detectors can be classified as two categories: direct or indirect detection. In a direct detector, the recorded information (electric charge, current or voltage) results directly from ionization of the atoms in the detector. For example, Fig. 1.06 shows a schematic concept of a solid state direct detection flat panel imager (FPI), also sometimes called a flat panel detector (FPD). A uniform layer of amorphous selenium (*a*-Se), which has attracted substantial amount of interest as a photoconductor for x-ray imaging, is placed between two electrodes in a sandwich structure. The potential difference between these two electrodes will produce the necessary electric field (~ 10 V/μm) so charges of signal can be generated as x-ray hits. In this example, the bottom electrode is pixilated, and read out by a 2-D TFT array: scanning control turns on the gate (marked as "G" in Fig. 1.06) of the TFT row by row, and multiplexer reads out all data on that row simultaneously.

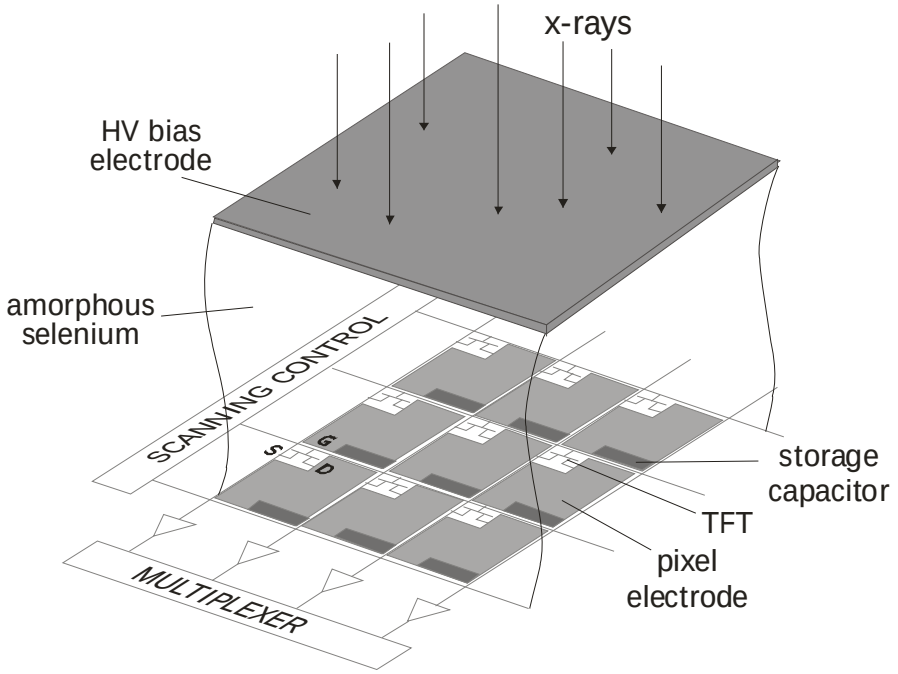

Figure 1.06: 3-D schematic showing the concept of direct flat panel imager. X-ray interacts with a photoconductor (e.g. *a*-Se) and generates negative and positive ions, which migrate to the opposite electrodes and produce signal data.

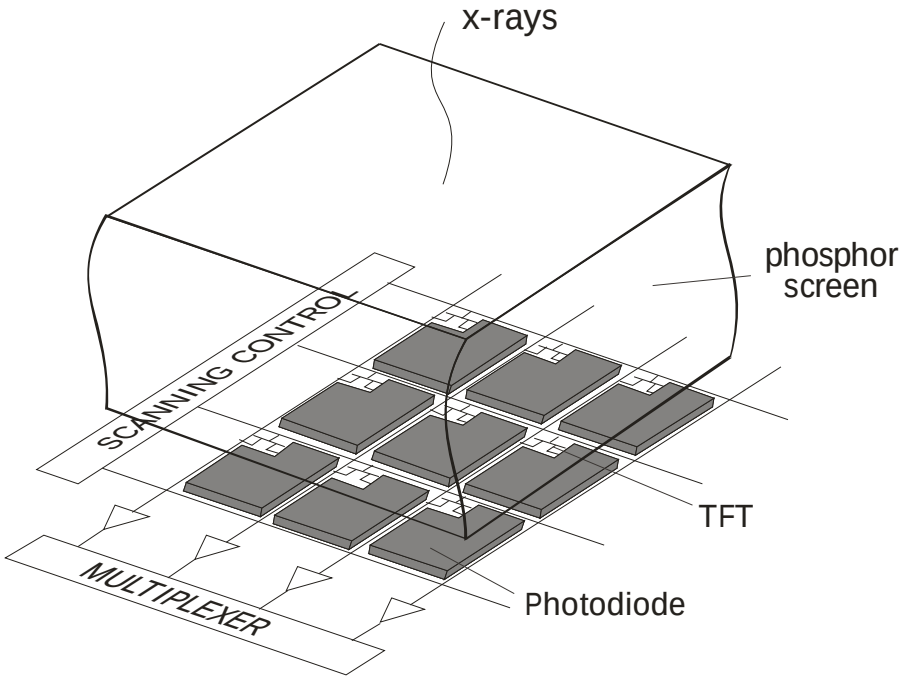

Figure 1.07: 3-D schematic showing the concept of indirect flat panel imager. X-ray interacts with a scintillator and produce light photons, which is then measured by the photo-detector.

An indirect detector system uses a phosphor/scintillator to convert x-rays to visible-light photons before the photons transmit, through optical diffusion, to a photo-detector such as a photodiode. Fig. 1.07 shows a schematic concept of an indirect AMFPI. A TFT is once again used here as the readout method. Although the TFT has been extensively used in FPIs and in other fields (such TFT liquid crystal display), we will see later it is not the only choice for digital mammography.

One of the advantages that the direct approach has over the indirect is the inherent image resolution. As the optical photons transmit through the phosphors, the optical diffusion may cause image blurring, which is usually the dominant source of blurring during imaging chain.

1.2.3 Limitations of current mammography detector

Although x-ray mammography is the most effective method for early detection of breast cancer, 10 % ~ 20 % may be missed even with the most recent advances in mammography [24]. The main reason that cancers are missed is because they are often obscured by radiographically dense, fibro-glandular breast tissue [14].

Meanwhile, because of their rapid readout speed and geometric accuracy, digital mammography detectors have generated interest in digital tomosynthesis [25, 26], where a series of images are taken quickly from different angles. Those images are then used to re-construct three dimensional (3-D) images of the breast to assist radiologists in the removal of "structured noise" and thus improve the accuracy of diagnosis. However, this presents a tremendous challenge for the detector: to generate quantum noise limited

images behind a dense breast with a dose a fraction (one tenth or less) of that used in screening mammography.

Although both of the direct or indirect AMFPI methods offer better image quality than screen-film or CR [27, 28], their imaging performance have not yet been fully optimized. Further improvement, especially in spatial resolution and low dose performance, is still possible and can lead to better clinical performance [8]. Existing mammography AMFPIs have the following two shortcomings: (1) the electronic noise degrades the imaging performance behind dense tissue in a low dose application. The spatial frequency dependent detective quantum efficiency, DQE(*f*), which describes the efficiency of an imaging detector in utilizing x-rays, is the gold standard for physical imaging performance of x-ray detectors. Previous researchers have shown that the DQE(*f*) for both direct and indirect AMFPI at ~ 1 mR of exposure behind dense tissue can be < 50 % of that at 10 mR exposure, which is about the mean exposure behind breast [29-31]. This suggests the detector is not x-ray quantum noise limited. This problem is exacerbated when pixel size is decreased or a low dose is used i.e. for tomosynthesis; (2) the pixel size currently used in mammography AMFPIs is about 70 ~ 100 μm. This size has an impact on the detection of the shape of micro-calcifications in breasts. It has not yet been known what pixel size, d_{el}, is optimal for digital mammography. However, it has been shown that with d_{el} = 100 μm, characterization of the shape of calcification is compromised, while d_{el} = 50 μm this information can be preserved [8].

To overcome the limitations above, several studies are currently being undertaken:

(1) The existing AMFPI is expected to be optimized by either increasing the signal or decreasing the electronic noise. The methods for increasing the signal include those to

develop continuous photodiodes [32, 33], those to optimize Cesium Iodide (CsI) for indirect AMFPIs [34], and those to increase the electric field in *a*-Se detectors for direct AMFPIs [35]. Although DQE(*f*) behind dense breasts can be theoretically improved by these changes when used in screening mammography applications [31], they will not be sufficient for tomosynthetic use or for a decreased pixel size (e.g., 50 μm). One method to decrease electronic noise is to introduce pixel amplification by adding two extra TFTs at each pixel, which can potentially lead to a twofold decrease in noise [36-38]. However, this improvement is still insufficient and may be extremely difficult to implement for the small pixel size needed for mammography.

(2) High conversion gain photoconductors are being developed for direct AMFPIs, including the promising candidate materials of Lead Iodide (PbI_2) [39] and Mercuric Iodide (HgI_2) [40, 41]. Both materials can provide x-ray to charge conversion gain which is about 5 ~ 7 times higher than that of *a*-Se [41]. This advantage makes it possible to build an AMFPI that is x-ray quantum noise limited for the low dose exposures used in tomosynthesis. These candidate materials, however, face two challenges. One is that the high gain results in the need for a large pixel storage capacitor (C_{st} > 10 pF) in order to hold the image charge generated in high exposure regions (e.g. near the skin line in screening mammography). This is impractical to manufacture for small pixel sizes, and a large C_{st} will significantly increase the pixel electronic noise, which eventually negates the advantage of signal gain at low exposures. The other challenge is that there is only one type of charge carrier in each instance (holes for PbI_2 and electrons for HgI_2) that has adequate range. This leads to a high probability of charge trapping in the photoconductors [42] and results in image artifacts (ghosting) [43]. Other materials, including Cadmium

Zinc Telluride (CdZnTe, or CZT) [44] and Thallium Bromide (TlBr) [45], have also been developed as potential x-ray photoconductors since both have higher atomic numbers and greater x-ray to charge conversion gain. However, they cannot provide additional avalanche gain.

1.3 SAPHIRE: our proposed detector

1.3.1 Structure and operational principles of SAPHIRE

Motivated by the continuing effort to improve upon digital mammography and the limitations of other methods, we proposed to investigate the feasibility of a new concept of indirect conversion flat-panel digital detectors with avalanche gain and field emitter array (FEA) readout, which is referred to as SAPHIRE (Scintillator Avalanche Photoconductor with High Resolution Emitter readout). The structure of the SAPHIRE concept is shown with the schematic drawing in Fig. 1.08. It consists of a thallium (Tl) doped needle-structured CsI scintillator, which is optically coupled (e.g. through fiber optics) to a uniform thin layer (4 ~ 25 μm) of avalanche *a*-Se photoconductor called HARP (High Avalanche Rushing amorphous Photoconductor). As shown in the cross-sectional view in Fig. 1.09, the optical photons emitted from the scintillator transmit through a transparent indium tin oxide (ITO) bias electrode of HARP and generate electron-hole pairs near the top interface of the HARP layer. Through carefully engineered blocking contacts, which prevent charge injection, a positive voltage is applied to the ITO electrode, and holes move towards the bottom (free) surface of the HARP and experience almost the identical avalanche multiplication under an electric field strength of $E_{Se} > 80$ V/μm [46, 47], which is an order of magnitude higher than that

typically used in direct *a*-Se x-ray detector. The holes form an amplified charge image at the bottom surface of HARP and are read out with the electron beams generated by a two-dimensional FEA, which is placed at a short distance, e.g. 1 mm, below the scintillator-HARP (SHARP) structure. The total amount of charge is measured by an amplifier connected on the ITO and forms the output signal.

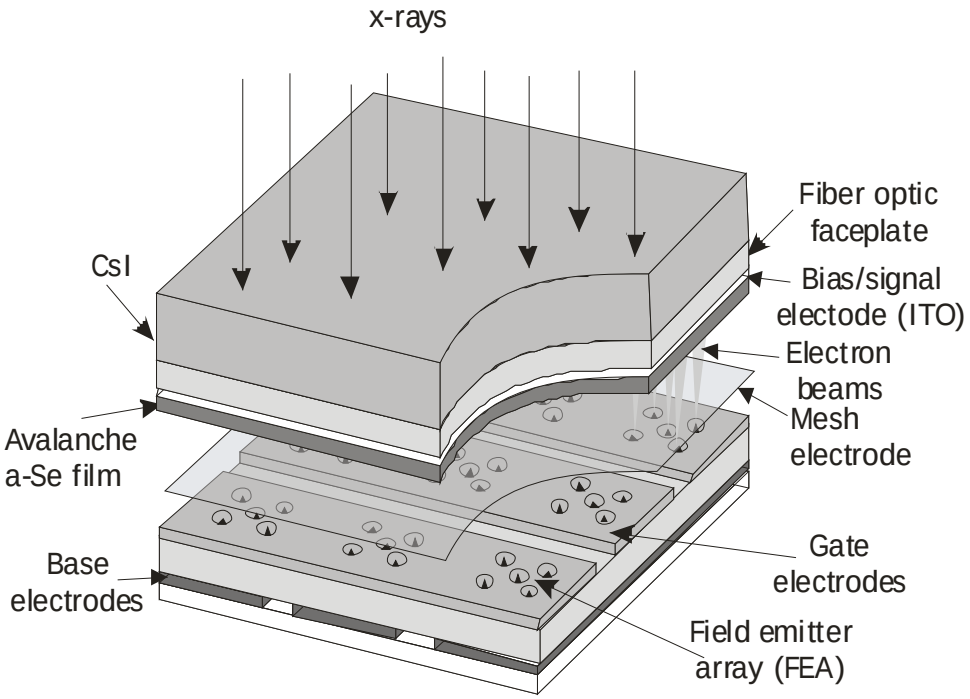

Figure 1.08: Schematics showing the concept of the proposed detector SAPHIRE: the side-view of main components of the detector. The figure is not to scale.

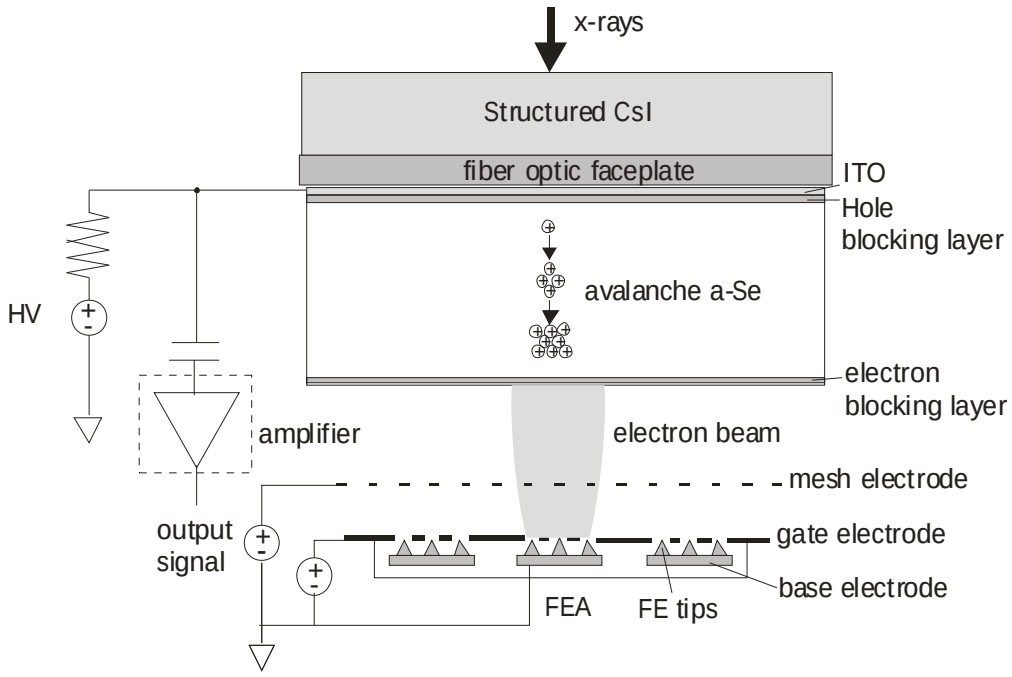

Figure 1.09: Schematics showing the concept of the proposed detector SAPHIRE: cross-sectional view showing the operating principles

The concept of electron beam readout is similar to that used in optical and x-ray vidicons [48], except that the FEA is a compact, two-dimensional source of electron beams, allowing the construction of the detector in the form of a FPI. As an emerging technology for large area flat-panel field emission displays (FED) [49], FEA has the potential to provide a smaller pixel size than that achieved with a TFT readout. As shown in Fig. 1.08, the field emitter (FE) tips (with spacing of ~1 μm) are connected to base electrodes arranged in columns, and rows of gate electrodes are used to control the field emission. The overlapping area between the base and gate electrodes defines the pixel size. Smaller pixel FEAs require thinner passive addressing lines and essentially no increase in cost while in TFT readout method, making smaller TFTs to reduce pixel size would result in exponential increase in cost. Sufficient FE tips can be included in a small pixel of d_{el} = 50 μm to provide sufficient emission current required by the wide dynamic range of medical images. Each pixel is addressed by applying a forward positive bias

potential (e.g., 60 V) between the gate and the base. This driving scheme is very similar to that used in passive matrix liquid crystal displays (LCDs). The main disadvantage of the passive driving scheme is the pulse delay due to load resistance and capacitance of each line. To alleviate this problem, active matrix FEA have recently been under development, where each pixel is addressed through a transistor [50, 51]. A mesh electrode, biased with positive potential, is inserted halfway between the FEA and HARP target to minimize the lateral spread of electron beams before they land on the free surface of the HARP target. The amount of charge required to return the bottom surface of the HARP target to ground (cathode) potential is measured by a charge amplifier connected to the ITO electrode to form the output signal. As will be discussed later in this dissertation, more sophisticated electron beam focusing methods are desirable to reach a pixel size of 50 μm.

All the detector components of SAPHIRE, including the CsI, the *a*-Se photoconductor and the FEA, can be fabricated into large area with moderate cost, than the detector can be assembled into the same thin and compact form as AMFPI. Although the operation of FEA requires vacuum, modern FED assembly technology allows the active area to be very near the edge of the detector, so that the dead space along the chest wall is minimal. By using an angle fiber optic faceplate to couple CsI to HARP, the dead space along the chest wall can be further reduced.

1.3.2 Advantages of SAPHIRE

Compared to existing AMFPI, SAPHIRE has the following advantages: (1) programmable avalanche gain, g_{av}, ensures a wide dynamic range. By changing the

electric field E_{Se}, high g_{av} can be applied for low dose applications (e.g. fluoroscopy or tomosynthesis) to achieve x-ray quantum noise limited performance, and turned off for high dose (e.g. radiography) to avoid detector saturation [52]; (2) FEA may provide smaller pixel sizes than what is possible with TFTs; (3) A high resolution (HR) type of CsI can be used because of the additional gain provided by HARP. HR type CsI has less Lubberts effect, i.e. depth dependent blur, which is the main source of DQE degradation at high spatial frequencies [3, 53]. Despite its resolution advantages, HR CsI has not been used widely in commercial indirect FPI due to its lower conversion gain, which makes the detector more susceptible to electronic noise at low exposure levels [54, 55]; (4) it has higher radiation resistance because FEA has no sensitive components; (5) it has a potentially higher readout speed and better temporal performance because both charge carriers in *a*-Se have adequate range and the probability of charge trapping is lower than PbI_2 or HgI_2 films.

The potential use of thick HARP layers (e.g., 500 μm) as direct x-ray detectors has been investigated and was found to be undesirable due to the depth dependence of avalanche gain and significant degrading Swank factor [56].

1.3.3 General requirements of x-ray imaging systems

As hundreds of years have passed for development of medical imaging acquisition and interpretation, radiologists are justifiably reluctant to stray too far, too quickly from their familiar approach. Definition of the important imaging parameters would be a good start. Although SAPHIRE is motivated to improve the performance of current mammographic detectors, its programmable gains and high readout speed make it also

appropriate for Radiography/Fluoroscopy detector. Table 1.01 shows priori requirements of SAPHIRE for the medical imaging systems, which is adopted from the one derived by J. A. Rowlands and J. Yorkston [23].

Table 1.01: Detector parameters for digital x-ray imaging systems

Clinical Task	Chest Radiography	Fluoroscopy	Mammography	Mammographic Tomosynthesis
Detector size (cm)	25 × 20	25 × 20	25 × 20	25 × 20
Pixel size (μm)	200 × 200	200 × 200	50 × 50	50 × 50
Number of pixels	1250 × 1000	1250 × 1000	5000 × 4000	5000 × 4000
Readout time (sec)	< 5	1 / 30	< 5	1/6 ~ ½
X-ray spectrum	RQA5	RQA5	28 kvp, Mo/Mo, 4cm PMMA	28 kvp, Mo/Mo, 4cm PMMA
Mean exposure (μR)	300	1	20000	2000
Exposure range (μR)	30 ~ 3000	0.1 ~ 10	1000 ~ 240000	100 ~ 24000
Noise level (μR)	6	0.1	60	10

1.4 Image quality metrics for digital systems

In order to assess the performance of these devices, it is necessary to consider the physical image quality parameters besides the observer's perceptual response. Here is a brief description of basic image quality metrics for digital systems we may use throughout this dissertation.

1.4.1 Linearity

The relationship between input intensity and output signal in an imaging system influences the range in which an appropriate image quality can be obtained. This relationship (response) is linear (with respect to the logarithm of incident intensity) in screen/film over approximately 1 to 2 orders of magnitude. In digital systems, the response is typically linear with respect to exposure over 3 to 4 orders of magnitude. The range of the highest to lowest response is usually called dynamic range of the system. The dynamic range for a digital system, we hope, is limited to practical issues of available digitization bits rather than an inherent limitation of the x-ray detection.

1.4.2 SNR, MTF, NPS and DQE

Signal to noise ratio (SNR) is one of the most basic metrics for image quality assessment and its importance was first recognized by Rose [57]. The Rose SNR is given by

$$\Delta \mathrm{SNR}_{Rose} = \frac{A(\Phi_b - \Phi_0)}{\sqrt{A\Phi_b}} = C\sqrt{A\Phi_b}\,, \qquad (1.04)$$

where Φ_0 and Φ_b are the mean quanta of the uniform object with area A and the uniform background. It is assumed that the background has uncorrelated quanta and the noise is Poisson distributed. Thus the noise is described by the standard deviation of $\sigma_b = \sqrt{A\Phi_b}$ and the contrast of the object is defined as $C = (\Phi_b - \Phi_0)/\Phi_b$. Rose's criterion states that the threshold of detectability of an object for humans is $\Delta \mathrm{SNR}_{Rose} \geq 5$ [57].

To compare the performance of imaging systems, characteristics curves based on Fourier analysis are proposed as useful metrics to determine the imaging performance of the system [58]. These characteristics curves include modulation transfer function (MTF),

noise power spectrum (NPS) and DQE. These characteristics measurements can be performed on the detector.

MTF measures the spatial resolution of the imaging system in the frequency domain. The spatial resolution in a system is "technically" the minimum distance between two objects which can still be distinguished as distinct objects. Of course, the shape of the object is important, thus, the shape of the response of the system to a delta-function is of the best utility. This response is called point spread function (PSF) and contains all of the deterministic spatial-transfer information of the system. The line spread function (LSF) is defined by

$$LSF(x) = \int_{y} PSF(x, y)dy\,, \tag{1.05}$$

which is usually more easily measured on the detector than the PSF. MTF is the Fourier transform of LSF, normalized by the MTF at the zero frequency:

$$MTF(f) = \frac{\left|FT(LSF(x))\right|}{\left|FT(LSF(x))\right|_{f=0}}\,. \tag{1.06}$$

Blurring sources for detector MTF depends on many factors. The interaction between the x-rays and detection media, e.g. scatter, is an inherent source of loss in the spatial resolution. In digital systems, the pixel size partially determines the shape of the MTF, which is the product of the inherent MTF and transmission function of the pixel. The pixel aperture function is usually a 2D Sinc function of the pixel size. For indirect digital detectors, the inherent MTF is usually poor due to the optical properties of the phosphor. For direct digital detectors, the inherent MTF is usually very high, therefore pixel size limits the spatial resolution.

NPS is the addition of independent noise sources. It is defined as the Fourier transform of the autocovariance of the signal $d(x)$, as

$$NPS(f) = \left| FT(K_d(x)) \right|, \tag{1.07}$$

where the autocovariance $K_d(x)$ is defined as

$$K_d(x) = \underset{x'}{E}\left\{ \Delta d(x') \times \Delta d(x'+x) \right\} \tag{1.08}$$

in an ergodic wide-sense stationary (WSS) system, which the digital imaging systems usually are. NPS for a 1D signal $d(x)$ has units of $d^2(x) \times x$.

The two most important sources of noise are x-ray quantum noise and electronic noise. Ideally quantum noise, with the characteristics of Poisson white noise, should be the dominant noise source. However, quantum noise may be contaminated by other noise sources such as electronic noise. This makes NPS exposure dependent. At low exposures, the NPS may become dominated by fixed pattern noise, i.e., electronic noise in a digital detector. This will subsequently cause degradation in DQE.

DQE is another useful quantity for imaging characterization. It describes the efficiency of the detector utilizing x-rays and transferring information, i.e., SNR through the system. Mathematically DQE is given by:

$$DQE(f) = \frac{\mathrm{SNR}_{\mathrm{out}}{}^2(f)}{\mathrm{SNR}_{\mathrm{in}}{}^2(f)}, \tag{1.09}$$

where for x-ray imaging systems, the $\mathrm{SNR}_{\mathrm{out}}$ is the output SNR, mainly determined by the gain, MTF and NPS. $\mathrm{SNR}_{\mathrm{in}}{}^2$ is the input SNR^2 and is equivalent to the incident x-ray quanta. More specifically, DQE is calculated from measured MTF and NPS by following equation:[58]

$$DQE(f) = \frac{k^2 MTF^2(f)}{NPS(f) q_0} \tag{1.10}$$

where q_0 is the incident x-ray quanta per unit area (in quanta mm^{-2}), and k is the measured sensitivity at a given exposure. DQE is a function of spatial frequency and has values within a range of 0 ~ 1, with higher values indicating better performance. Comparisons based on DQE can indicate which detector makes more efficient use of the incident photons. However, such comparison does not necessarily indicate which detector will produce a better image. For DQE to be a valid metric for comparing images produced by different detectors, $SNR_{in}(f)$ for the different systems must be equal. If different kVp settings are used or if the scatter conditions are different, comparisons based on DQE may be misleading [59]. Alternatively the quantification of image quality may use noise equivalent quanta (NEQ):

$$NEQ(f) = q_0 DQE(f) \tag{1.11}$$

NEQ is an absolute measure of image quality and directly related to image quality. In principle, NEQ can be used to compare an ultrasound system with a positron emission tomographic system [60].

1.5 Chapter Outline

In this chapter (Chapter 1), we briefly examined x-ray production, interaction with matter and x-ray spectrum. The basic modalities for breast imaging and current status of digital x-ray detectors were also reviewed. With the goal of enhancing the detector's low dose performance with high resolutions, we proposed our indirect FPI, SAPHIRE. Its structure and operational principles were described. Before we analyzed the details of

SAPHIRE, the basic requirement for the operational conditions as well as the image quality metrics for digital systems are given.

In Chapter 2, we will determine the optimal CsI-HARP combination. We will investigate the total gain in the HARP, the linearity, dynamic range, gain non-uniformity resulting from thickness non-uniformity. The effects of direct x-ray interaction with HARP are also investigated.

In Chapter 3, the spatial resolution of SAPHIRE is investigated. The spatial resolution in different components of SAPHIRE is analyzed. Three different electron beam focusing methods, i.e. mesh-electrode-only, magnetic focusing, and electrostatic focusing are proposed and theoretically studied. Parallel beam readout is also proposed to read out the information.

In Chapter 4, the temporal performance of SAPHIRE, i.e. lag and ghosting are investigated. The contributions to lag and ghosting from the three components of SAPHIRE are studied. The beam discharge lag, which is found to be the dominant source of lag, is investigated in details. Different factors are considered to be the reason for discharge lag and a theory is established and validated by the experiment. Also, we proposed several methods to improve its temporal performance.

In Chapter 5, we experimentally investigated a prototype HARP-FEA image sensor with magnetic focusing. Its linearity, spatial resolution, noise properties are validated by experiments. Its potential x-ray imaging performance is also experimentally studied with a combination of x-ray imaging intensifier (XRII).

In Chapter 6, we will give an overview on potential future work.

Chapter 2

Signal Detection

One of the advantages of SAPHIRE is its programmable gain made possible by the HARP layer, which can be turned on during low dose fluoroscopy or mammographic tomosynthesis to overcome electric noise, and turned off during high dose radiography to avoid pixel saturation. In this chapter, we will investigate the important design considerations for the combination of Scintillator and HARP (called SHARP), such as avalanche gain. To determine the optimal design parameters and operational conditions for HARP, we measured the avalanche gain and optical quantum efficiency of an 8-μm HARP layer, both of which are functions of electric field (E_{Se}) inside the *a*-Se. The results were used in a physics model of HARP as well as a linear cascaded model of the FPI to determine the following x-ray imaging properties in both the avalanche and non-avalanche modes as a function of E_{Se}: (1) total gain, which is the product of avalanche gain and optical quantum efficiency; (2) linearity; (3) dynamic range; (4) gain non-uniformity due to the thickness non-uniformity of HARP layer; and (5) effects of direct x-ray interaction in HARP.

2.1 Photo-charge generation mechanism inside *a*-Se

As a semiconductor, selenium has been a focus of research and commercial interest for the use as a photoconductor since its discovery and initial application in rectifiers and photocells in the last century. In the most recent development of *a*-Se technology, one of its most promising properties is that its avalanche multiplication occurs at extremely high electric fields (E_{Se} > 80 V/μm). It was Juska *et al* [46] who were first to observe the avalanche phenomenon in *a*-Se by measuring time-of-fight (TOF) signals in an *a*-Se layer sandwiched between two insulating layers. In avalanche mode, *a*-Se has been used as a target for ultra-high sensitivity HARP television cameras [61, 62]. Avalanche multiplication may provide extremely high sensitivity for optical light, up to 1000 times higher than the sensitivity of the Silicon (Si) based charge-coupled devices (CCDs). These HARP television cameras may be able to produce high definition imaging in low light conditions such as night shooting. It is not a long history for HARP to be proposed as an indirect photoconductive material for medical imaging [35, 53, 63].

2.1.1 Quantum efficiency

Quantum efficiency (QE) is defined by the number of free carriers generated per absorbed photon. Generally, the mechanism of photo-charge generation in *a*-Se is described by the Onsager dissociation mechanism [64, 65]. This has been proven experimentally by Pai and Enck [66]. In the Onsager model, every absorbed photon creates a single thermalized germinate electron-hole pair (EHP) which is bound by Coulomb attraction. The probability of EHP dissociation/recombination depends on the

initial separation (r_0) between the two thermalized charge carriers, and the strength of applied electric field, i.e., E_{Se}. For higher energy photons, i.e., smaller wavelength (λ), the initial separation will be larger and so the probability of dissociation for the bound pairs into free carriers will also be greater. A high E_{Se} help the charge carriers to overcome their mutual Coulomb attraction thus also increase the probability of dissociation.

Following the Onsager mechanism, the photo-generation quantum efficacy (η) in *a*-Se is dependent on E_{Se} and λ, and can be expressed by

$$\eta = \phi_0 \frac{kT}{qE_{Se}r_0} e^{-A} e^{-\frac{qE_{Se}r_0}{kT}} \sum_{m=0}^{\infty} \frac{A^m}{m!} \sum_{n=0}^{\infty} \sum_{l=m+n+1}^{\infty} \left(\frac{qE_{Se}r_0}{kT} \right)^l \frac{1}{l!}, \tag{2.01}$$

with

$$A = \frac{e^2}{4\pi\varepsilon\varepsilon_0 kT}. \tag{2.02}$$

where T is the absolute temperature, k is the Boltzmann constant, q is the elementary charge (to distinguish from the exponential sign "e"), ε is the relative static permittivity for HARP, ε_0 is the vacuum permittivity, r_0 is the characteristic thermalization length or the initial separation, which is wavelength dependent. ϕ_0 is defined as the efficiency of production of thermalized charge pairs per absorbed photon, and it is independent of E_{Se}. Pai and Enck showed that the room temperature measurement of η can be best fitted with the expression in Eq. 2.01 using ϕ_0=1 and r_0 in the range between 0.8 – 7.0 nm for λ values between 620 and 400 nm.

However, in the Onsager model, the external electric field is generally emphasized to play a role in the dissociation process. A higher external electric field is believed to be able to modify the density of states within band tails, influencing the photoconductive

properties of amorphous material. Furthermore, the Onsager model has not included the effect of impact ionization. Thus, it can only explain the initial production of EHPs. The final effective quantum efficiency (η*) should include avalanche multiplication phenomenon if necessary.

2.1.2 Impact ionization rate and avalanche multiplication

When the electric field in a semiconductor is increased above a certain value, the carriers can gain enough energy so that they can excite electron-hole pairs by impact ionization. The impact ionization rate is defined as the number of EHP generated by one carrier per unit distance traveled. It is obviously electric field dependent and is related to the threshold fields for carriers to overcome the deceleration effects of thermal, optical-phonon, and ionization scattering [67, 68]. Let us assume that electrons and holes have impact ionization rates, α and β, respectively. We also assume an *a*-Se layer with thickness of L and under an external electric field E_{Se}, as shown in Fig. 2.01. Consider one EHP which has been created at depth of x. In traversing an element of distance dx, the electron will create αdx ionization collisions on average when it moves up while the hole similarly will generate βdx EHPs when it passes down. These secondary pairs will start chains of ionization depending on where they are created. If $M(x)$ is the average final total number of EHPs generated resulting from one initial EHP created at x, we can write

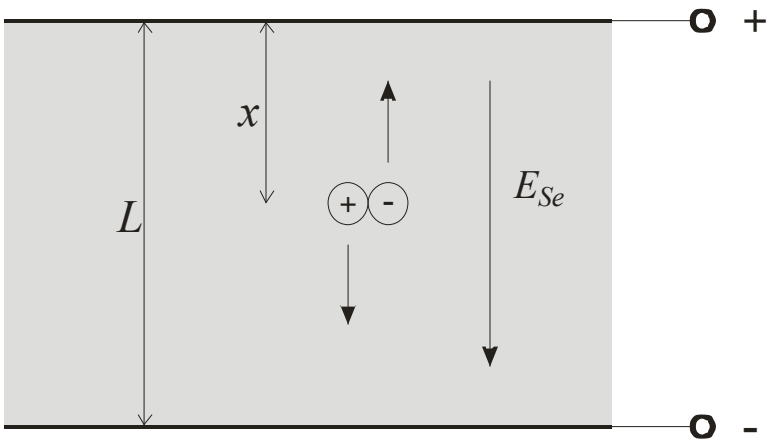

Figure 2.01: Schematics shows the process and parameters of avalanche phenomenon in *a*-Se layer with thickness of L and external electric field of E_{Se}. The initial EHP is assumed at depth of x.

$$M(x) = 1 + \int_0^x \alpha M(y)dy + \int_x^L \beta M(y)dy \,. \tag{2.03}$$

Its universal solution thus is given by

$$M(x) = \frac{\exp\left(-\int_x^L (\alpha - \beta)dy\right)}{1 - \int_0^L \alpha \exp\left(-\int_y^L (\alpha - \beta)dz\right)dy} \,. \tag{2.04}$$

In our case where E_{Se} is uniform everywhere, Eq. 2.04 can be simplified to

$$M(x) = \frac{(\beta - \alpha)e^{((\beta-\alpha)(L-x))}}{\beta - \alpha e^{(\beta-\alpha)L}} \,. \tag{2.05}$$

Eq 2.05 shows avalanche multiplication is depth dependent. The overall avalanche gain, g_{av}, is the average avalanche multiplication at different depths, the probability of which is determined by the Lambert-Beers law given by Eq. 1.02. So,

$$g_{av} = \frac{\mu(\alpha - \beta)(e^{\mu L} - e^{(\alpha-\beta)L})}{(\mu + \beta - \alpha)(e^{\mu L} - 1)(\alpha - \beta e^{(\alpha-\beta)L})}, \tag{2.06}$$

where μ is the linear attenuation coefficient for *a*-Se. Here we assume the photons are from the side of $x = 0$, i.e., the positive bias electrode. The details of derivation are given in Appendix A.

For optical photon absorption of *a*-Se, the values of μ are very large, compared with α and β. For example, $\mu = 3 \times 10^7$ / m for λ = 450 nm. This means that more than 95% of photons are absorbed within 0.1 μm of *a*-Se layer from the entrance side. Therefore,

$$g_{av} = M(0) = \frac{(\beta - \alpha) e^{((\beta-\alpha) d_{Se})}}{\beta - \alpha e^{(\beta-\alpha) d_{Se}}}, \tag{2.07}$$

where d_{Se} is the thickness of *a*-Se layer. The impact ionization rate, α and β, have previously been studied for multiple *a*-Se layers with thickness up to 4 μm [47]. They found both α and β show an exponential dependence on $1/E_{Se}$. Meanwhile, in *a*-Se the value of β is much greater than α since the drift mobility of holes (0.18 cm^2/Vs) is much higher than that of electrons (0.003 cm^2/Vs). It is important to note that in order for g_{av}, as defined in Eq. 2.07, to have a finite positive value, i.e., stable, avalanche, the condition of $\beta > \alpha e^{(\beta-\alpha) d_{Se}}$ must be satisfied. Under the assumption that the contribution of electrons to avalanche gain is negligible, Eq. 2.07 can be simplified to

$$g_{av} = e^{\beta d_{Se}}. \tag{2.08}$$

We will obtain the value of β by fitting experimental results.

The final effective quantum efficiency, i.e., the photosensitivity (η*), defined as the number of photo-carrier collected finally per absorbed photon, is given by

$$\eta^* = \eta \times g_{av}. \tag{2.09}$$

2.2 HARP structure

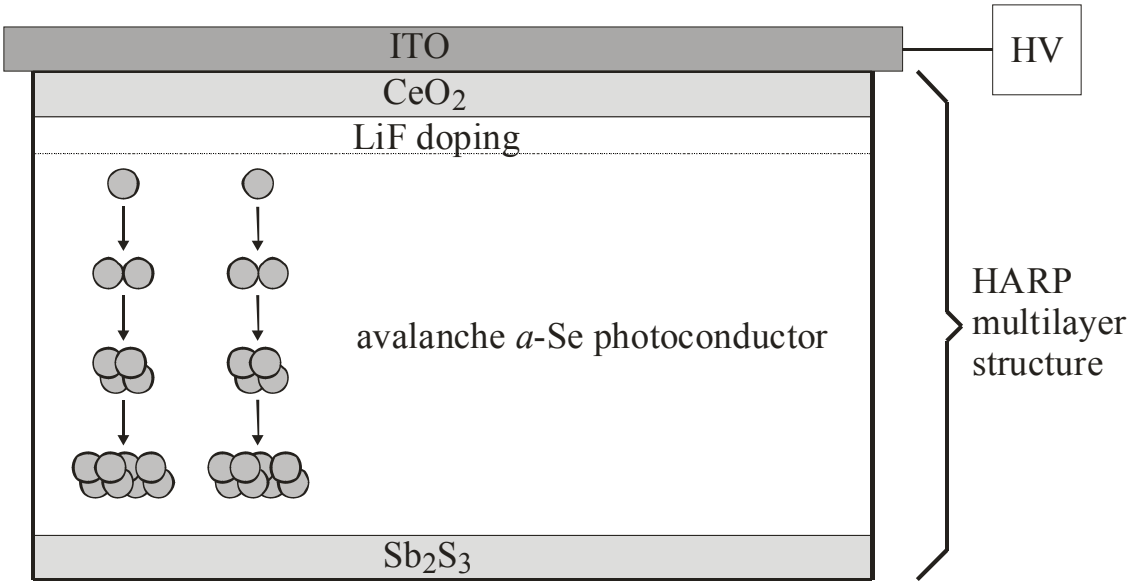

Figure 2.02: Schematics show the HARP multilayer structure. Only hole avalanche process is shown as an example in this figure. Electron avalanche process is not shown here.

Since the discovery of avalanche multiplication in *a*-Se over a decade ago, HARP tubes, which consist of a HARP layer read out with a scanning electron beam, have been commercialized for high sensitivity and high definition television applications. Stable and uniform avalanche multiplication has been observed with very little added noise [69]. The electric field (E_{Se} > 80 V/um), under which avalanche multiplication occurs, is an order of magnitude higher than that typically used in direct FPI incorporating thick *a*-Se layers. In order to sustain E_{Se} of this high magnitude without significant increase in dark current due to charge injection from the bias electrodes, blocking layers need to be developed for both electrode interfaces. A sample structure of the sandwiched *a*-Se HARP layer used in our experiment is schematically shown in Fig. 2.02. The top side is biased with a high voltage through transparent ITO electrode and the bottom is a free surface where charge images are formed and read out. A thin layer of antimony trisulphide (Sb_2S_3) is deposited on the bottom side to prevent electron injection from the negative bias electrode, which may be happen in a solid state detector with TFT readout

or scanning electron readout beams (e.g., from FEA). This electron injection blocking layer can reduce the emission of secondary electrons. Between the *a*-Se layer and the ITO electrode, a thin layer (~ 20 nm) of cerium dioxide (CeO_2) is interposed to make the hole-blocking contact stable and a thin layer of lithium fluoride (LiF) doped *a*-Se is used to block injection of holes from the ITO bias electrode. The intrinsic *a*-Se photoconductor is usually 0.5 – 35 μm thick depending on the desired avalanche gain and is doped with arsenic (As) to prevent *a*-Se from recrystallizing.

2.3 Experiment measurement of photosensitivity of HARP

The x-ray imaging performance of the indirect FPI with avalanche gain relies on the photosensitivity (η*) of HARP. Understanding its dependence on E_{Se} and HARP layer thickness, d_{Se}, is crucial for the proper choice of HARP design parameters and operational conditions for both the avalanche and non-avalanche modes. In this section, we will present the experimental method and results of the photosensitivity measurements of HARP. In section 2.1, we will present the theory of the effective quantum efficiency (photosensitivity), which is proportional to both the optical quantum efficiency η and the avalanche gain g_{av}, both of which are E_{Se} dependent. The theory and experimental data will then be used to determine η and g_{av} as a function of E_{Se} in the context of x-ray imaging.

2.3.1 Experiment method

The experimental setup for photosensitivity measurements is shown in Fig. 2.03. A grating monochromator was used to generate optical photons of a single wavelength (λ).

The values of λ used in our experiments ranged between 380-600 nm. The intensity of the output beam was attenuated by neutral-density (ND) filters. A beam-splitter was used to direct a fraction (90 %) of the attenuated beam to a silicon (Si) photodiode (PD), which is used to monitor the beam intensity during experiment. The optical photons passing directly through the beam splitter (10 %) are detected by the HARP tube, which contains an *a*-Se photoconductive layer of d_{Se} = 8 μm. Before sensitivity measurements, the HARP input light intensity was calibrated for each λ in order to keep a constant input power. This was achieved by adjustment of the ND filters and monitoring the light intensity using the Si PD.

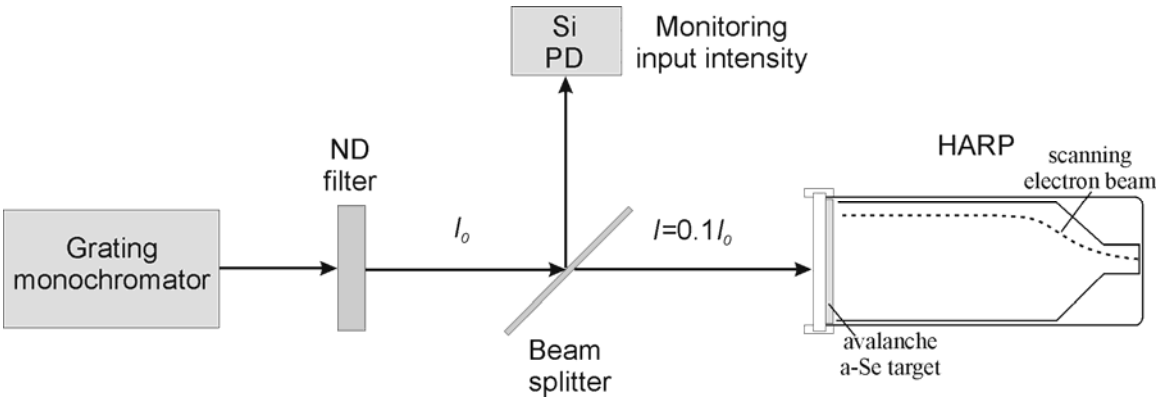

Figure 2.03: Experimental apparatus for measuring the photosensitivity of HARP.

For each λ and E_{Se}, the signal current, *S*, obtained by the HARP tube was recorded, and the photosensitivity, which was quantified as the number of signal charge carriers generated by one absorbed light photon and referred to as the effective quantum efficiency η^*, is the product of η and g_{av}. The values of η^* was experimentally determined from the measurement of HARP tube current *S* using:

$$\eta^* = \frac{S/q}{IT/h\nu}, \qquad (2.10)$$

where q is the electron charge, I is the HARP input light intensity power given in Watts (W), $h\nu$ is the energy of each incident photon, and T is the fraction of the incident photons (to HARP) reaching the *a*-Se layer. The correction factor, T, is due to light attenuation by both the ITO bias electrode and the CeO_2 blocking layer for HARP, and is a function of the wavelength λ. The value of T was experimentally measured for all λ used in our experiment by using a HARP substrate consisting of just the faceplate, electrode, and blocking layer. During the manufacturing of HARP targets this structure is assembled prior to deposition of the *a*-Se layer. The substrate sample was placed in the beam path of the monochromator and the transmission of light was calculated by taking the ratio of the light intensity measured by the Si PD with the sample in place to that without.

2.3.2 Measurement results

Shown in Fig. 2.04 is the measured effective quantum efficiency η^* as a function of E_{Se} for an 8 μm thick HARP layer. It shows that for blue light (λ = 400 nm), η^* reaches a plateau at E_{Se} > 20 V/μm. This corresponds to a saturation of optical quantum efficiency, η, at unity. With a further increase in E_{Se} to > 80 V/μm, η^* starts to increase again, which shows the onset of avalanche. However, for green light, the E_{Se} dependence of η^* is quite different. As shown in Fig. 2.04 for λ = 540 nm, which is the peak of the emission spectrum of CsI (Tl), η^* starts at a much smaller value compared to that with blue light. It then increases continuously with E_{Se} without saturation before avalanche starts at ~80 V/μm. Based on the theory behind the photo-carrier generation mechanism, described in section 2.1, this is because of the lower optical η for green light, which has lower photon

energy, and as a result does not saturate as a function of E_{Se} or reach unity until E_{Se} is well into the range of avalanche multiplication.

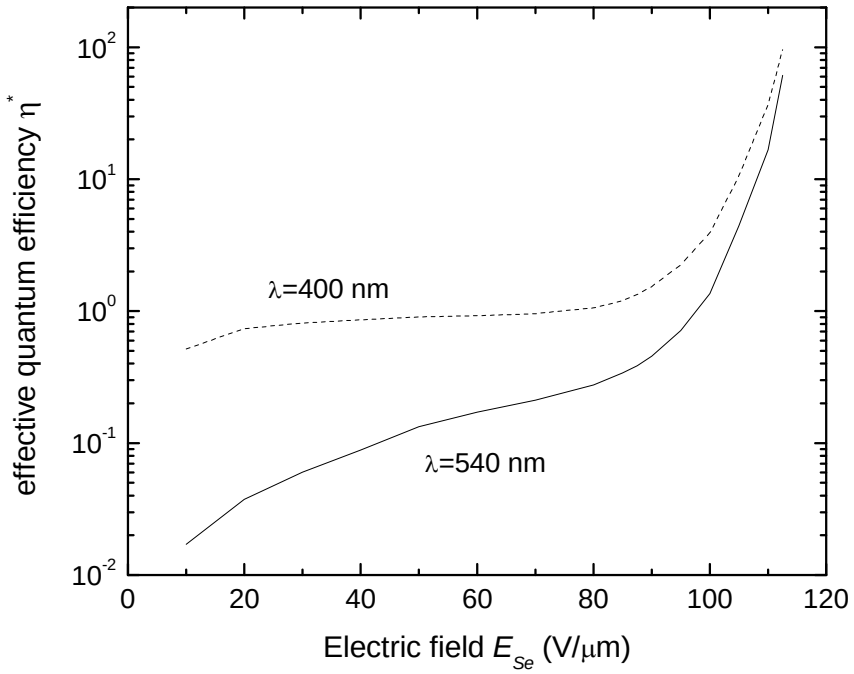

Figure 2.04: Measured effective quantum efficiency η^* as a function of E_{Se} for an 8 μm thick HARP layer.

2.3.3 Determination of the avalanche gain

As we described in Eq. 2.09, the effective quantum efficiency η* of HARP is proportional to both η and g_{av}. The value of η can be calculated by using Eq. 2.01. The initial separation of r_0 is a function of incident photon wavelength λ, which has been measured by Pai and Enck [66]. For the rest of the discussion, we will focus on λ = 540 nm, which is the peak of the emission spectrum for CsI (Tl) used for SAPHIRE.

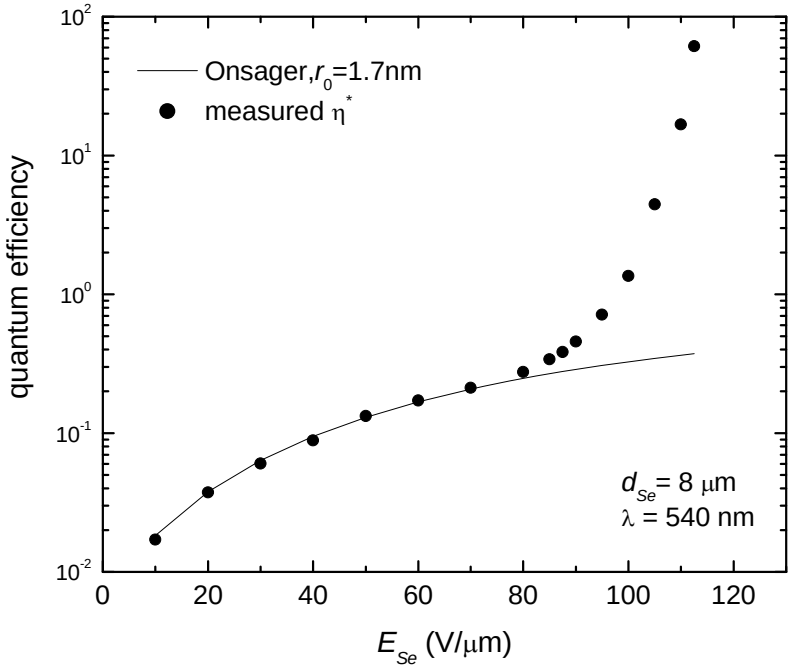

Figure 2.05: Optical efficiency of *a*-Se calculated using Onsager theory and r_0 = 1.7 nm, compared with the measured effective quantum efficiency η* at λ = 540 nm.

Shown in Fig. 2.05 is the value of η calculated using Eq. 2.01 and r_0 = 1.7 nm. The infinite calculation was stopped at l = 140, n =115 and m = 24. Also plotted in Fig. 2.05 are the measurement of η* at the same wavelength for d_{Se} = 8 μm. These results show that the Onsager theory provides a reasonable predication for the E_{Se} dependence of η^* in HARP for $E_{Se} \leq 80$ where g_{av} = 1. The theoretical η-value predicted by Onsager theory was then used as the denominator. The numerator would be the measured η*, which therefore results in the E_{Se} dependence of g_{av}. The results are shown in Fig. 2.06 (a), where g_{av} = 46 at E_{Se} = 110 V/μm. Fig. 2.06 (a) shows that g_{av} increases very rapidly with E_{Se}. As a result choosing the appropriate operating conditions for HARP is crucial. In order to determine the x-ray response of the indirect FPI with avalanche gain, it is necessary to understand the continuous dependence of g_{av} on E_{Se}. This is because as

image charge accumulates on the pixels, the voltage drop across the HARP layer will decrease, i.e., E_{Se} will decrease. With the rapid change of g_{av} as a function of E_{Se} shown in Fig. 2.06 (a), the value of g_{av} will decrease significantly as a result of charge accumulation on the pixels, especially when E_{Se} is high. This will affect the x-ray sensitivity, linearity and dynamic range of the FPI.

Based on avalanche multiplication theory (Eq. 2.08), the avalanche gain g_{av} is a function of E_{Se} (through β, where the effect from electrons, α, has been ignored) and d_{Se}. To determine how β is exponentially dependent on$1/E_{Se}$, we use

$$\beta = \beta_1 e^{\frac{-\beta_2}{E_{Se}}} \tag{2.11}$$

to fit the experimental measurement of g_{av}, where β_1 and β_2 are two constants independent to E_{Se} and d_{Se} By taking the logarithm of Eq. 2.11 twice, we obtain

$$\ln(\ln g_{av}) = \ln(\beta_1 d_{Se}) - \frac{\beta_2}{E_{Se}}, \tag{2.12}$$

which indicates that the quantity $\ln(\ln(g_{av}))$ is linearly related to $1/E_{Se}$. Shown in Fig. 2.06 (b) is the re-plotted experimental data from Fig. 2.06 (a) in the form of $\ln(\ln(g_{av}))$ as a function of $1/E_{Se}$. The best linear fit for the experimental data is also shown in Fig. 2.06 (b). From the intercept and the slope of the fitted straight line we obtained

$$\beta_1 = 5.5 \times 10^3 \text{ /μm} \tag{2.13}$$

and

$$\beta_2 = 1.029 \times 10^3 \text{ V/μm}. \tag{2.14}$$

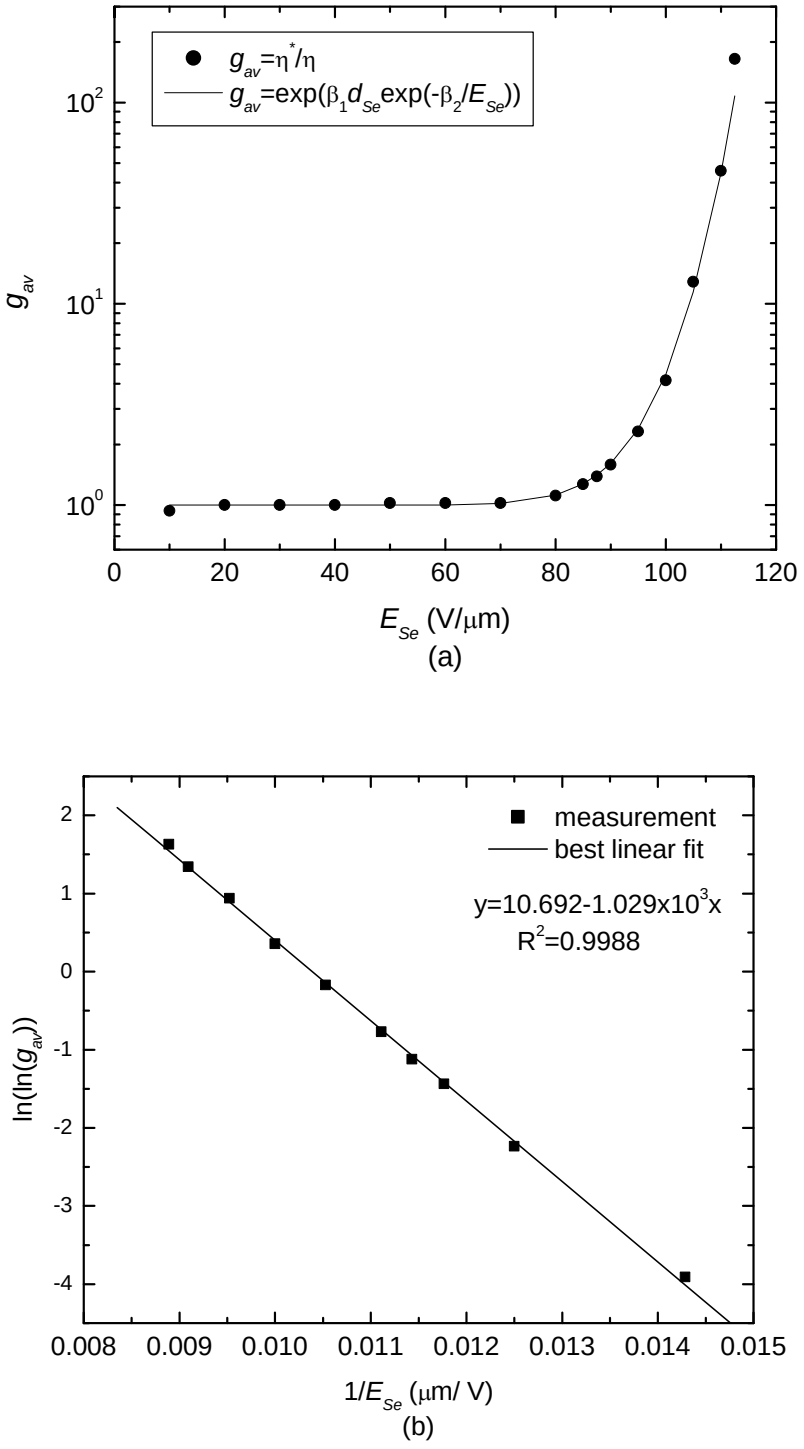

Figure 2.06: (a) Solid circles are the g_{av} for the 8 μm HARP layer calculated by dividing the measured η^* at 540 nm by the optical η predicted by the Onsager theory using r_0 = 1.7 nm. The solid line shows the g_{av} calculated using the fitted β_1 and β_2 values. (b) The plot of ln(ln(g_{av})) as a function of $1/E_{Se}$, and the best linear fit for the data.

The fitting parameters agree well with the experimentally determined g_{av}. Using these β_1 and β_2 values and the analytical expression for g_{av} shown in Eq. 2.08, the theoretical g_{av} values are calculated and shown in Fig. 2.06 (a). Since g_{av} is related to β_2 through two exponential functions, a small error in the estimate of β_2 may result in a large error in the estimation of g_{av}. Nevertheless, the Fig. 2.06 shows the excellent quality of fitting for E_{Se} in the range $\leq$ 110 V/μm in the figures. The fitting parameters β_1 and β_2 are slightly different from that obtained from samples without LiF doped layer. This may be due to the field modulation caused by a positive space charge in the LiF doped region [70, 71].

2.4 X-ray imaging performance

2.4.1 Cascaded linear system model

Digital medical imaging systems are complex with multiple physical processes involved in the conversion of the input signal to the final output image, which is presented to the physicians. A highly-quality image is obtained only when all processes are designed appropriately to ensure accurate transfer of the image signal and noise from input to output. This transfer is laid out by communication theory, and in particular, by the Fourier transform linear-systems approach [72]. Linear-system theory was initially applied in the imaging sciences by Rossmann [73-75] and then developed by others [76-81]. Normally, the final image is represented as a cascade of multiple processes in the systems, and is then described by the linear system theory for the transfer of signals and noise.

There are three elementary processes which play an important role in the transfer theory: (a), quantum amplification; (b) deterministic blurring; and (c) quantum scattering,

which is also called stochastic blurring in other publications. The image formation process can be interpreted as an appropriate serial combination of these three processes. The characteristic details [82] will not be described here.

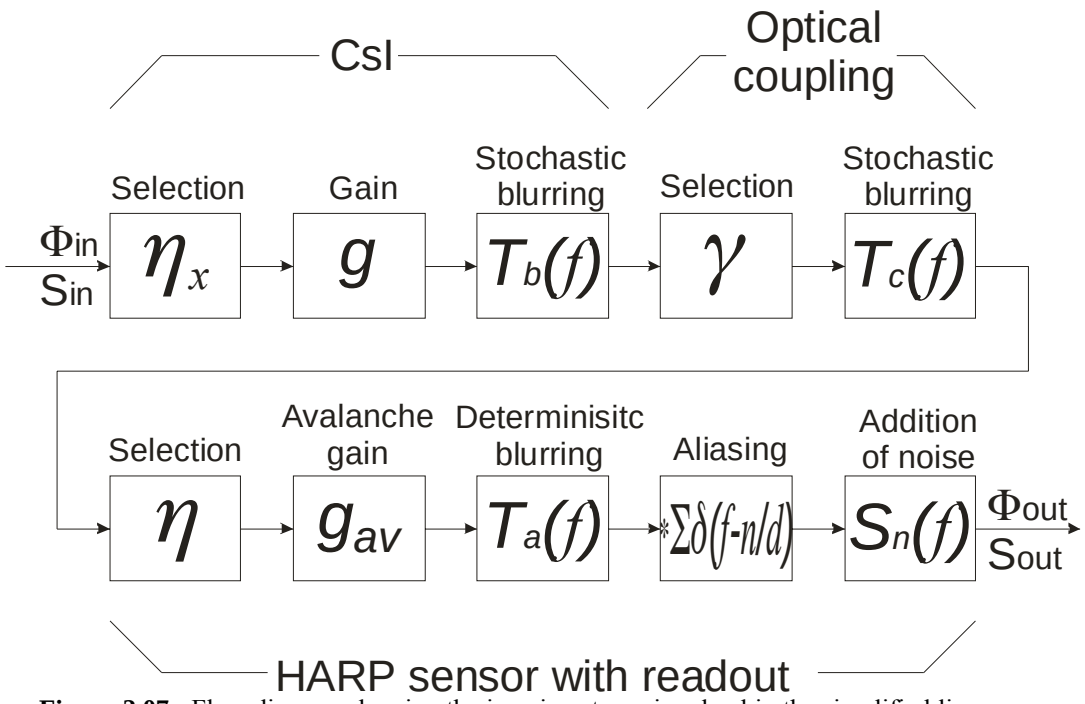

Figure 2.07: Flow diagram showing the imaging stages involved in the simplified linear system model for SAPHIRE, adapted from [1]. Φ and S represent the signal and noise, respectively.

In order to obtain an estimate of how much avalanche gain is needed for SAPHIRE, we adopted a preliminary cascaded linear system model developed in our group [1]. Shown in Fig. 2.07 is a flow diagram of the imaging stages. To simplify the model for SAPHIRE, it does not yet show the effect of K-fluorescence reasbsorption or the Lubberts' effect [83] in CsI. The effect of direct x-ray interaction events in the HARP layer is also ignored.

Using the cascaded linear system model, we investigated two important aspects of the x-ray imaging performance, the pixel x-ray response of the detector, i.e. the linearity and

dynamic range, for both the avalanche and non-avalanche operational modes, and the DQE.

From the cascaded linear system model, we obtain the mean signal, Φ_s, from each pixel of the detector, which is given by

$$\Phi_s = \frac{a_p{}^2 \gamma \eta g_{av} E_{ab}}{W}, \tag{2.15}$$

where W is the energy required to generate an optical photon in CsI, and E_{ab} is the x-ray energy absorbed by CsI per unit area. E_{ab} here includes contributions from all three parallel paths associated with K-fluorescence, i.e.

$$E_{ab} = \sum_E q_0(E)\eta_x(E)[(1-P_k)E + (E-E_k)P_k + E_k P_k f_k], \tag{2.16}$$

where $q_0(E)$ is the incident x-ray photons per unit area as a function of energy E for a given x-ray spectrum, P_k is the probability of K-fluorescence, E_k is the energy of the K-fluorescence photon, and f_k is the fraction of K-fluorescence reabsorbed in the CsI layer. Each of the K-fluorescence related terms in Eq. 2.16 were determined separately for the K_α and K_β photons from both Cs and I atoms and integrated to obtain the final result of E_{ab}.

Thus the final DQE from the cascaded linear system model in Fig. 2.07 is then given by:

$$\mathrm{DQE}(f) = \frac{T_b{}^2(f)T_c{}^2(f)T_a{}^2(f)}{[\frac{1}{\eta_x A_S}T_b{}^2(f)T_c{}^2(f) + \frac{(2g_{av}-1)}{g_{av}g\eta_x\gamma\eta}]T_a{}^2(f) + \frac{S_n}{(a_p{}^2 g_{av} g\eta_x\gamma\eta)^2 q_0}}, \tag{2.17}$$

where q_0 is the number of incident x-ray photons per unit area, γ is the optical coupling efficiency between CsI and HARP layer, $T_b(f)$, $T_c(f)$, and $T_a(f)$ are the MTF due to blur in

CsI, the optical coupling between CsI and HARP, and the pixel aperture function, respectively. A_S, η_x, and g are the Swank factor, x-ray quantum absorption efficiency and x-ray to photon conversion gain of the CsI layer, respectively. a_p is the pixel width. S_n is the electronic noise associated with the pixel readout. For simplicity, we ignore the effect of aliasing. This is a reasonable assumption for most indirect detectors. The denominator of Eq. 2.17 is the dose normalized NPS. The first term is the x-ray quantum noise, the second term is the secondary quantum noise associated with the variance in gain in the conversion and the avalanche process, and the third term is the contribution from the electronic noise of the readout. It shows that the electronic noise is less important at high dose (i.e., q_0 is high). It is also inversely proportional to g_{av}^2. This demonstrates that the introduction of avalanche gain effectively reduces the importance of noise at low dose. The avalanche gain also introduces additional noise due to its variance, as the second term, which is approximately twice for $g_{av} >> 1$ than that for $g_{av} = 1$, assuming η is the same in both cases. This excess secondary quantum noise is the penalty for avalanche gain. However for SAPHIRE with high conversion gain g and efficient optical coupling between CsI and HARP, i.e. $g\eta_x\gamma\eta \gg 2$, the secondary quantum noise is negligible compared to the x-ray quantum noise. Here, $T_a(f)$ is the aperture function of readout, which remains unknown for FEA right now. However, it is reasonable to assume it behaves like a TFT readout, i.e., it is a sinc function from the Fourier transform of a square aperture function with fill factor of unity. When the electronic noise is small, the factor $T_a(f)$ will be eventually cancelled from this equation. Eq. 2.17 also does not include the effect of K-fluorescence reabsorption of CsI which have been investigated by Zhao, *et. al.* [3]. The results showed that K-fluorescence reabsorption in CsI has too effects: (1)

degradation of the Swank factor for x-ray energies above the K-edge and (2) additional image blur.

The previous investigation of the inherent x-ray imaging performance of CsI (Tl) has shown that the high resolution (HR) type has essentially no depth dependent blur and provides better DQE(*f*) at high spatial frequencies compared to the CsI optimized for high light output (HL) [3]. This was achieved at the cost of a lower light output (60 %) for the HR compared to the HL type. For the calculation in this chapter, we used a 150 μm HR type CsI for mammography and a 600 μm HL CsI for R/F applications. The previously measured values for W, A_S and presampling MTF of these CsI layers were used in the cascaded linear system model. Since we have not yet implemented the depth dependent blur of CsI in our cascaded linear system model, the DQE(*f*) at high frequencies for the 600 μm HL CsI layer (for R/F) will be overestimated. Table 2.01 summarizes the detector parameters and HARP operating conditions chosen for each application. For mammography, we consider two different image acquisition modes: regular screening mammography and tomosynthesis.

Table 2.01: Detector design operating conditions chosen for different x-ray imaging applications.

	Mammography detector		R/F detector	
	tomosynthesis	screening	Fluoroscopy	radiography
X-ray spectrum	28 kVp Mo/Mo, 4cm PMMA		RQA5	
CsI (75% packing)	150 μm HR		600 μm HL	
W for CsI (eV)	30		18	
α	0.8		0.8	
Minimum exposure	0.1 mR	1 mR	0.1 μR	30 μR
E_{Se} (V/μm)	110	105	110	95
η	0.36	0.35	0.36	0.31
g_{av}	46	12	46	2.3

2.4.2 Pixel response

In this section, we will apply the E_{Se} dependence of g_{av} and η derived in previous sections to determine the x-ray response of the SHARP layer. Due to the difference in resolution and avalanche gain requirement for mammography and R/F detector, the calculation will be performed separately for these two imaging applications.

A. Radiography/Fluoroscopy

Shown in Fig. 2.08 is the DQE(*f*) calculated using the cascaded linear system model for the detector with different g_{av} settings. The calculation was performed for the lowest exposure in fluoroscopy (0.1 μR), where the detector performance is most susceptible to electronic noise. It shows that g_{av} = 46 is sufficient to bring the DQE(*f*) to its theoretical limit (i.e. a detector without electronic noise). The DQE(*f*) for the next g_{av} = 12 measured at E_{Se} = 105 V/μm also provides reasonable DQE. Thus, an E_{Se} between 105 and 110 V/μm will be adequate for fluoroscopy. Fig. 2.09 shows the DQE(*f*) calculated for the lowest radiographic exposure of 30 μR. It shows that E_{Se} = 95 V/μm can provide sufficient η (0.31) and g_{av} (2.3). Hence the E_{Se} chosen in Table 2.01 is adequate for the dual-mode operation of a R/F detector.

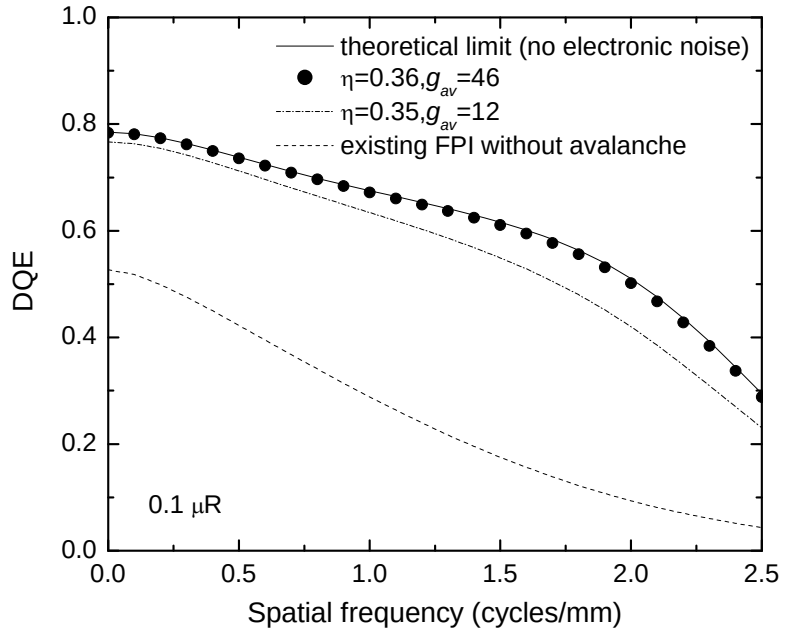

Figure 2.08: Calculated DQE(f) for a fluoroscopy detector at the x-ray exposure level of 0.1 μR. Operating conditions are shown in Table 2.01.

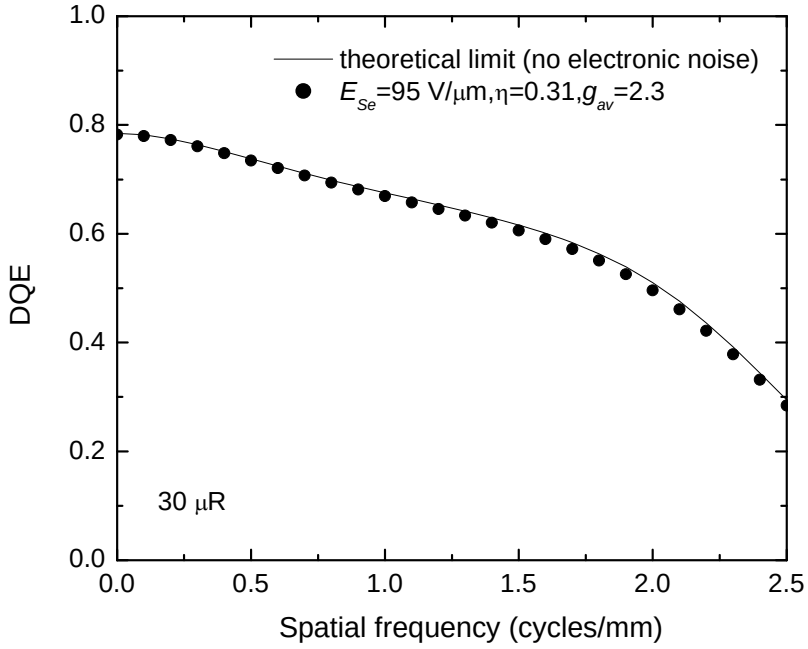

Figure 2.09: Calculated DQE(f) for a fluoroscopy detector at the x-ray exposure level of 30 μR. Operating conditions are shown in Table 2.01.

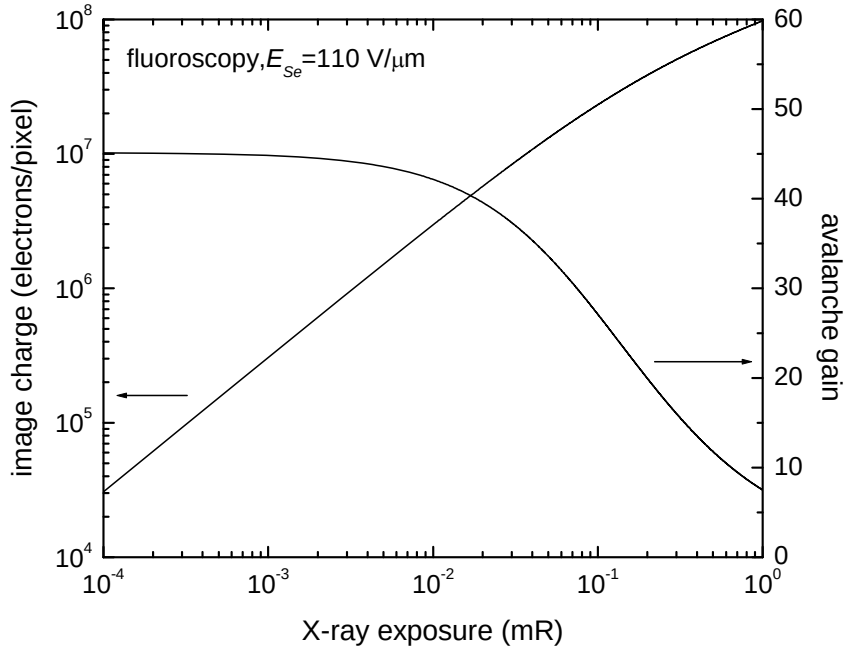

Figure 2.10: Calculated image charge on each pixel of the detector and the corresponding avalanche gain as function of x-ray exposure for the fluoroscopy detector.

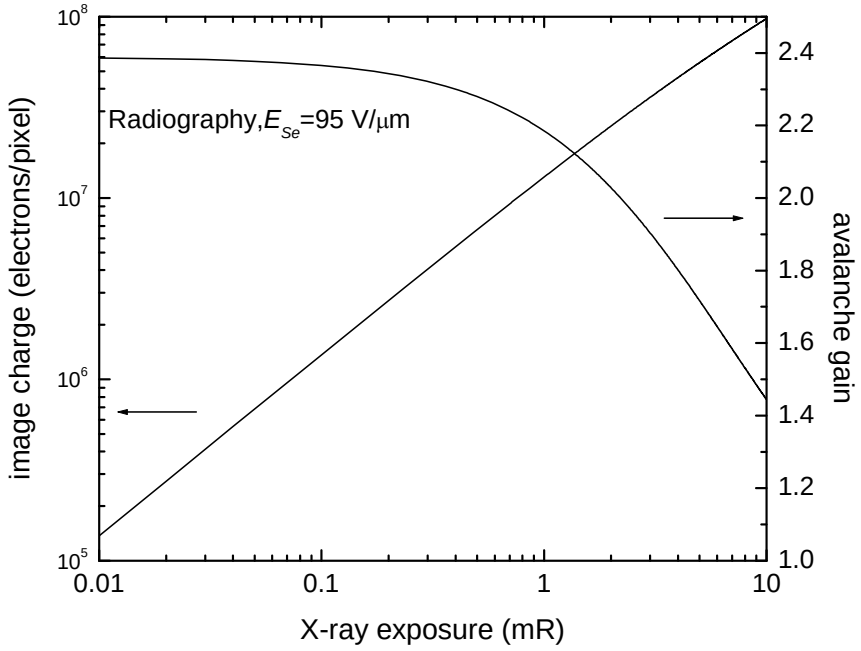

Figure 2.11: Calculated image charge on each pixel of the detector and the corresponding avalanche gain as function of x-ray exposure for the radiography detector.

Shown in Figs. 2.10 and 2.11 are the calculated pixel x-ray responses for the R/F detector under two different operating conditions. Here we assumed that the dominant pixel capacitance is the capacitance of the HARP layer. This condition results in the largest drop in the potential across the HARP layer for a given x-ray exposure, and creates the biggest effect on linearity. Fig. 2.10 shows that for fluoroscopy, the initial E_{Se} = 110 V/μm provides a g_{av} of 46. Within the regular exposure range of 0.1 – 10 μR per frame in fluoroscopy, the detector has very good linearity, i.e. an essentially constant g_{av}. With further increase in exposure, which corresponds to the exposure near or beyond the edge of the human body, the x-ray response becomes sub-linear with a decrease in g_{av}. This decrease in g_{av} ensures a wide dynamic range for the detector because there is no "hard" saturation. The pixel potential will continue to increase as a function of x-ray exposure. The pixel potential for the exposure of 1 mR in the fluoroscopy mode is V_P = 56 V. Fig. 2.11 shows that with a much lower g_{av} = 2.3 programmed for radiography, the detector response for the regular exposure range of 30 μR – 3 mR is essentially linear with very little change in g_{av}. Comparing Figs. 2.10 and 2.11, the image charge on the pixels are in the same range despite their large difference in exposure range. This demonstrates the wide dynamic range (over 5 orders of magnitude) of the detector by varying g_{av} for different x-ray imaging applications. This is different from a detector with constant high gain, which has problems of pixel saturation for radiographic applications.

B. Mammography

Figs. 2.12 and 2.13 show the DQE calculated for mammography detector. The parameters and the operating conditions are listed in Table 2.01 for tomosynthesis and screening applications. Both figures show that the choice of E_{Se} for both operational modes are adequate for achieving the theoretical limit of DQE without electronic noise.

The pixel x-ray response for mammography was calculated and the results are shown in Figs. 2.14 and 2.15 for tomosynthesis and screening mammography, respectively. The minimum exposure in both figures corresponds to the detector exposure behind dense breast tissue, and the maximum corresponds to raw exposure. Figs. 2.14 and 2.15 show that when there is no storage capacitance, the signal increases sub-linearly as a function of the x-ray exposure. This is because the pixel capacitance due to the HARP layer for mammography is only ~0.02 pF with a_p = 50 μm, which is much smaller than that for the R/F detector (0.28 pF). Hence the signal accumulated on each pixel creates a much more significant drop in the E_{Se}, which causes a rapid decrease in g_{av}. The maximum image charge shown in Figs. 2.14 and 2.15 corresponds to a pixel potential of ~100 and 210 V, respectively. Alternatively we have proposed a detector called SHARP-AMFPI, which reads out the signal by TFT arrays rather than FEA [52]. However, these potentials exceed the maximum voltage safe for the TFT readout. One method for alleviating this problem while maintaining the same dynamic range is to add a pixel storage capacitance C_{st}. With C_{st} = 0.5 pF, the pixel potential rises much slowly and the x-ray response of the detector becomes more linear. The pixel potentials corresponding to the maximum exposures in Figs. 2.14 and 2.15 reduce to 25 and 50 V, respectively, both of which are safe for TFTs.

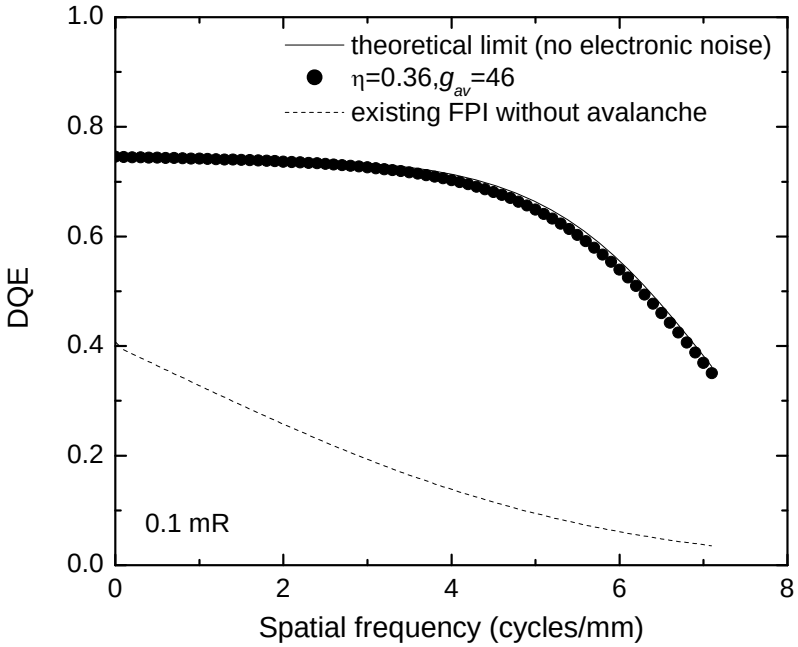

Figure 2.12: Calculated DQE(*f*) using the detector parameters and operating conditions shown in Table 2.01 for mammographic tomosynthesis with minimum exposure of 0.1 mR.

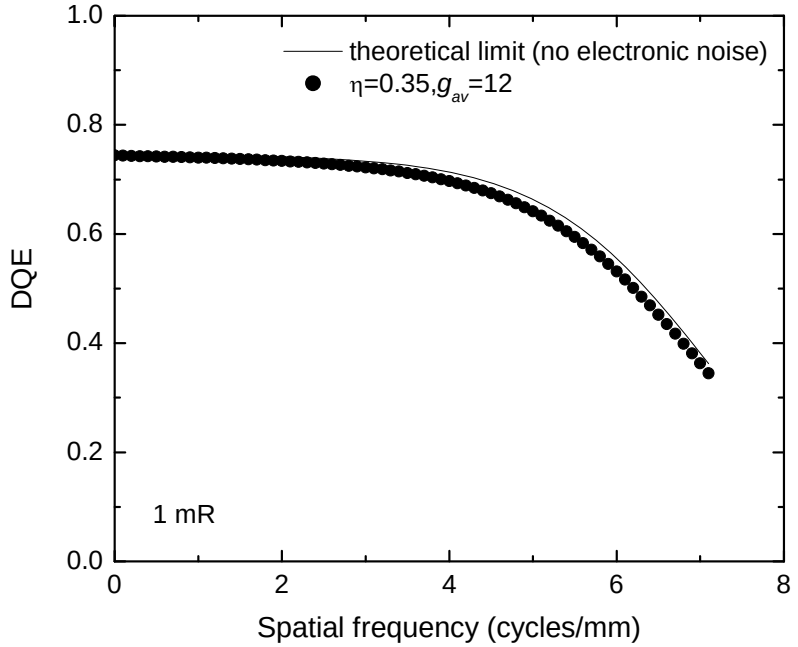

Figure 2.13: Calculated DQE(*f*) using the detector parameters and operating conditions shown in Table 2.01 for screening mammography with minimum exposure of 1 mR.

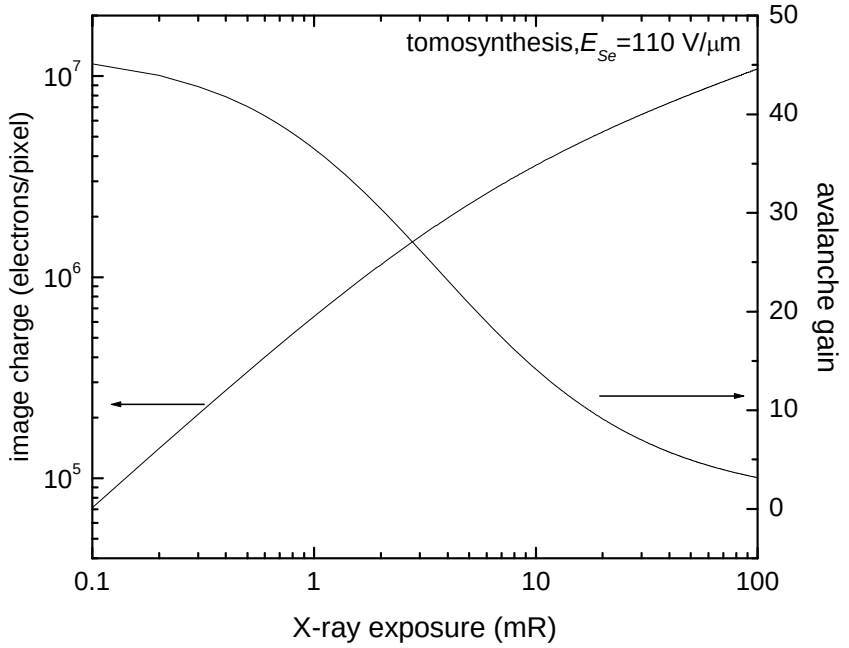

Figure 2.14: Calculated image charge on each pixel of the mammography detector and the corresponding avalanche gain as a function of x-ray exposure. The results are for detector operating conditions chosen for tomosynthesis image acquisition.

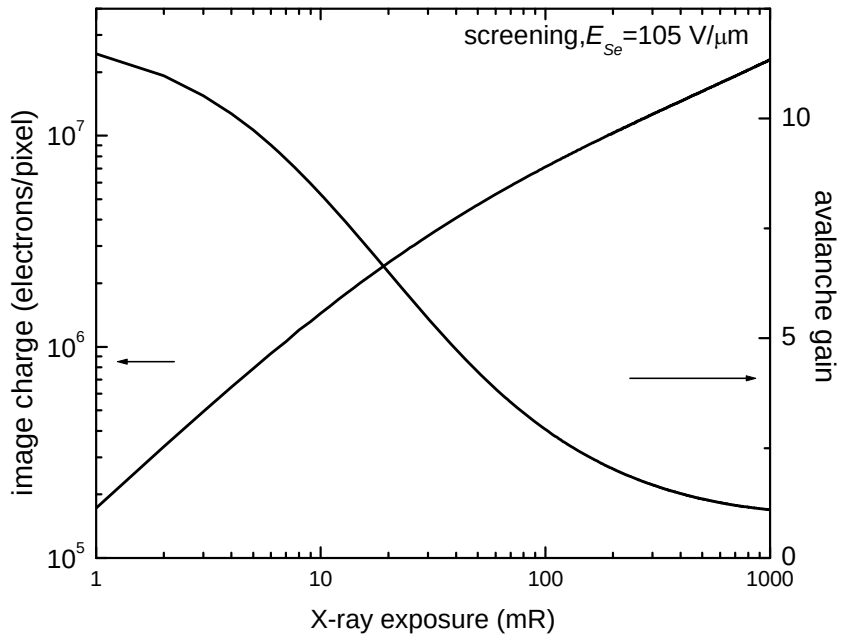

Figure 2.15: Calculated image charge on each pixel of the mammography detector and the corresponding avalanche gain as a function of x-ray exposure. The results are for detector operating conditions chosen for screening mammography.

2.4.3 Direct x-ray interaction in HARP

In indirect FPI, direct interaction of x-rays in the photodiodes (or CCD) produces additional noise [84]. This is because the x-ray to charge conversion gain in the photodiodes is much higher (~ 50 times) than that in phosphors, which causes each direct interaction x-ray to produce a much higher signal (and noise) than that absorbed in the phosphors. For our proposed detectors, the HARP sensor (e.g. d_{Se} = 8 μm) is much thicker than the a-Si photodiodes (~ 1 μm) in existing indirect FPI, hence there will be more direct x-ray interaction events. Fortunately the x-ray to charge conversion gain in HARP [43] (W_{Se} = 16 eV at E_{Se} = 100 V) is very similar to that in CsI, thus direct x-ray interaction in HARP is not expected to add additional noise. However when HARP is operated in the avalanche mode, the x-rays absorbed by HARP will experience different avalanche gain depending on their depth of interaction. For x-rays absorbed in HARP at depth x from the top (light entrance) interface, the effective thickness for avalanche multiplication is ($d_{Se} - x$). This could lead to a depth dependent variation in g_{av}, and add additional noise [85]. In the following we will derive the propagation of signal and noise due to direct x-ray interaction in HARP, and investigate the effect on the DQE of SHARP-AMFPI.

A. Signal and noise propagation for direct x-ray interaction

The input for direct x-ray interaction in HARP is the number of x-rays transmitted through the CsI layer, q_1, which is a function of x-ray energy. For clarity we assume a mono-energetic x-ray beam in the following derivation of theory, although we used the

full x-ray spectrum in our calculation of direct x-ray interaction. We ignored the effect of K-fluorescence reabsorption in HARP. Under this assumption, both the signal and NPS for direct x-ray interaction are white prior to the pixel aperture function so that we could omit the frequency dependence in the following derivation. The x-ray signal produced at depth x into the HARP layer by a small thickness dx of a-Se is given by:

$$\Phi(x) = q_1 e^{-\mu x} g_{av}(x) g_{Se} \mu \, dx \,, \tag{2.18}$$

where μ is the linear attenuation coefficient of a-Se, and g_{Se} is the average x-ray to charge conversion gain which is equal to E/W_{Se}. The depth dependence in g_{av} can be derived from Eq. 2.05 as $g_{av}(x) = \exp[\beta(d_{Se} - x)]$. The noise power spectrum NPS due to direct interaction as a function of depth, $S(x)$, is given by [85]:

$$S(x) = \exp(-\mu x)[(g_{Se}{}^2 + \sigma^2{}_{g_{Se}})g_{av}{}^2(x) + g_{Se}\sigma^2{}_{g_{av}}(x)]\mu dx \,. \tag{2.19}$$

Integrating both Eqs.2.18 and 2.19 with respect to x from 0 to d_{Se}, we obtain the total signal and NPS due to direct x-ray interaction:

$$\Phi = \frac{\mu g_{Se}(e^{\beta d_{Se}} - e^{-\mu d_{Se}})}{\mu + \beta} \tag{2.20}$$

and

$$S = \frac{\mu(g_{Se}{}^2 + \sigma^2{}_{g_{Se}})(e^{2\beta d_{Se}} - e^{-\mu d_{Se}})}{\mu + 2\beta} \tag{2.21}$$

B. Calculation results

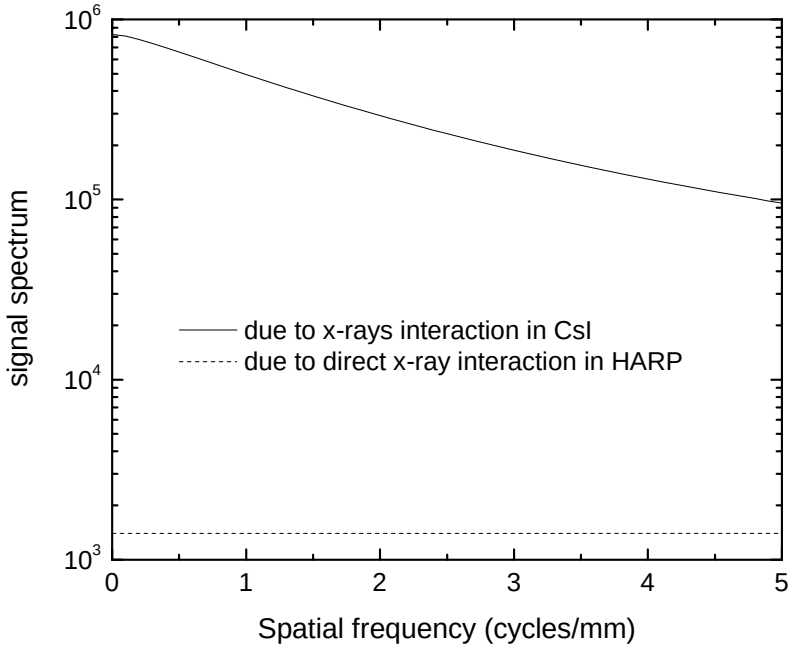

Figure 2.16: Signal spectra comparison of the pre-sampling signal and NPS (before pixel aperture function) due to x-ray absorbed in CsI and direct x-ray interaction in HARP, where the signal due to direct interaction is negligible.

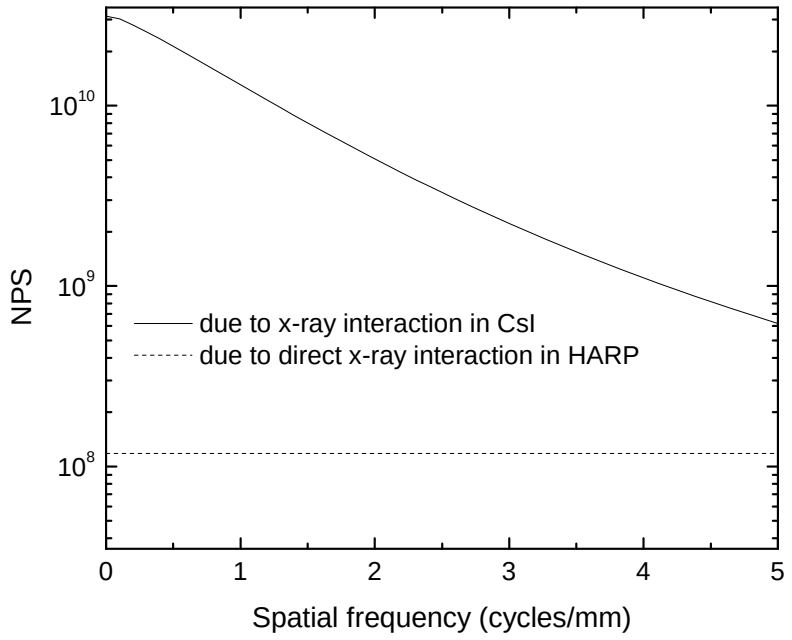

Figure 2.17: NPS comparison of the presampling signal and NPS (before pixel aperture function) due to x-ray absorbed in CsI and direct x-ray interaction in HARP, where the NPS due to direct interaction under the Nyquist frequency of 2.5 cycles/mm is negligible.

Using Eqs.2.20 and 2.21, we calculated the contribution to the total signal and NPS by the direct interaction of x-rays in HARP using the parameters shown in Table 2.01 for an R/F detector. With a RQA5 x-ray spectrum and a 600 μm HL layer of CsI, the fraction of x-rays transmitted through the CsI layer is 13.2%, out of which ~1 % is absorbed by the HARP layer. Shown in Fig. 2.16 is a comparison between the presampling signal spectra (before the pixel aperture function) due to x-rays absorbed in CsI and that in HARP. It shows that at low frequencies, the signal due to direct x-ray interaction is less than 0.2 % of that due to x-ray absorbed in CsI. This is consistent with the difference in their x-ray quantum efficiencies. At high frequencies (e.g. 5 cycles/mm), the signal from CsI decreases due to the blur in CsI, however the signal from direct x-ray interaction in HARP stays constant. But the latter is still negligible. Shown in Fig. 2.17 is the NPS (before pixel aperture function) comparison. It shows that at 5 cycles/mm, the NPS due to direct x-ray interaction becomes significant (~17 % of the NPS due to CsI). However below the Nyquist frequency of 2.5 cycles/mm, it is still negligible (< 3 %). This is why there is no significant change in DQE after including the direct x-ray interaction events in HARP, as shown in Fig. 2.18. Hence we can conclude that direct x-ray interaction in HARP in an indirect FPI with avalanche gain has no degradation effect on DQE of the detector.

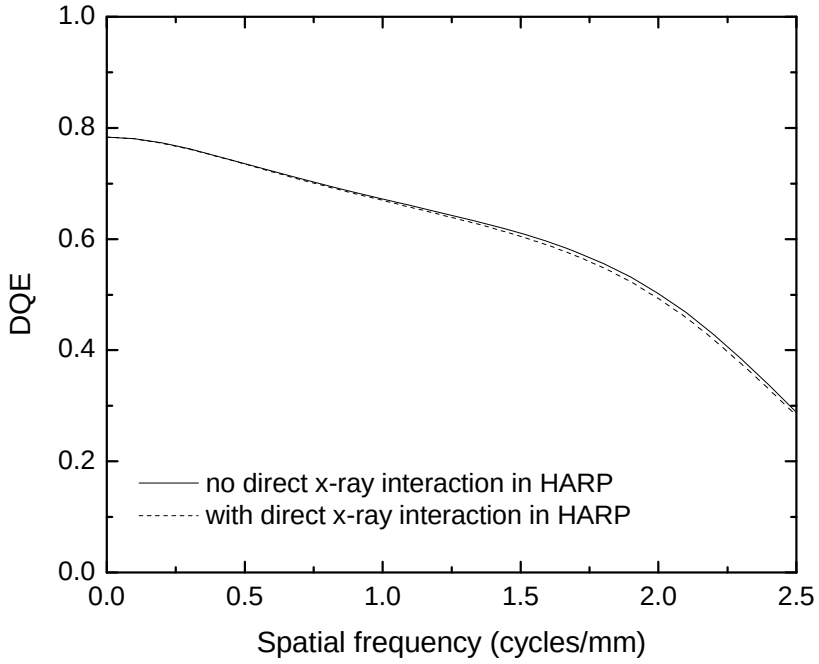

Figure 2.18: Comparison between the DQE of SHARP-AMFPI with and without consideration of direct x-ray interaction in HARP.

2.5 Effect of HARP thickness uniformity

An important issue for making a large area HARP is its thickness uniformity. Currently HARP films can be made very uniform for an area of 1-2" in diameter with essentially no visible gain variation in the images. The images currently produced by HARP for broadcast applications do not require any gain uniformity correction. The area of HARP needs to be increased significantly for x-ray imaging applications. Although uniform, large area *a*-Se films have been developed for direct FPI, the uniformity requirement for HARP in indirect FPI with avalanche gain is expected to be much higher. In this section we will derive the relationship between thickness non-uniformity and gain non-uniformity for HARP sensors so that the results can be used as a guideline for engineering of large area HARP layers for FPI.

2.5.1 Relationship between HARP avalanche gain and thickness uniformity

During the operation of HARP, a constant potential V_b is applied to the top ITO bias electrode, as shown in Fig. 2.02. A non-uniformity in the thickness of HARP will result in a variation in E_{Se} and subsequently a gain non-uniformity. An increase in d_{Se} under a constant V_b causes a decrease in E_{Se}. Although an increase in d_{Se} tends to increase g_{av} (Eq. 2.08)**,** the simultaneous decrease in E_{Se} will lead to a much bigger effect in decreasing g_{av} because of the additional exponential dependence shown in Eq. 2.11. By substituting $E_{Se} = V_b/d_{Se}$ into Eq. 2.12 and differentiating both sides, we obtain:

$$\frac{1}{\ln g_{av}} \frac{\triangle g_{av}}{g_{av}} = \frac{\triangle d_{Se}}{d_{Se}} - \frac{\beta_2}{V_b} \triangle d_{Se} . \tag{2.22}$$

Eq. 2.22 can be rewritten as:

$$\frac{\Delta g_{av}}{g_{av}} = \ln(g_{av})(1 - \frac{\beta_2}{E_{Se}}) \frac{\Delta d_{Se}}{d_{Se}} \tag{2.23}$$

Eq. 2.23 shows that with $\beta_2 > E_{Se}$, which is true for HARP, a positive change in d_{Se} results in a negative change in g_{av}. Eq. 2.23 also shows that the percentage variation in avalanche gain is proportional to $\ln(g_{av})$ and the percentage thickness variation, hence HARP layers operated with higher g_{av} is more susceptible to thickness non-uniformity.

2.5.2 Calculation of gain non-uniformity

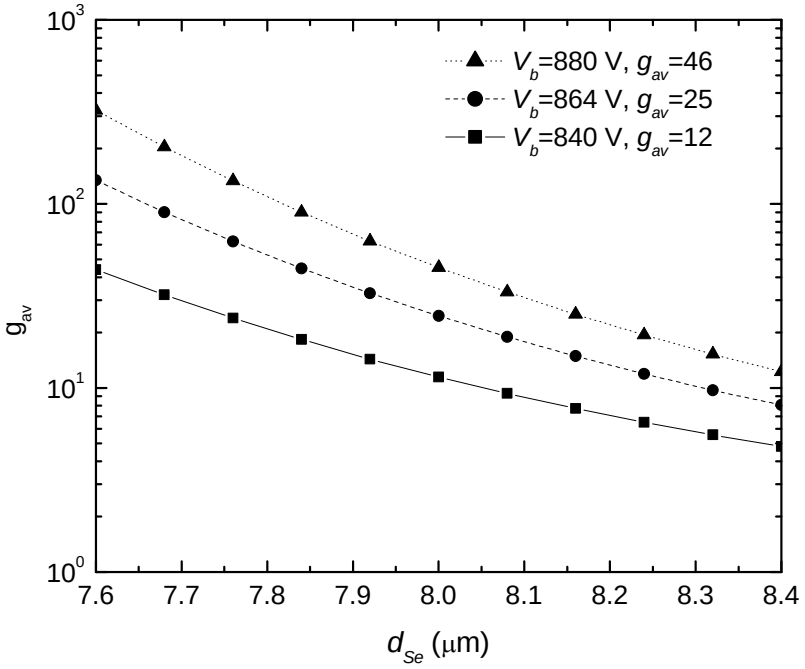

Figure 2.19: The avalanche gain g_{av} calculated as a function of the thickness of HARP, which varies around 8 μm, under a constant bias potential V_b of 840, 864 and 880 V.

Using Eqs.2.08 and 2.11, and the values for β_1 and β_2 determined in Section 2.3.3, the variations in g_{av} were calculated for both positive and negative change in d_{Se} around 8 μm, and results are shown in Fig. 2.19. Three V_b values of 840 V, 864 V and 880 V were used, which corresponds to g_{av} of 12, 25 and 46, respectively. Fig. 2.19 shows that the slope of the curve, i.e. percentage change in g_{av}, is much higher for negative change in d_{Se}, which causes an increase in g_{av}, than it is for positive. Hence when choosing the bias potential V_b of HARP for a desired E_{Se}, the smallest d_{Se} for the entire detector area should be used, so that the variation in thickness is positive from the reference thickness. If we assume the smallest d_{Se} = 8 μm, the percentage changes in g_{av} due to an increase in d_{Se} of 1 % are 19 %, 23 % and 26 %, respectively, for the three V_b settings of 840 V, 864 V and 880 V. The change in g_{av} increases to 33 %, 40 %, and 44 %, respectively, when the

variation in d_{Se} increases to 2 %. This range of g_{av} non-uniformity is certainly within the capability of gain correction and the dynamic range of the electronic circuits of FPI. With further increase in d_{Se} to 4 %, the value for g_{av} will decrease from the original setting of 46, 25 and 12 to 15, 10 and 6, respectively, which is a gain non-uniformity of 2 to 3 folds. Although the change in g_{av} is significant, it is not expected to cause significant degradation in the DQE performance, as can be seen in the example of g_{av} = 46 and 12 shown in Fig. 2.08. However this will pose more challenges for the uniformity correction algorithm. Hence we can conclude that a maximum thickness non-uniformity of 2 % is desirable for a HARP layer, and 4 % non-uniformity could still possibly be tolerated.

2.6 Conclusions

The feasibility of a new concept of indirect conversion flat-panel detector with avalanche gain is being investigated. The avalanche gain and quantum efficiency of an 8 μm thick HARP layer was investigated experimentally as function of E_{Se}. The characteristics of HARP were applied to a cascaded linear system to determine the operating conditions for x-ray imaging. Our results showed that by varying the avalanche gain between 2 and 46, x-ray quantum noise limited performance and a wide dynamic range can be obtained for typical detector parameters chosen for both R/F and mammographic imaging applications. Direct x-ray interaction in HARP is not expected to affect the imaging performance. Due to the rapid increase in g_{av} as a function of E_{Se}, a small variation in d_{Se} can cause significant non-uniformity in avalanche gain. It is desirable to keep the thickness uniformity of a HARP layer within 2 %, which could keep the variation in g_{av} within ~ 40 %.

Chapter 3

Spatial Resolution

In the previous chapter, the programmable avalanche gain of HARP has been investigated, which can improve the low dose performance of SAPHIRE. Because of the avalanche gain, a high resolution (HR) type of CsI (Tl), which has not been widely used in indirect FPI due to its lower light output, can be used to improve the high spatial frequency performance. The FEA can be also made with pixel sizes down to 50 μm. The purpose of this chapter is to investigate the factors affecting the spatial resolution of SAPHIRE. Since the resolution performance of the Scintillator/HARP combination has been well studied, the focus of this chapter is on the inherent resolution of the FEA readout method. The lateral spread of the electron beam emitted from a 50 μm × 50 μm pixel FEA was investigated with three different electron-optical designs: mesh-electrode-only, magnetic focusing and electrostatic focusing. Our results showed that both magnetic and electrostatic focusing methods can satisfy the requirement of 50-μm-pixel size. However the electrostatic focusing is more feasible with the manufacture of large area FPI and provides better spatial uniformity.

3.1 Introduction

The pixel sizes currently used in mammography AMFPI range from 70 to 100 μm, which may not be optimal for the detection of calcifications. For example, it has been shown that with pixel size d_{el} = 100 μm characterization of the shape of micro-calcifications is compromised in digital mammography, while d_{el} = 50 μm can preserve this information [8].

As we described the structure and operational principles of SAPHIRE in Chapter 1, the concept of electron beam readout by FEA is similar to that used in optical and x-ray vidicons [48], except that the FEA is a compact, two-dimensional source of electron beams, allowing the construction of the detector in the form of a FPI. As an emerging technology for large area flat-panel FED, FEA has the potential to provide a smaller pixel size than that achieved with TFT readout. As shown in Fig. 1.08, the overlapping area between the base and gate electrodes defines the pixel size. Therefore smaller pixel FEAs require thinner passive addressing lines and essentially no increase in cost. Sufficient FE tips can be included in a small pixel of d_{el} = 50 μm to provide sufficient emission current to produce the wide dynamic range required in medical images. A mesh electrode, biased with a positive potential, is inserted halfway between the FEA and HARP target to minimize the lateral spread of electron beams before they land on the free surface of the HARP target. As will be discussed later in this chapter, more sophisticated electron beam focusing methods are desirable to reach a pixel size of 50 μm.

Compared to existing AMFPI, SAPHIRE can use a high resolution (HR) type of CsI because of the additional gain provided by HARP. HR type CsI has less Lubberts effect,

i.e. depth dependent blur, which is the main source of DQE degradation at high spatial frequencies [3, 53]. Despite its resolution advantages, HR CsI has not been used widely in commercial indirect FPI due to its low conversion gain, which makes the detector more susceptible to electronic noise at low exposure levels [54, 55].

In this chapter, we focus our investigation on the factors affecting the spatial resolution of SAPHIRE. Since breast imaging is the application that requires the highest spatial resolution, we will use a hypothetical mammography detector design as an example for our discussion, although SAPHIRE can be used in a general purpose R/F detector as well. In Section 3.2, we provide a brief review of the principles and mechanisms of field emission as well as the electron beam readout method, especially the parallel electron beam readout proposed for SAPHIRE. In Section 3.3, we present our theoretical and simulation methods for investigating the spatial resolution of SAPHIRE, focusing on the factors related to the FEA readout. Three different electron-optical designs for focusing the electron beams are included in our investigation: (1) a basic design incorporating only a mesh electrode, such as that shown in Fig.1.09, (2) magnetic focusing, and (3) electrostatic focusing in addition to the mesh electrode. In Section 3.4, the results for different electron-optical designs are presented and compared from which we draw conclusions about the desired methods for electron beam focusing in SAPHIRE.

3.2 Background and theory

3.2.1 Principles of field emission

Field emission refers to the extraction of electrons from the surface of a condensed phase (e.g. conductor or semiconductor) into another phase (e.g. the vacuum) under very

high electric fields (0.3-1.0 V/Å) [86]. As an example, Fig. 3.01 shows the energy band diagram of a conductor. The work function φ is defined as the energy difference between the Fermi level of the conductor and the vacuum level. The occupation of each energy level by electrons follows the Fermi-Dirac distribution, and most electrons have energy below the Fermi level at room temperature. Compared to thermionic emission or photoemission, where extra energy is absorbed by the electrons to overcome the barrier (φ), field emission is based on tunneling. An electric field (E_{FE}) applied across the vacuum bends the vacuum energy level downwards, as shown in Fig. 3.02, which increases the probability of the electrons inside the conductor of tunneling into the vacuum thereby enabling in electron emission.

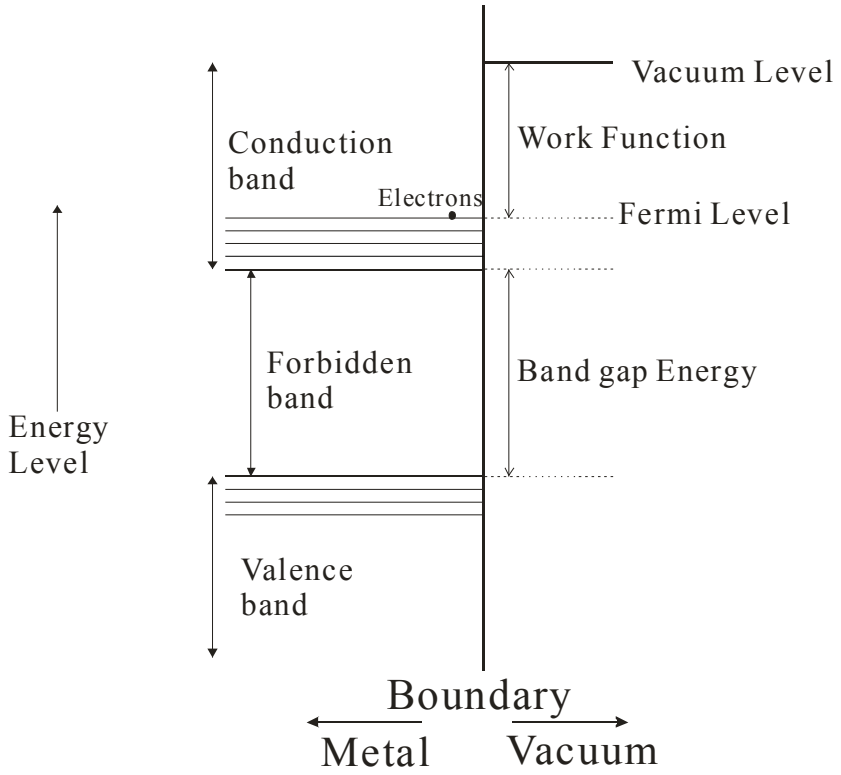

Figure 3.01: Energy band diagram for a conductor (e.g., Molybdenum)

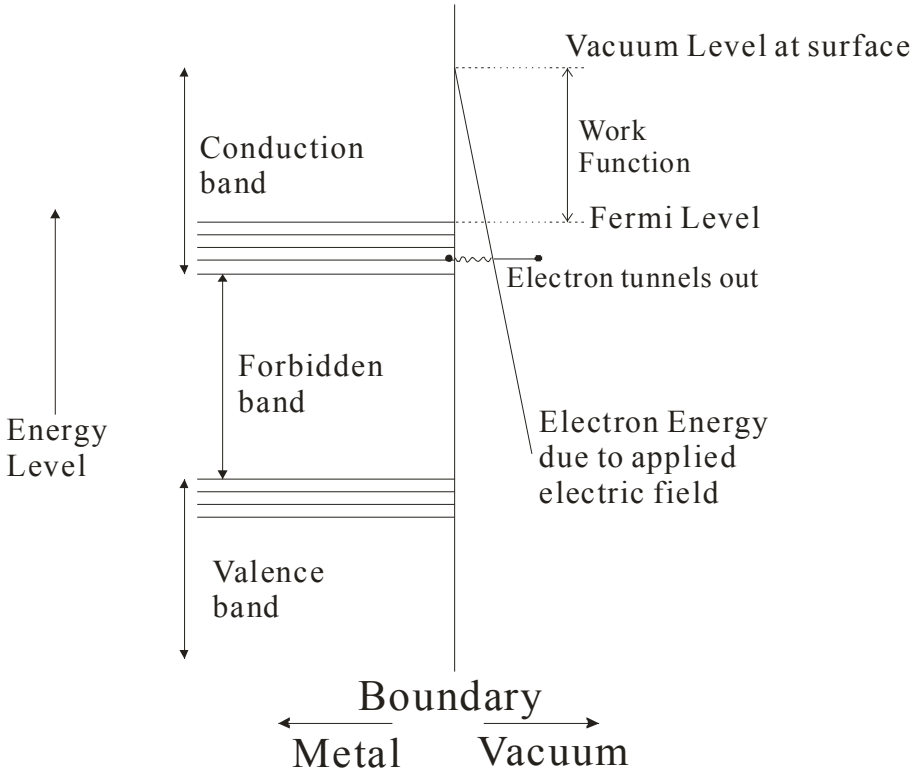

Figure 3.02: Energy band diagram with applied electric field. Electron is tunneling from metals.

The field emission process can be treated by considering a one-dimensional potential, which is assumed to have the same effect on a conduction electron as the actual metal. This potential was used in Fowler-Nordheim theory [87]. There are three contributions to this effective potential barrier: 1, within the metal the potential energy has some constant value, $-W_a$ relative to vacuum level. Its actual value is immaterial in the ordinary discussions of the theory; 2, an electric field, E_{FE}, is applied to draw the electrons out of the metal and gives a contribution of $-qE_{FE}x$ to the potential energy; 3, an electron outside a metal is attracted to the metal as a result of the charge it induces on the surface and the energy at position x is $-\frac{q^2}{4\pi\varepsilon_0 x}$, where q is the elementary charge, ε_0 is the

permittivity of free space and x is the distance between the electron and the surface of metal. These three contributions give

$$\begin{aligned} V(x) &= -W_a \qquad\qquad \text{where } x < 0 \\ &= -qE_{FE}x - \frac{q^2}{4\pi\varepsilon_0 x} \qquad \text{where } x > 0 \end{aligned} \tag{3.01}$$

for the effective potential energy. If we define W as the energy related to x-part, the field emission intensity, J, the electric current per unit area, is given by

$$J = q\int_{-W_a}^{\infty} P(W)dW \ , \tag{3.02}$$

where

$$P(W)dW = D(W)N(W)dW \ . \tag{3.03}$$

The function of $N(W)$ is called the supply function and $N(W)dW$ is the number of electrons with their energies of $W \sim W + dW$ incident on the surface per second per unit area; $D(W)$ is called the transmission coefficient and is the probability of penetration of the barrier. The product $P(W)dW$ gives the number with those energies that emerge from the metal per second per unit area. The supply function originates from the Fermi-Dirac distribution of electron gas statistics and the transmission coefficient is obtained from the time-independent Schrödinger equation as

$$\frac{d^2\Psi(x)}{dx^2} + \frac{2m}{\hbar^2}\big(W - V(x)\big) = 0 \tag{3.04}$$

through Wentzel-Kramers-Brillouin (henceforth, WKB) approximation method. Here we will not give the details of the solutions, which have been well documented.

Finally, at the absolute temperature of $T = 0$, the field emission intensity, J (in A/cm^2), is related to φ (in eV) and E_{FE} (in V/cm) by [88, 89]

$$J = 1.5 \times 10^{-6} \frac{E_{FE}{}^2}{\varphi} e^{10.4/\varphi^{1/2}} e^{-(6.44\times10^7 \varphi^{3/2}/E_{FE})}. \qquad (3.05)$$

An increase in temperature T will increase J from its value at $T = 0$, $J(0)$, by

$$\frac{J(T)}{J(0)} = \frac{\frac{\pi kT}{d}}{\sin\left(\frac{\pi kT}{d}\right)}, \qquad (3.06)$$

where k is the Boltzman's constant and d is a function [90] related to E_{FE} and φ. However, the effects of temperature on J are negligible compared to the effect of E_{FE}. Using the field emission from molybdenum (Mo) as an example, which has φ = 4.6 eV, a field strength of $E_{FE} = 6.0\times10^7$ V/cm can generate a current density of $J \approx 3\times10^6$ A/cm^2 at T = 0, while at room temperature (T = 300 K) J increases by only ~1.68 %.

3.2.2 Structure and operation of FEA

The FEA is a practical vacuum microelectronic device built to nanometer tolerance. Several technologies have been invented for manufacturing FEA for flat-panel display (FPD) applications. They include surface-conduction electron emitter (SCE) [91], carbon nanotube (CNT) [92], metal-insulator-metal (MIM) emitter as ballistic electron surface emitting device (BSD) [93, 94], metal-insulator-semiconductor (MIS) in high-efficiency electron emission devices (HEED) [95] and Spindt-type field emitters [96]. The characteristics of different FEA technologies vary in the angular distribution and intensity of the emitted electron beams. In field emission display (FED), the anode (phosphor) is usually biased with a positive potential at tens of thousands of volts, which accelerate the electrons to high speeds and minimize the time the electrons take to reach the anode. As a result, the lateral spread of the electron beam, which is due to the lateral velocity

component of the electrons emitted with an oblique angle, is insignificant. However in an image sensor, the potential on the bottom surface of the photoconductive target is proportional to the image signal, and is typically less than a few tens of volts. Therefore additional electron-optical focusing methods need to be developed to ensure that the electrons can reach the target without significant lateral spread. Furthermore, the intensity of the electron beam has to be sufficient for reading out the highest signal current generated in the HARP target.

Compared to the other types of FEA, Spindt-type field emitters have higher emission intensity and narrower angular distribution. They have also proven to be robust and stable over time [88]. Prototype Spindt-type FEDs of 8 inches [97] and 11.3 inches [98] have been presented, which are approaching the imager size required for medical FPI. For the remainder of this dissertation, we will use the typical characteristics of Spindt-type FEA as an example for our investigation. The most commonly used material for the Spindt tips is molybdenum (Mo). The cross-sectional view in Fig. 3.03 shows the typical geometry and structure of a single Spindt-type emitter tip. The FEA is enclosed in high vacuum (10^{-9} torr) during operation. To turn on field emission, the cone-shaped Mo cathode is biased at ground potential and a positive bias, V_g (40-100 V), is applied to the gate electrode. This bias condition results in a very high E_{FE} around the emitter tip due to its small area (~ 13Å^2) [88, 96] and causes field emission. As shown in Fig. 3.04, each pixel consists of a matrix of FE tips and different pixels of a FEA are addressed by orthogonal base and gate lines, i.e. a passive driving scheme. A prototype FEA with d_{el} = 50 μm with 17 × 17 tips in each pixel has been used in a 1″ diameter optical HARP FEA image sensor [2].

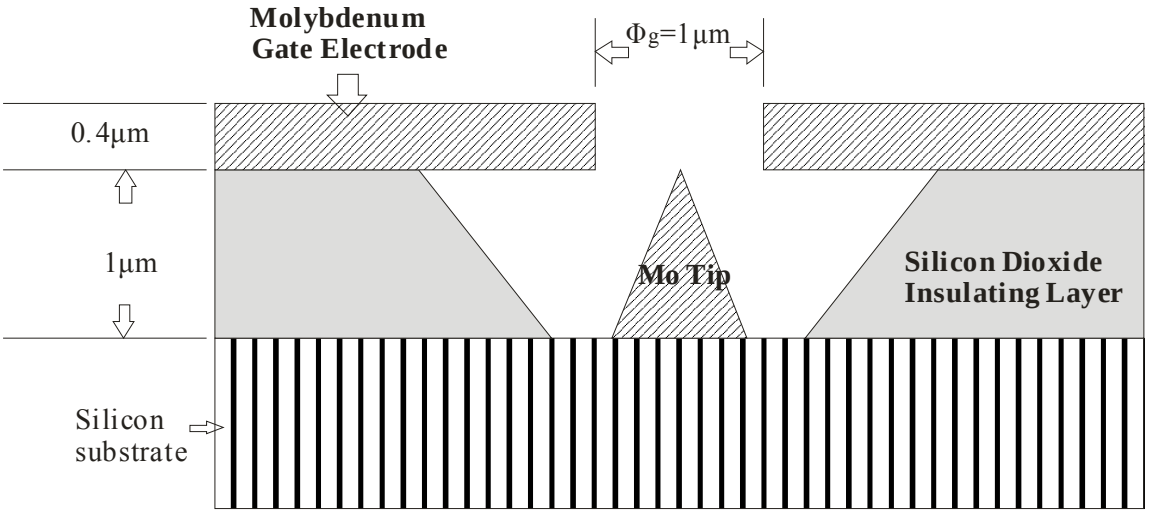

Figure 3.03: Cross-sectional view showing the structure of a single Sprindt-type Emitter.

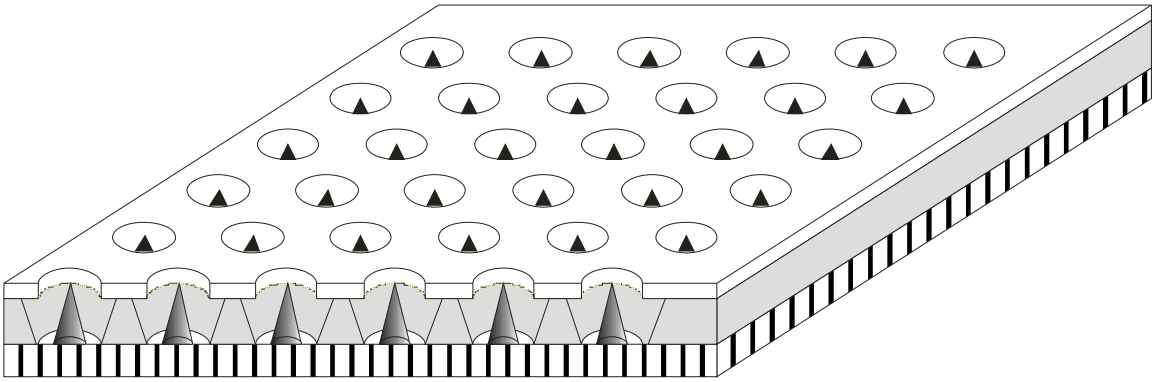

Figure 3.04: Schematic showing an example of FE tip arrangement on a Spindt-type FEA pixel.

The emission current as a function of gate voltage has been measured for such a FEA array. It has been found that the mesh electrode will absorb 45 % ~ 50 % of the total emission current [99]. Fig. 3.05 shows the effective emission current (I_e) as a function of V_g, which controls the field emission, from a sample of Spindt-type FEA. The emission current has ensured a wide dynamic range.

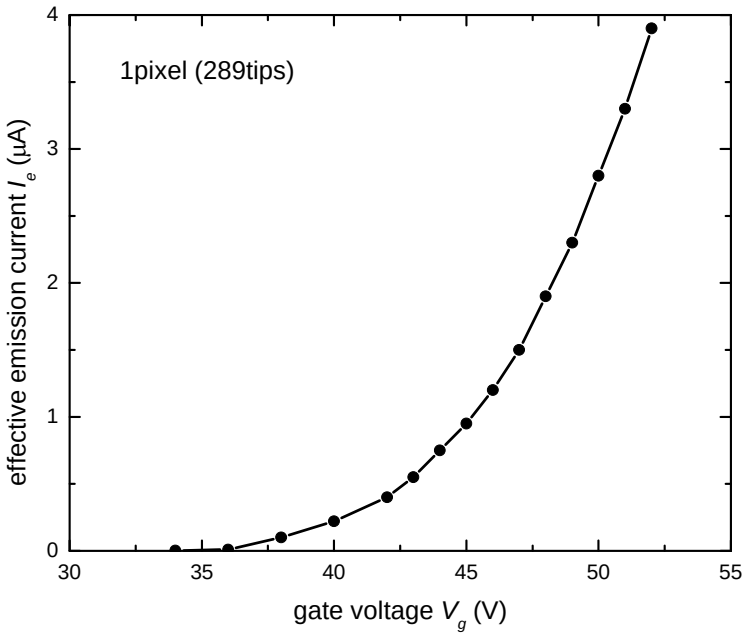

Figure 3.05: Effective emission current as a function of gate voltage on a FEA array with 17 × 17 tips/pixel.

The size of the FPI required for x-ray imaging is much larger than that for optical imaging, e.g. 20 cm × 25 cm for mammography. A pixel size of 50 μm would result in 4000 × 5000 pixels. This necessitates division of the ITO signal/bias electrode into multiple strips for two reasons: 1. One large ITO electrode would result in a large input load capacitance for the amplifier, which leads to increased electronic noise; 2. The large passive load (capacitance and resistance) of each gate and base line of a large area FEA results in driving pulse delay, which requires that each pixel be turned on for a typical time of 0.16 μs. A FEA matrix of 4000 × 5000 pixels would require 3.2 seconds to read out pixel-by-pixel. If the ITO electrode is divided into N_s stripes and each connected to a charge amplifier, as shown in Figs. 3.06 and 3.07, N_s pixels can be turned on simultaneously for parallel readout and increase the readout speed by N_s times. The major benefits of parallel beam readout are the decrease in readout lag, which will be discussed

later. For the discussion in the present paper, the parallel beam readout only has an impact on the pixel turn on time (t_p), which affects the pixel aperture function (to be discussed in subsection 3.3.4 and Section 3.4.4).

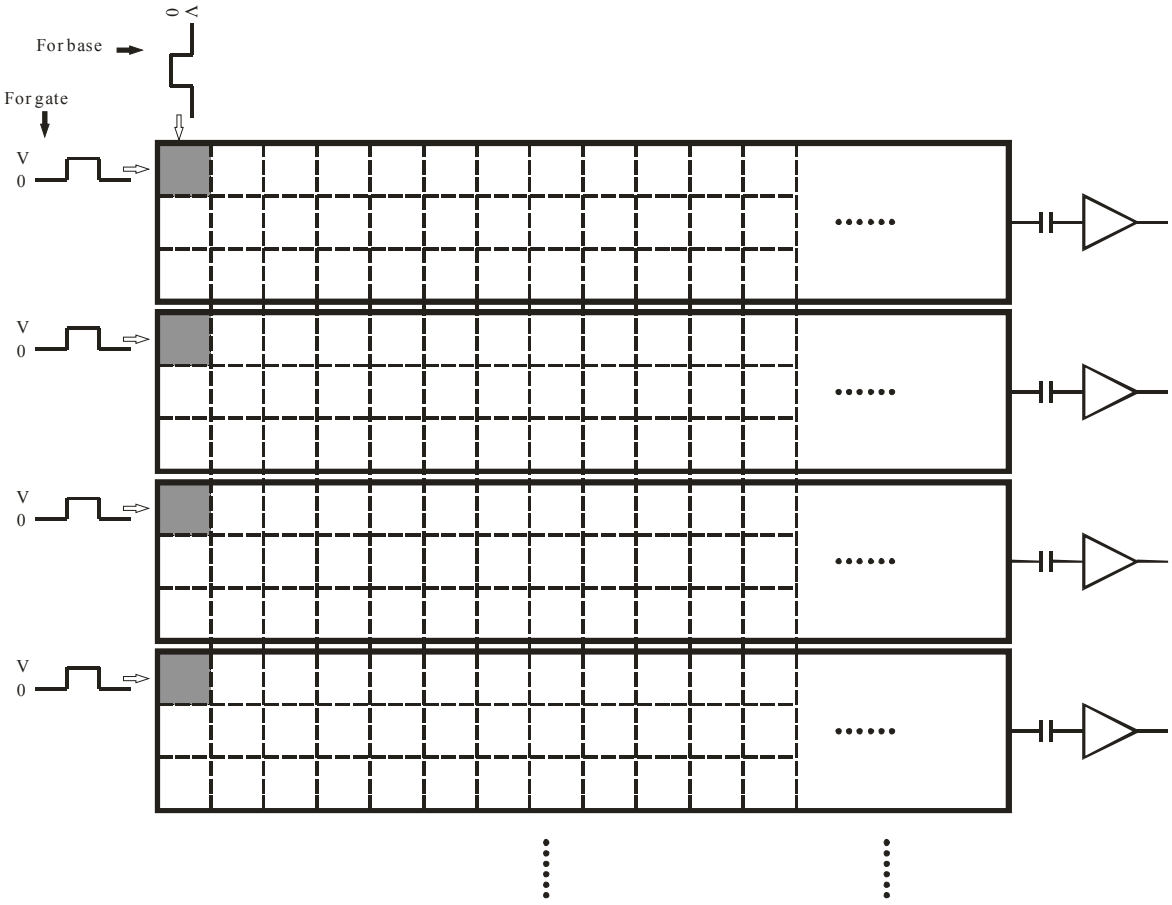

Figure 3.06: Schematic diagram showing the necessity of dividing the ITO electrode into multiple strips to enable parallel beam readout. The rectangle shows the ITO pattern, whereas the shaded squares show the pixels addressed simultaneously on the FEA.

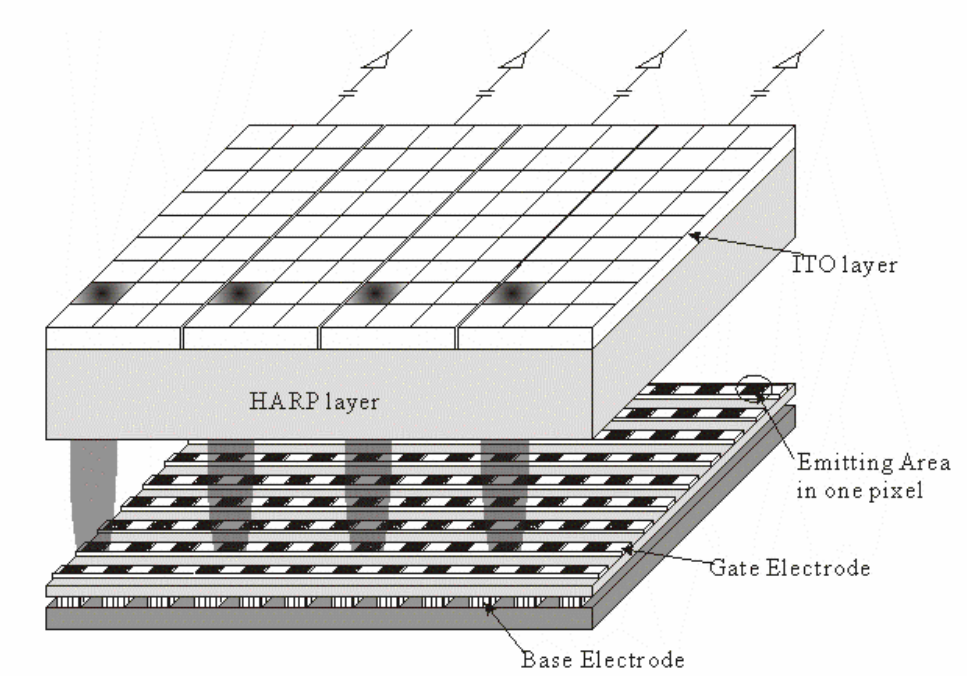

Figure 3.07: 3-D schematic view of the parallel beam readout method to show the simultaneous emission of electron beams from several pixels of the FEA, one for each ITO strip. The mesh electrode and CsI are removed from the SAPHIRE structure for clarity of illustration.

3.3 Materials and Methods

There are several factors affecting the spatial resolution of SAPHIRE: (1) the inherent resolution of the optically coupled scintillator-HARP (SHARP) combination; (2) the FEA pixel size; and (3) the lateral spread of the electron beams. In this section, we will first outline the inherent imaging performance of the SHARP combination in subsection 3.3.1, and then describe the lateral spread of electrons emitted from the FEA with different electron-optical designs (subsection 3.3.2). Finally in subsection 3.3.3, we will derive the shape and intensity of the electron beam for each pixel of the FEA from the FEA pixel design and the lateral spread of electrons. This information can be used to determine the aperture function of the FEA readout method.

3.3.1 Imaging performance of Scintillator-HARP (SHARP)

The SHARP combination determines the inherent x-ray imaging properties of SAPHIRE, and provides a reference for the spatial resolution requirement of the FEA readout. The dynamic range of SHARP and the inherent resolution of different types of CsI have been investigated previously [52]. However the dynamic range of SHARP affects the configuration for FEA operation and the spatial resolution of the FEA needs to be compared with the inherent resolution of SHARP. Hence in this section we will briefly describe our method developed previously for the determination of inherent resolution and dynamic range of SHARP, and make modifications needed for the unique readout properties of SAPHIRE. We will use design parameters suitable for mammography as an example.

3.3.1.1 Inherent spatial resolution

The inherent resolution of SHARP is dominated by the blur in the structured CsI scintillator. The photon detection and avalanche processes in HARP do not introduce additional blur because the bias field E_{Se} in HARP draws the image charge directly to the bottom surface without lateral spread. This has been experimentally demonstrated in high definition optical HARP that operates with an effective pixel size of 10 ~ 20 μm [61, 62]. It was found in our previous work that the HR type CsI provides significant improvement in modulation transfer function (MTF) compared to the high light (HL) type CsI layers. The image blur in HR CsI also has less depth dependence, which results in improved DQE at high spatial frequencies. The only disadvantage with HR CsI is the lower light output, which is 64% of that in HL CsI [3]. However the lower light output does not

degrade the Swank factor for HR CsI, which is ~ 91 ~ 93 % for mammographic x-ray energies lower than the K-edge of CsI (33.2eV for I and 36.0eV for Cs) [3, 100]. Therefore the avalanche gain of SAPHIRE can overcome the limitation of the low light output of HR CsI and realize its advantages for high resolution imaging. The imaging performance of a 150 μm HR CsI layer will be used for our discussion in this paper.

3.3.1.2 Dynamic range

Since the avalanche gain of HARP is programmable by changing the bias field. E_{Se}, the SHARP combination has a wide dynamic range. In this chapter, we followed the methods in our previous work and calculated the variation of the bottom surface potential (V_t) of the HARP target based on a proposed detector design for mammography with an *a*-Se thickness of d_{Se} = 8 μm and HR type CsI of 150 μm. The relationship between image charge generated by SHARP under different E_{Se} bias condition has been established through the development of a cascaded linear system model for indirect AMFPI with avalanche gain [1, 52]. The major difference between SAPHIRE and the TFT readout method is that the pixel capacitance in SAPHIRE is only attributed to the HARP target itself, i.e. no additional pixel storage capacitor as in the TFT readout method. Therefore the cascaded linear system model was modified to reflect this difference. The relation between V_t and the x-ray exposure under different E_{Se} bias condition is given by:

$$V_t = \frac{\gamma \eta g_{av} E_{ab} q d_{Se}}{W \varepsilon_{Se} \varepsilon_0} . \qquad (3.07)$$

Here, Eq. 3.07 is actually the same as the Eq. 2.15 on page 43, except here we calculated the pixel response in units of potential instead of charge. The avalanche gain g_{av} follows

Eq. 2.06 with the parameters determined in the previous chapter. E_{ab} contains the information of exposure, which is calculated through Eq. 2.16 on page 43.

3.3.2 Lateral spread of FEA readout

The geometric arrangement of FE tips on each pixel of the FEA determines the area of emission. However, the spatial resolution of the FEA readout is determined by the intensity of the electron beam when it reaches the bottom surface of the HARP target as shown in Fig. 3.08, which depends strongly on the lateral spread of the electrons with an emission angular range of ~ 40 - 50° [2].

The lateral spread of electrons is the integration of the lateral component of the velocity, v_x, over the time t_{gt} it takes for the electron to travel from the gate electrode to the target. Since the value of V_t is on the order of several volts, the electric field, E_z, between HARP and FEA is not sufficient to drive the electrons to a reasonable speed. Therefore it is necessary to insert a mesh electrode with several hundred volts of potential V_m between the HARP target and the FEA. As shown in Fig. 3.08, the mesh electrode will accelerate the axial velocity component v_z of the electrons thus shorten t_{gt}. After the electrons transmit through the mesh electrode, they decelerate due to the reversed electric field, and only those electrons with sufficient initial value of v_z can reach the target. The other electrons decelerate to $v_z = 0$ before reaching the target and return to the mesh electrode. If we assume the same initial energy for electrons emitted with different angles (θ), the electrons with smaller θ have higher initial v_z. Thus, there exists a critical emission angle θ_c, within which the emitted electrons can reach the target.

To reduce the lateral spread of electrons, different electron-optical focusing designs have been investigated to reduce either v_x or t_{gt}. In this paper three different electron-optical designs were investigated: (1) mesh electrode only; (2) magnetic focusing and (3) electrostatic focusing in addition to the mesh electrode. For each design, we use a two-step approach to determine the spatial resolution of electron beam: (1) determine the maximum lateral travel distance (LS_{max}) of a single electron emitted from a single FE tip; and (2) compute the spreading of the electron beam emitted from one pixel of the FEA, which includes a two-dimensional array of tips. These two steps will be described in this subsection (3.3.2) and the next two subsections (3.3.3 and 3.3.4) separately.

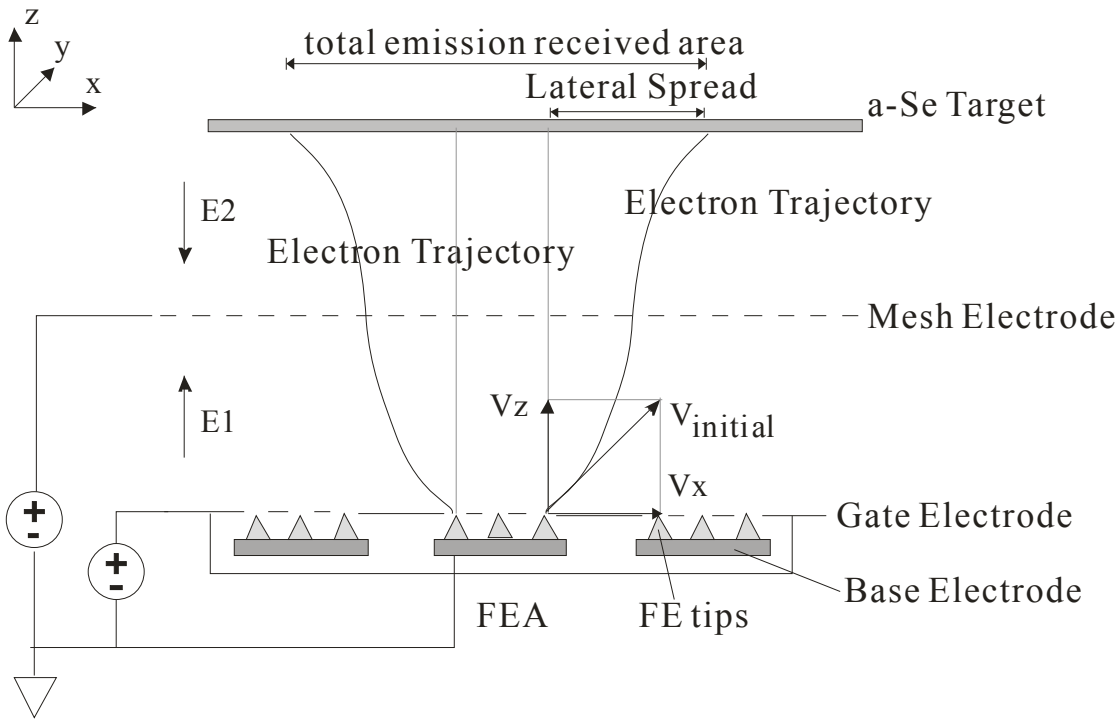

Figure 3.08: Schematic diagram showing the lateral spread of electron beams emitted from the FEA. The emitted electrons neutralize the image holes accumulated on the bottoms surface of HARP target layer. It induces the same amount of reduction of accumulated electrons on the other side of HARP layer. This reduction is read out through ITO electrode as signal.

3.3.2.1 Mesh-electrode-only

As described above, the simplest method to reduce t_{gt} and subsequently, the lateral spread, is to insert a mesh electrode halfway between the HARP target and the FEA, as shown in Fig. 3.08. If we assume that all electrons have the same initial energy $E = qV_g$ after emission from the gate electrode [99], the lateral spread can be derived analytically as shown in Appendix B, and is given by

$$LS = 2\sqrt{V_g}\sin\theta \cdot L_{gm}\left(\frac{\sqrt{V_m - V_g\sin^2\theta} - \sqrt{V_g}\cos\theta}{V_m - V_g}\right) + 2\sqrt{V_g}\sin\theta \cdot L_{mt}\left(\frac{\sqrt{V_m - V_g\sin^2\theta} - \sqrt{V_t - V_g\sin^2\theta}}{V_m - V_t}\right), \quad (3.08)$$

where L_{gm} and L_{mt} are the gate-mesh and mesh-target distances, respectively; V_t and V_g are potential on target and gate electrode, respectively. The LS_{max} is the value of lateral spread with critical angle θ_C, which is determined by V_t and V_g of the FEA:

$$\theta_C = \arcsin\left(\sqrt{\frac{V_t}{V_g}}\right). \quad (3.09)$$

Then LS_{max} can be obtained by substituting θ in Eq. 3.08 with θ_C in Eq. 3.09:

$$LS_{\max} = 2\sqrt{V_t}\cdot L_{gm}\left(\frac{\sqrt{V_m - V_t} - \sqrt{V_g - V_t}}{V_m - V_g}\right) + 2\sqrt{V_t}\cdot L_{mt}\left(\frac{1}{\sqrt{V_m - V_t}}\right). \quad (3.10)$$

Eq. 3.10 shows that $LS_{\max}$ depends on the geometry and the operating conditions of the FEA, e.g. L_{gm}, L_{mt}, V_m and V_g, as well as on the x-ray exposure (i.e. V_t).

3.3.2.2 Magnetic focusing

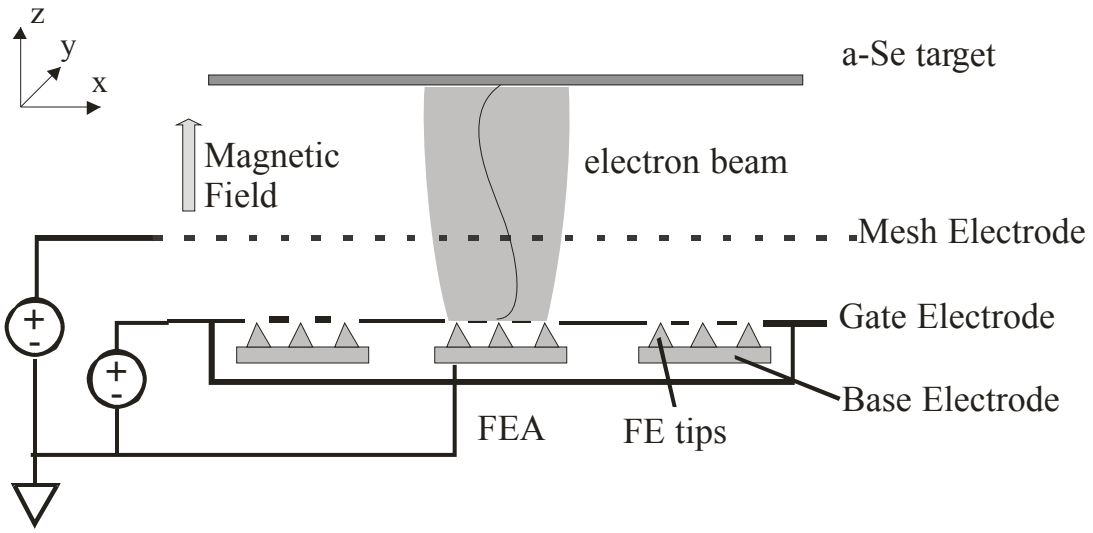

Figure 3.09: Cross-sectional view showing electron trajectory under magnetic focusing.

The magnetic focusing design was originally proposed and implemented for a 1″ optical HARP FEA sensor [101]. The concept is shown in Fig. 3.09. In addition to the mesh electrode, a constant and uniform magnetic field, *B*, is applied in the z-direction through a ring shaped permanent magnet which is placed around the FEA sensor. The magnetic field results in a spiral trajectory for the emitted electrons. The projection of the electron trajectory in the horizontal plane (x-y plane in Fig. 3.09) is a circle. As shown in the derivation in Appendix C, the lateral spread of the electron depends on the diameter of the circle, which is determined by the strength of the magnetic field, *B*, through:

$$LS = \frac{2}{B}\sqrt{\frac{2mV_g}{q}}\sin\theta \cdot \left|\sin\left(\frac{qBt_{gt}}{2m}\right)\right|, \tag{3.011}$$

where m is the mass of an electron, and t_{gt} is given by

$$\begin{aligned} t_{gt} = {} & \frac{L_{gm}}{V_m - V_g}\sqrt{\frac{2m}{q}}\left(\sqrt{V_m - V_g\sin^2\theta} - \sqrt{V_g}\cos\theta\right) \\ & + \frac{L_{mt}}{V_m - V_t}\sqrt{\frac{2m}{q}}\left(\sqrt{V_m - V_g\sin^2\theta} - \sqrt{V_t - V_g\sin^2\theta}\right) \end{aligned}. \tag{3.12}$$

It is difficult to obtain an analytical expression of LS_{max} from Eq. 3.11 for electrons with different θ because lateral spread in Eq. 3.11 is not a monotonic function of θ and LS_{max} does not necessarily correspond to $\theta = \theta_C$. The values for LS_{max} were determined by calculating lateral spread as a function of θ at different operating conditions.

Although magnetic focusing may not be practical for FPI in medical imaging due to the difficulty in maintaining a uniform magnetic field over a large area, the fundamental properties of magnetic focusing were investigated here for completeness and ease of comparison.

3.3.2.3 Electrostatic focusing

Electrostatic focusing is feasible for large area SAPHIRE. The concept of electrostatic focusing proposed for SAPHIRE is shown in Fig. 3.10. An additional (focusing) electrode layer is added on top of the FE tips and this structure is referred to as the double-gated Spindt-type emitter [88]. Both electrodes are made of Mo through photolithography and are separated by an insulating layer (e.g. SiO_2). The lower Mo layer is the regular gate electrode for the control of field emission, while the upper Mo layer acts as an electrostatic focusing lens. To deflect the electrons with large θ back to the vertical direction, a focusing lens potential V_L that is much lower than V_g is applied. The choice of V_L depends on the geometry of the double-gated tip.

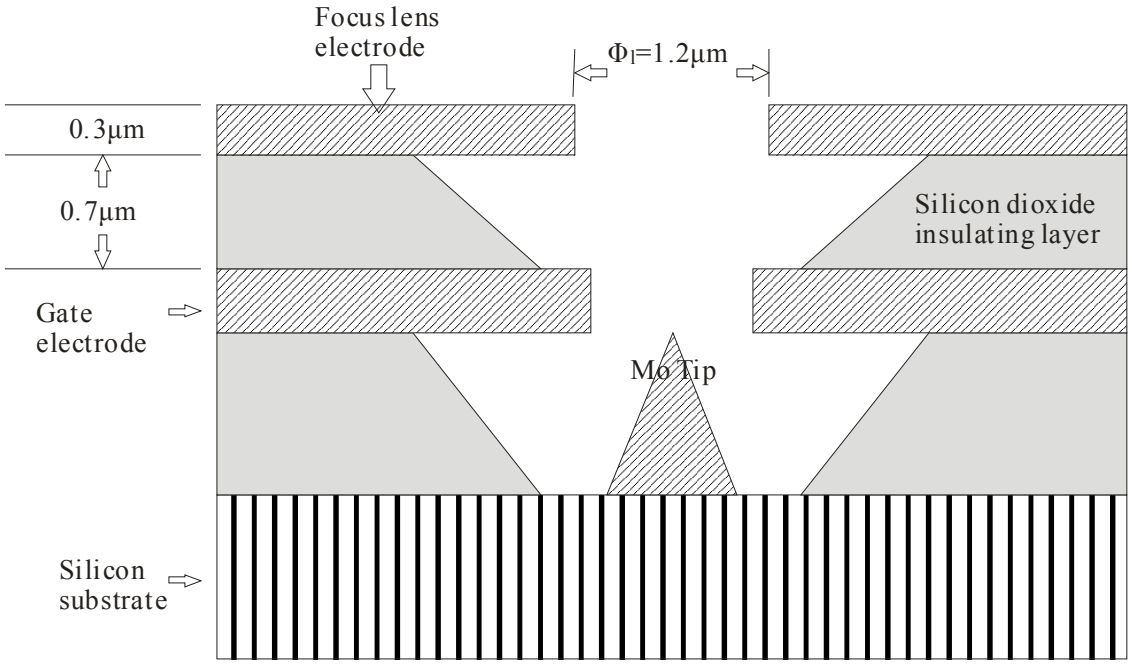

Figure 3.10: Cross-sectional view showing the structure of a double-gated Sprindt-type Emitter with focusing electrodes, which defect the electrons with large emission angle to axial direction.

The lateral spread of electrons with electrostatic focusing cannot be calculated analytically. Instead, the electron trajectory was simulated using finite element analysis (COMSOL Multiphysics®), which was used to solve for the electric field distribution between the HARP target and the FEA. Since the size of FE tips (~1 μm) is three orders of magnitude smaller than the distance between the target and the gate L_{gt} (~1 mm), variable resolution was used to set up the finite element mesh in the simulation. The element size chosen for the vicinity of the FE tip was ~1 nm to ensure accurate simulation of electron trajectory with the focusing lens. Since the structures of each FE tip were identical and independent, the simulation was performed on a single FE tip with circular symmetry about the tip. With axial distance of > 2 μm above the focusing electrode, the electric field becomes essentially parallel; therefore the element size for simulation was increased gradually to ~1 μm to minimize the simulation time. The

trajectories of a single electron emitted at different angles were determined with separate runs of the simulation. The effects of possible interaction between electrons as they traverse between the FEA and the HARP target were not included in the simulation. These effects were estimated and found to be negligible. They will be discussed in section 3.4.5. The electron emission intensity and relationship of lateral spread versus θ ,LS(θ), determines the beam shape for a single FE tip, which will be used in the next section to form the beam intensity profile for a pixel with a 2D array of FE tips.

3.3.3 Electron beam intensity

The spatial intensity distribution of the electron beam as it reaches the target, $I(x,y)$, was calculated for each pixel of the FEA with d_{el} = 50 μm×50 μm. An array of 17 × 17 FE tips was arranged in a total emission area of 20 μm × 20 μm in the center of the pixel.

The electron beam intensity from a single tip, $I_0(x,y)$, was first obtained by substituting the inverse of the relationship between lateral spread and θ in subsection 3.3.2, i.e. $\theta = LS^{-1}(x, y)$, into the angular intensity distribution of field emission $I_\theta(\theta)$ from a single tip, and then converting the result to Cartesian coordinates:

$$I_0(x,y) = I_\theta\left(LS^{-1}(x,y)\right). \tag{3.13}$$

The distribution of $I_\theta(\theta)$ used in our calculation is shown in Fig. 3.10 and was adapted from the simulation and experimental measurements by Itoh *et. al.* for Spindt-type FEA. The beam intensity for one pixel was then calculated by integrating $I_0(x, y)$ over all the FE tips in the x and y directions with $N_x = N_y = 17$:

$$I(x,y) = \sum_{N_x}\sum_{N_y} I_0(x - n_x d_t, y - n_y d_t). \tag{3.14}$$

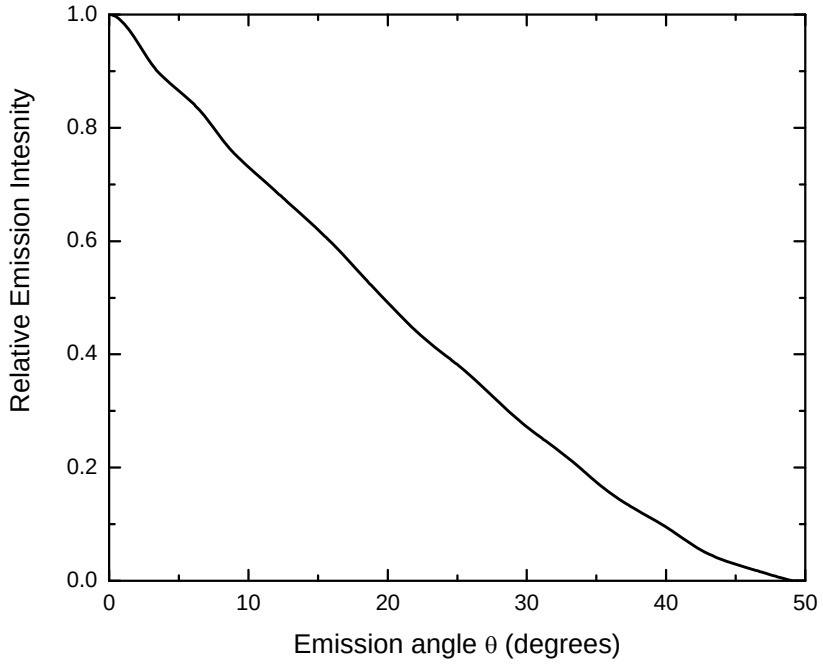

Figure 3.11: Angular distribution of electrons in Spindt-type field emitters, adapted from ref [2].

3.3.4 Pixel aperture function

The pixel aperture function of the FEA readout method, $MTF_{FEA}(f_x, f_y)$, was determined from the Fourier transform of the spatial distribution of the image charge on the target, $Q_a(x, y)$, that was read out by each FEA pixel. $Q_a(x, y)$ is given by the integral of $I(x, y)$ within the pixel readout time, t_p:

$$Q_a(x, y) = \int_0^{t_p} I(x, y)dt \, . \tag{3.15}$$

During electron beam readout, the target potential V_t decreases with time as the electrons reach the target. Since $I(x, y)$ is V_t dependent, $Q_a(x, y)$ was calculated numerically by dividing t_p into small steps and updating $I(x, y)$ in real-time. After $Q_a(x, y)$ was calculated for each focusing method, $MTF_{FEA}(f_x, f_y)$ was obtained through the two-dimensional Fourier transform:

$$\mathrm{MTF}_{\mathrm{FEA}}(f_x, f_y) = \frac{\left|\mathrm{FT}\left(Q_a(x,y)\right)\right|}{\mathrm{MTF}_{\mathrm{FEA}}(0,0)}. \tag{3.16}$$

The presampling MTF of SAPHIRE was then calculated by multiplying the $\mathrm{MTF}_{\mathrm{FEA}}(f_x, f_y)$ by the MTF of the SHARP combination:

$$\mathrm{MTF}_{SAPHIRE} = \mathrm{MTF}_{SHARP} \times \mathrm{MTF}_{FEA}. \tag{3.17}$$

3.4 Results and discussion

3.4.1 Imaging performance of Scintillator-HARP (SHARP)

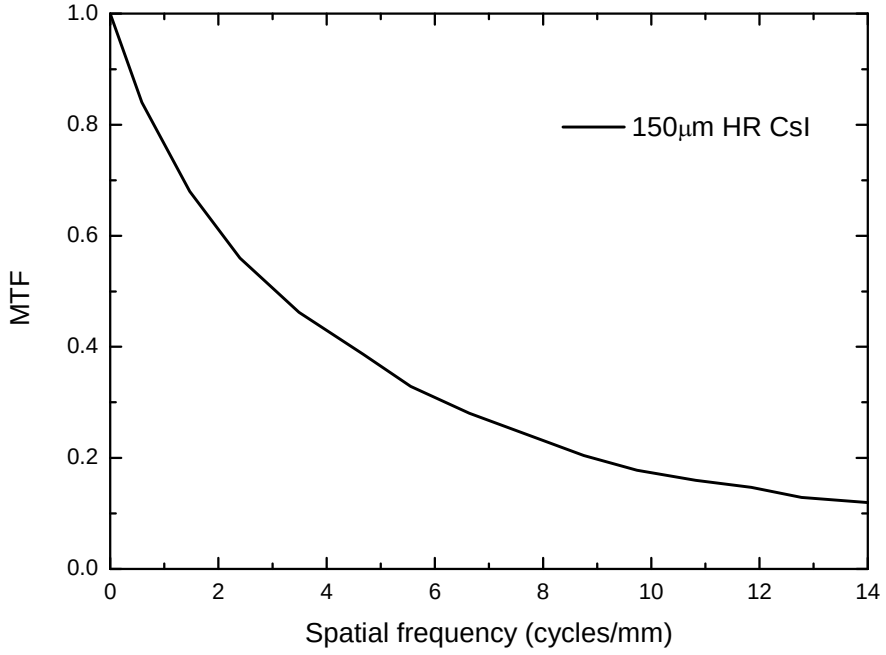

Figure 3.12: Presamling MTF of the CsI layers for 150 μm HR type CsI layers (adapted from Ref. [3])

Fig. 3.12 shows the measured presampling MTF for a 150μm thick HR type CsI layer [3]. This result has been corrected for the pixel aperture function of a 48 μm pixel size CMOS sensor used in the measurement. The MTF is 36% and 17% at 5 and 10

cycles/mm, respectively. This will be compared with the aperture function of the FEA readout in subsection 3.4.3.

Our previous study [52, 53] of the dynamic range of SHARP showed that by varying the avalanche gain between 12 and 46, x-ray quantum noise limited performance and a DQE value that is independent of x-ray exposure can be obtained for both screening and mammography tomosynthesis applications. Using the previously calculated range of image charge generated by SHARP, and the unique pixel capacitance of SAPHIRE, the range of V_t corresponding to the operating conditions is calculated using Eq. 3.07. Figs. 3.13 and 3.14 show the values for V_t as a function of x-ray exposure for tomosynthesis and screening mammography, respectively. The operating conditions chosen are listed in Table 2.01. Due to the change in g_{av}, the range of V_t for tomosynthesis and screening mammography is comparable, which is the major advantage of SAPHIRE versus a photoconductor with constant high gain. The maximum V_t behind the breast, where the estimated detector exposure is 50 mR near the skin line for screening mammography, is expected to be ~ 50 V. However, outside the region of the breast where the detector is receiving raw radiation exposure, V_t can be as high as 150 V. This range of V_t is considered in the calculation of spatial resolution of the FEA readout method in the next section.

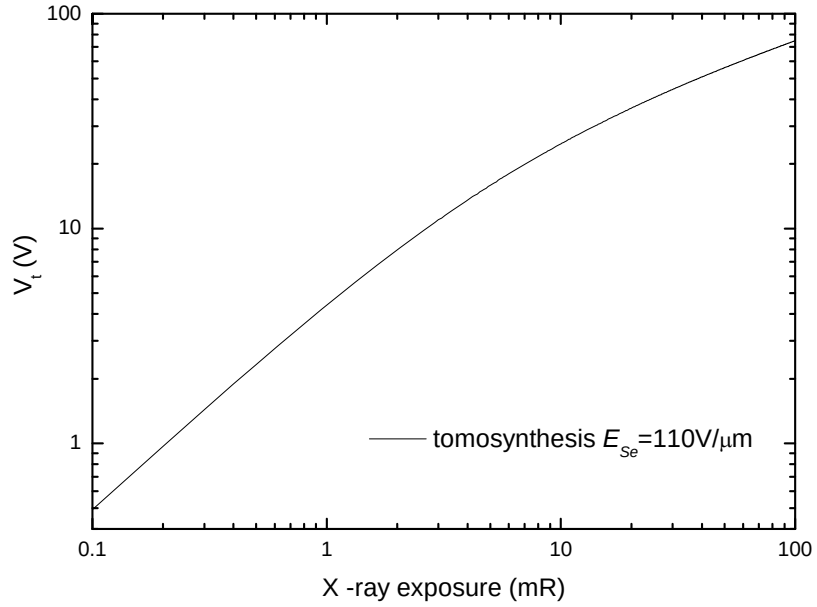

Figure 3.13: Calculated target potential V_t of the mammography detector for tomosynthesis with minimum exposure of 0.1 mR and E_{Se}=110V/μm, η=0.36 and g_{av}=46.

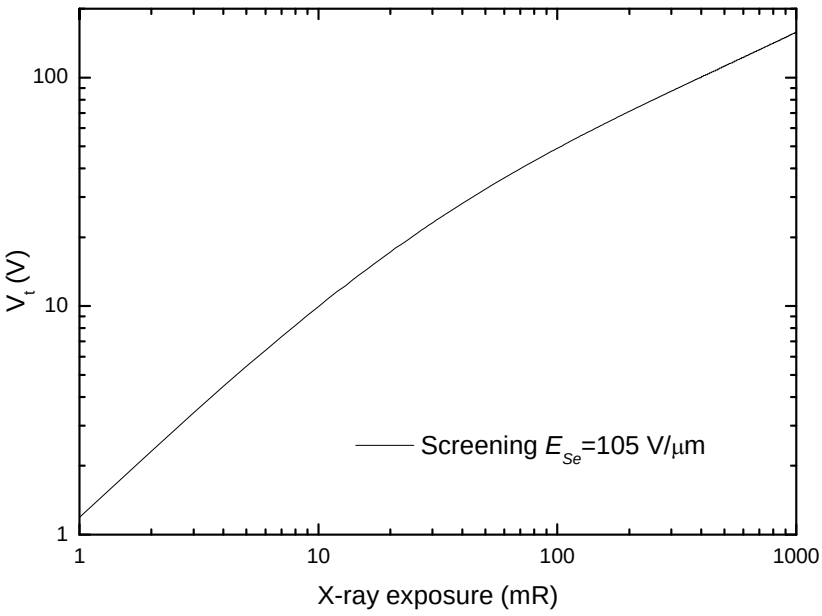

Figure 3.14: Calculated target potential V_t of the mammography detector for screening mammography with minimum exposure of 0.1 mR and E_{Se}=105V/μm, η=0.35 and g_{av}=12.

3.4.2 Lateral spread of FEA readout

The lateral spread of electrons emitted from a single tip for all three electron-optical designs were calculated using the methods described in subsection 3.3.2. Fig. 3.15 shows an example of the calculation result, which is a comparison between the electron trajectory of mesh-electrode-only and the electrostatic focusing designs. It shows that focusing can reduce lateral spread significantly (from 59 μm to 16.9 μm). Magnetic focusing can also help reduce lateral spread moderately, resulting in a value that is between the other two focusing methods. Here we discuss the results in detail for each design separately.

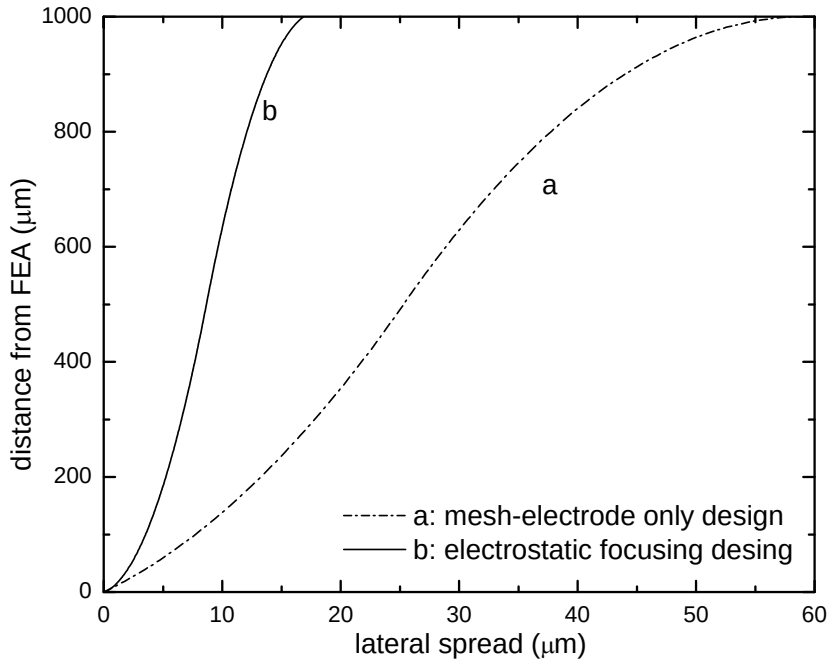

Figure 3.15: Electron trajectories within the vacuum space between the FEA and the HARP target for different electron-optical designs. The mesh electrode is placed half-way between the FEA and the target, i.e. 500 μm from the FEA. The detector geometry and bias conditions are shown in Table 3.01.

3.4.2.1 Mesh-electrode–only

The lateral spread for mesh-electrode-only design was calculated using Eq. 3.08 and the trajectory was calculated using Eqs. B.07 and B.11 in Appendix B. The detector geometry and bias conditions, i.e. V_g, V_m, L_{gm} and L_{mt}, are listed in Table 3.01. The example result in Fig. 3.15 shows that lateral spread is 59 μm at V_t = 0.4 V, which corresponds to a critical angle θ_c of 5.74°. This means that only a small fraction of the emitted electrons is utilized for readout. With an increase in V_t, the efficiency increases by drawing electrons with larger θ to the target, however at the cost of increased LS_{max}, which becomes 444 μm with V_t = 20 V. The major limitation of the mesh-electrode-only design is that lateral spread varies significantly as a function of signal, which will lead to image artifact due to non-uniformity in spatial resolution that cannot be easily corrected. Furthermore, while this magnitude of lateral spread may be acceptable for general radiographic applications with pixel size ranging from d_{el} = 150 ~ 200 μm, it is not adequate for mammography with d_{el} = 50 ~ 100 μm. As shown in Eq. 3.08, lateral spread can be reduced by increasing V_m or decreasing L_{gt}. However, this makes the detector much more difficult to manufacture. Therefore, for mammography, additional focusing without reduction in L_{gt} is desirable.

Table 3.01: Detector geometry and bias conditions used for all three electron-optical designs

	Mesh-electrode only	Magnetic focusing B = 0.12 T	Electrostatic focusing V_L = -2V
V_g (V)	40	50	40
V_m (V)	350	300	350
L_{gm} (mm)	0.5	0.9	0.5
L_{mt} (mm)	0.5	0.9	0.5

3.4.2.2 Magnetic focusing

The lateral spread with magnetic focusing was calculated using Eq. 3. 11. A previous study has shown that there exist optimal *B* values that minimize lateral spread [101]. The choice of *B* value depends on detector geometry and bias conditions. Shown in Fig. 3.16 are the lateral spread values as a function of *B* with V_t = 0.4V, 10V and 20V at $\theta = \theta_C$. The calculation was performed using the geometry and bias conditions listed in Table 3.01. The figure shows that optimal *B* values correspond to multiples of complete rotations of electrons in its spiral trajectory, e.g. 360° and 720°. The *B* value that provides the first minimum is in the range of 0.11 – 0.13 T. With a fixed *B* value**,** lateral spread depends on V_t and θ, and is not always at the minimum. Shown in Fig. 3.17 are the calculated lateral spreads as a function of θ (up to θ_c) for different value of *B* and V_t. The set of curves for each *B* value can be used to determine LS_{max} as a function of V_t, and the results for *B* = 0.12T are shown in Fig. 3.18. Despite the V_t dependence, the range of lateral spread values is much smaller than that for the mesh-electrode-only design at the same V_t.

As noted in Table 3.01, the detector parameters chosen for the magnetic-focusing design, which are identical to those used in the prototype 1″ optical FEA sensor [101] are different from the other two focusing designs. The distances between different electrodes are noticeably larger. This is because lateral spread for magnetic-focusing does not depend strongly on the separation of different electrodes due to the spiral trajectory of the electrons. For a given set of detector geometries and bias conditions, lateral spread can be minimized by optimizing the *B* value.

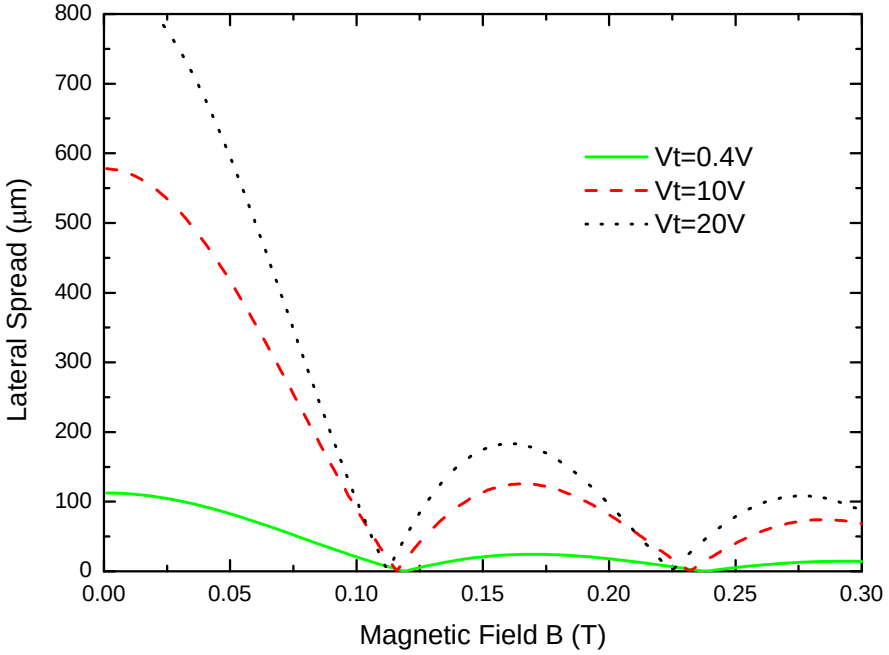

Figure 3.16: Lateral spread of electrons with magnetic focusing as a function of magnetic field B with different target potentials V_t at critical emission angle θ_C. Other conditions are listed in Table 3.01.

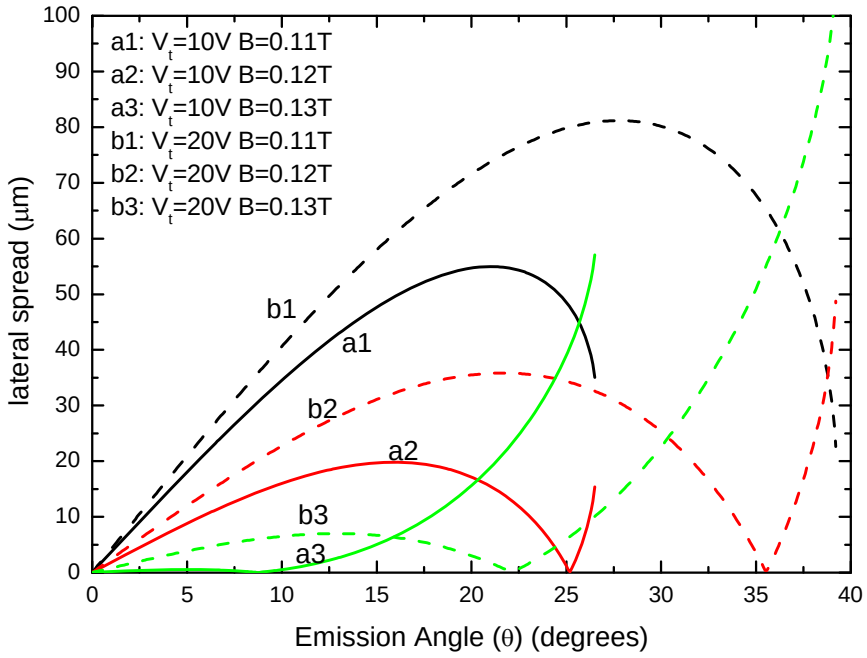

Figure 3.17: Lateral spread of electrons with magnetic focusing as a function of the emission angle θ with different B and target potential V_t. Other conditions are listed in Table 3.01.

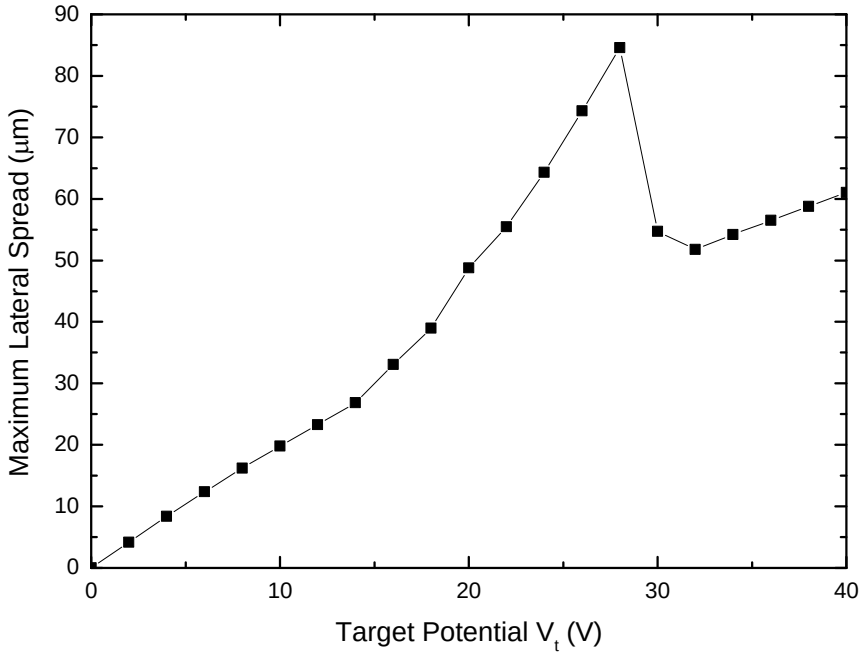

Figure 3.18: LS_{max} of electrons with magnetic focusing as function of target potential V_t at B = 0.12T. Other detector parameters are listed in Table 3.01.

3.4.2.3 Electrostatic focusing

The electron trajectory for electrostatic focusing was obtained using finite element analysis. The example result shown in Fig. 3.15 indicates that electrostatic focusing can reduce lateral spread significantly. Here we will further examine the dependence of electrostatic focusing on different FEA operating conditions:

a. Electrostatic focusing lens potential V_L

With electrostatic focusing, the major factor affecting the trajectory of emitted electrons is the bias potential, V_L, on the electrostatic focusing lens electrode. In general, $V_L < V_g$ is required to produce the focusing effect. Since the focusing lens electrode is located < 1 μm away from the gate, V_L has to be chosen carefully to avoid inadequate

focusing. The diagrams in Fig. 3.19 show qualitatively the effect of V_L on the trajectory of electrons emitted from different angles. Our strategy in the choice of V_L is to minimize under-focusing, which leads to larger lateral spread and loss of electrons. Our simulation of electron trajectories with different V_L showed that V_L = -2V provides the best compromise, and this value was used for calculating the results in Fig. 3.20.

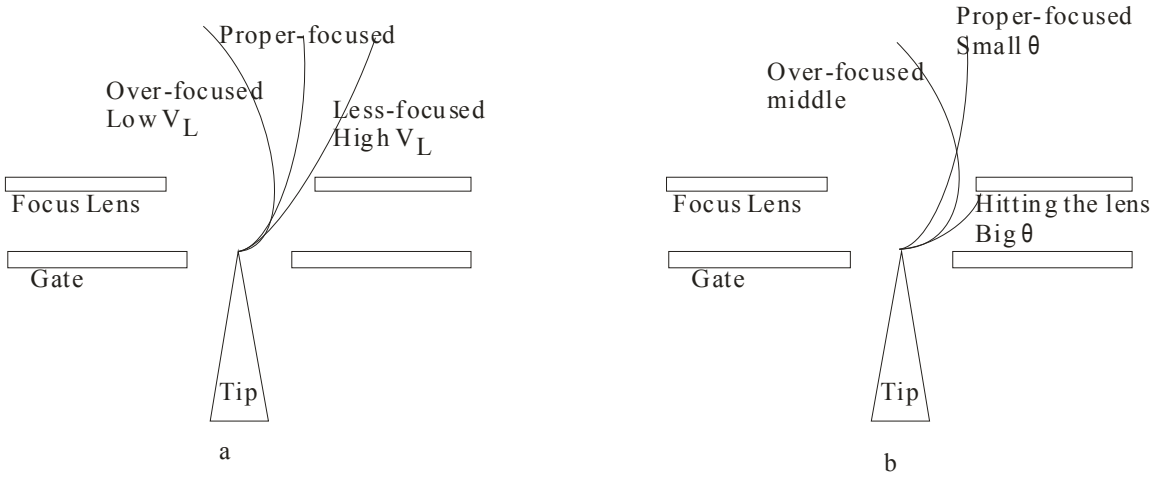

Figure 3.19: Conceptual electron trajectories under different V_L bias conditions: (a) For electrons emitted with the same angle, different V_L results in different lateral spread; (b): For the same V_L, electrons emitted with different angle results in different lateral spread.

Shown in Fig. 3.20 are the lateral spreads as a function of θ for the operating conditions in Table 3.01 and FE tip geometry in Fig. 3.10. The LS_{max} occurs at θ = 20°. This is because electrons emitted with larger θ are deflected by the focusing lens and result in lower lateral spread. Electrons emitted with θ > 28° are absorbed by the lens electrodes in this simulation setting.

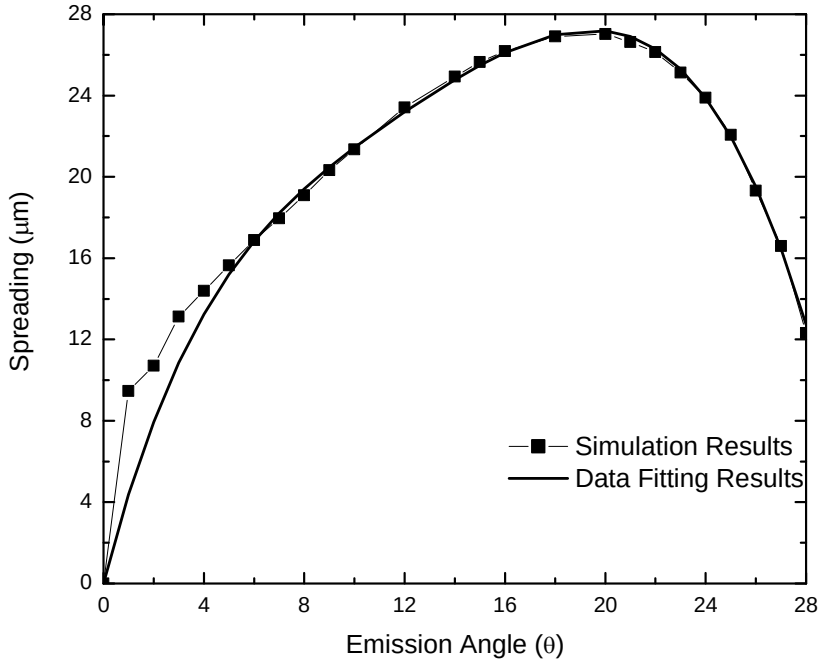

Figure 3.20: Lateral spread of electrons with electrostatic focusing design as a function of electron emission angle θ under the operating conditions in Table 3.01 and FE tip geometry in Fig. 3.10. The target potential V_t = 0.6 V.

To facilitate the calculation of the pixel aperture function in the next section, the relationship between lateral spread and θ shown in Fig. 3.20 was fitted with a 6th order polynomial function, and the fitted result is shown for comparison in the same graph**.**

b. HARP target free surface potential V_t

In the previous two focusing designs, the dependence of lateral spread on V_t is significant (larger than the desired pixel size), and would result in non-uniformity in spatial resolution. The results of the lateral spread calculation for electrostatic focusing are shown in Fig. 3.21 as a function of V_t for two emission angles: θ = 5° and 20°. The figure shows that lateral spread decreases as V_t increases due to the reduction in electron travel time t_{gt}. However the variation in lateral spread is < 2 μm over a V_t range of 0 ~ 30

V. Since this variation is much smaller than the desired pixel size, lateral spread can be regarded as essentially independent of V_t, which leads to uniform spatial resolution across the image.

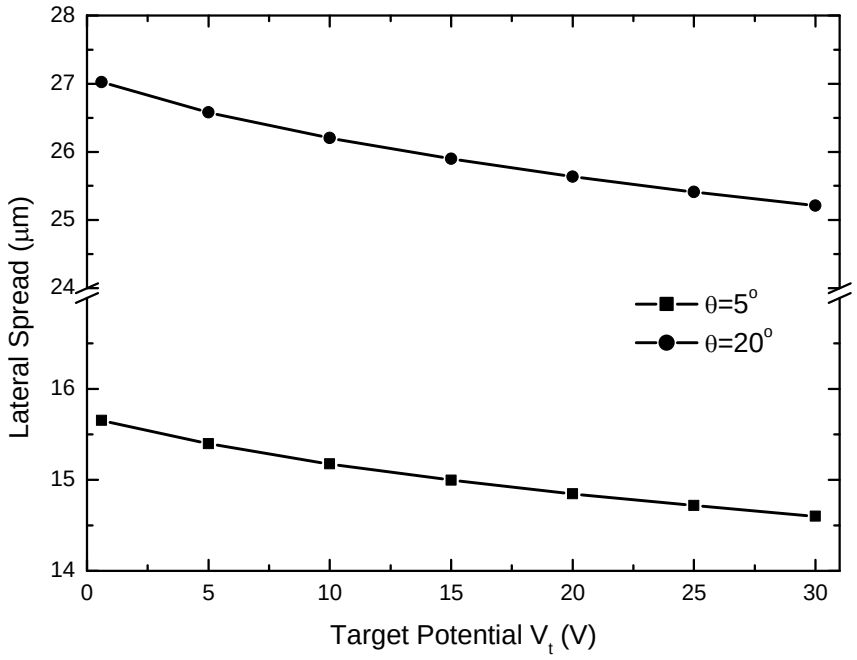

Figure 3.21: Lateral spread of electrons with electrostatic focusing as function of target potential V_t for electrons emitted at θ = 5° and 20°.

Another difference for electrostatic focusing is that the fraction of emitted electrons utilized by readout is essentially independent of V_t because all electrons emitted with θ<28° can reach the target and contribute to the readout. Whereas with the other focusing designs, the critical angle θ_c decreases with decreasing V_t, as indicated by Eq. 3.09, which means that the readout becomes less efficient as the target potential approaches ground.

c. Detector geometry and bias conditions: V_m and L_{gt}

The dependence of lateral spread on V_m is shown in Fig. 3.22 for θ = 5° and 20°. Plotted in the same graph for comparison is the lateral spread versus V_m for the mesh-electrode-only design calculated using Eq. 3.08 for θ = θ_c. It shows that lateral spread decreases with an increase in V_m. This is because the lateral spread with electrostatic focusing is the product of v_x and t_{gt}, which is similar to the mesh-electrode-only design. While v_x is reduced substantially by the focusing lens, t_{gt} can be reduced by increasing V_m or decreasing L_{gt}. However since the lateral spread is much smaller than that in mesh-electrode-only design, electrostatic focusing is much more tolerant to changes in detector geometry.

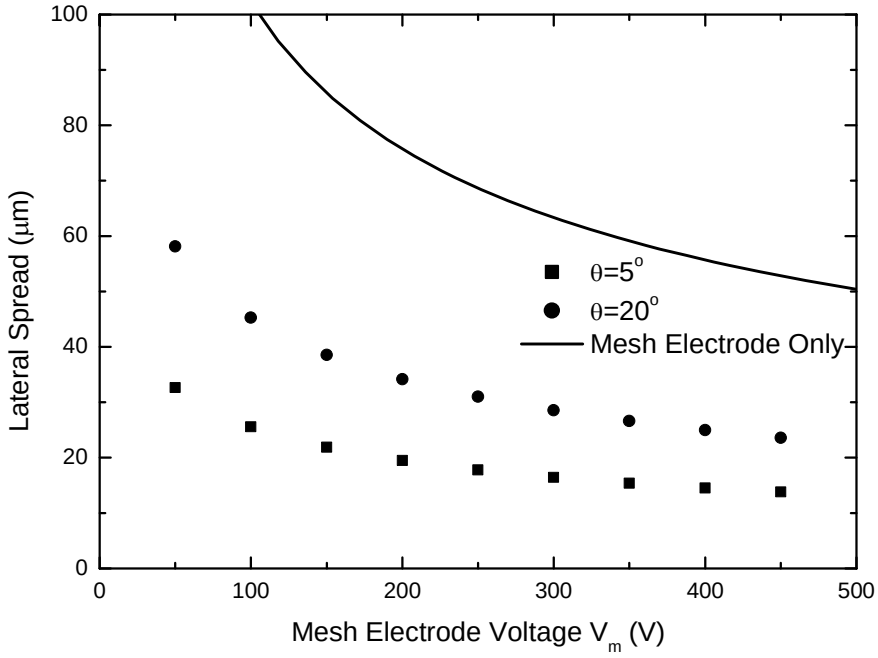

Figure 3.22: Lateral spread of electron beams with the electrostatic focusing as a function of mesh electrode potential V_m with V_t = 1.5 V. For comparison, the result for mesh-electrode-only at V_t = 0.4 V is plotted in the same graph.

3.4.3 Electron beam intensity

The intensity of the electron beam reaching the target from a single tip, $I_0(x, y)$ was obtained using Eq. 3.13. The relation between lateral spread and θ used in Eq. 3.13 was established in Eqs. 3.08 and 3.011**,** and Fig. 3.20 for the three electron-optical designs. The results of the $I_0(x,y)$ calculation are shown in Fig. 3.23. Since $I_0(x,y)$ has circular symmetry, the results are shown as a function of x only (with $y = 0$).

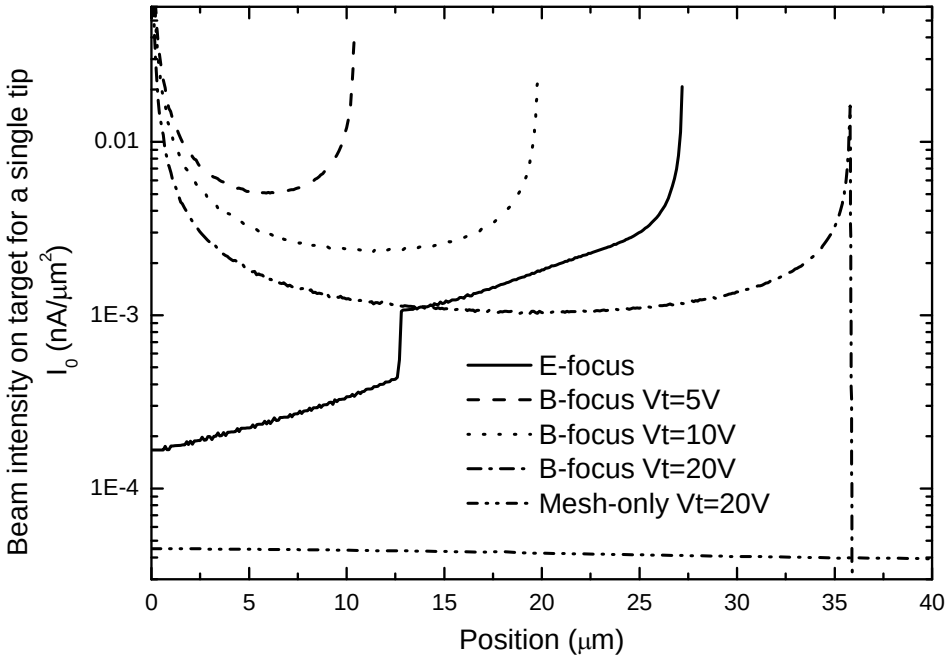

Figure 3.23: Comparison of the electron beam intensity on target for a single FE tip, $I_0(x, y)$, for three different electron-optical designs.

As shown in Fig. 3.23, $I_0(x, y)$ for the mesh-electrode-only design has the lowest intensity and widest spread, and is not suitable for mammography detectors. For magnetic focusing, $I_0(x, y)$ near the FE tip is the highest. This is because the optimal B value corresponds to complete spiral rotation of the emitted electrons regardless of the emission angle. However as discussed before, lateral spread and hence $I_0(x, y)$ depends on V_t. For electrostatic focusing, $I_0(x, y)$ is the lowest near the center, and peaks at the edge. The low

intensity at the center is because electrons emitted with small θ are not affected significantly by the focusing lens and their trajectory is similar to that in the mesh-electrode-only design. However near the edge of the emission spot on target, where lateral spread is in the range of 26 ~ 27 μm, electrons emitted with a much wider angular range accumulate due to the effect of electrostatic focusing. This can be seen from the lateral spread versus θ relation in Fig. 3.20, where the curve is essentially flat near the maximum lateral spread of 27 μm for θ between 16° and 23°. Similar behavior of higher $I_0(x, y)$ at the edge also exists in magnetic focusing because the LS-θ curves also exhibit a plateau near the maximum lateral spread, as shown in Fig. 3.17.

The results of $I_0(x, y)$ shown in Fig. 3.23 were used to calculate $I(x, y)$ for the entire pixel with 17 × 17 FE tips. The results are shown in Figs. 3.24 (A)-(C) for magnetic focusing with different target potentials, and in Fig. 3.24 (D) for electrostatic focusing. Here we omitted the result for mesh-electron-only design because it is not suitable for high resolution imaging applications such as mammography. For each intensity image of $I(x, y)$ in Fig. 3.24, the square in the center represents the emitting area of 20 μm × 20 μm, the outer square represents the desired d_{el} = 50 μm, and the boundary of 100 μm × 100 μm shows the extent of electron spreading. Figs. 3.24 (A)-(C) show that for magnetic focusing, beam spreading decreases as V_t decreases, which is consistent with the results in Figs. 3.16 and 3.23. Unlike the other two graphs, however, Fig. 3.24 (A) shows a darker ring outside the boundary of the FE tips. This is because with the wider $I_0(x, y)$ distribution for large V_t, the edge of the beam from each tip is greater than the dimension of the emission area (d_a = 20 μm) of a pixel. Therefore the shape of $I_0(x,y)$ is reflected in the integrated result for all the tips, i.e. $I(x, y)$. Similarly for electrostatic focusing, as

shown in Fig. 3.24 (D), the lower $I_0(x, y)$ in the center of each tip is reflected in the $I(x, y)$ result.

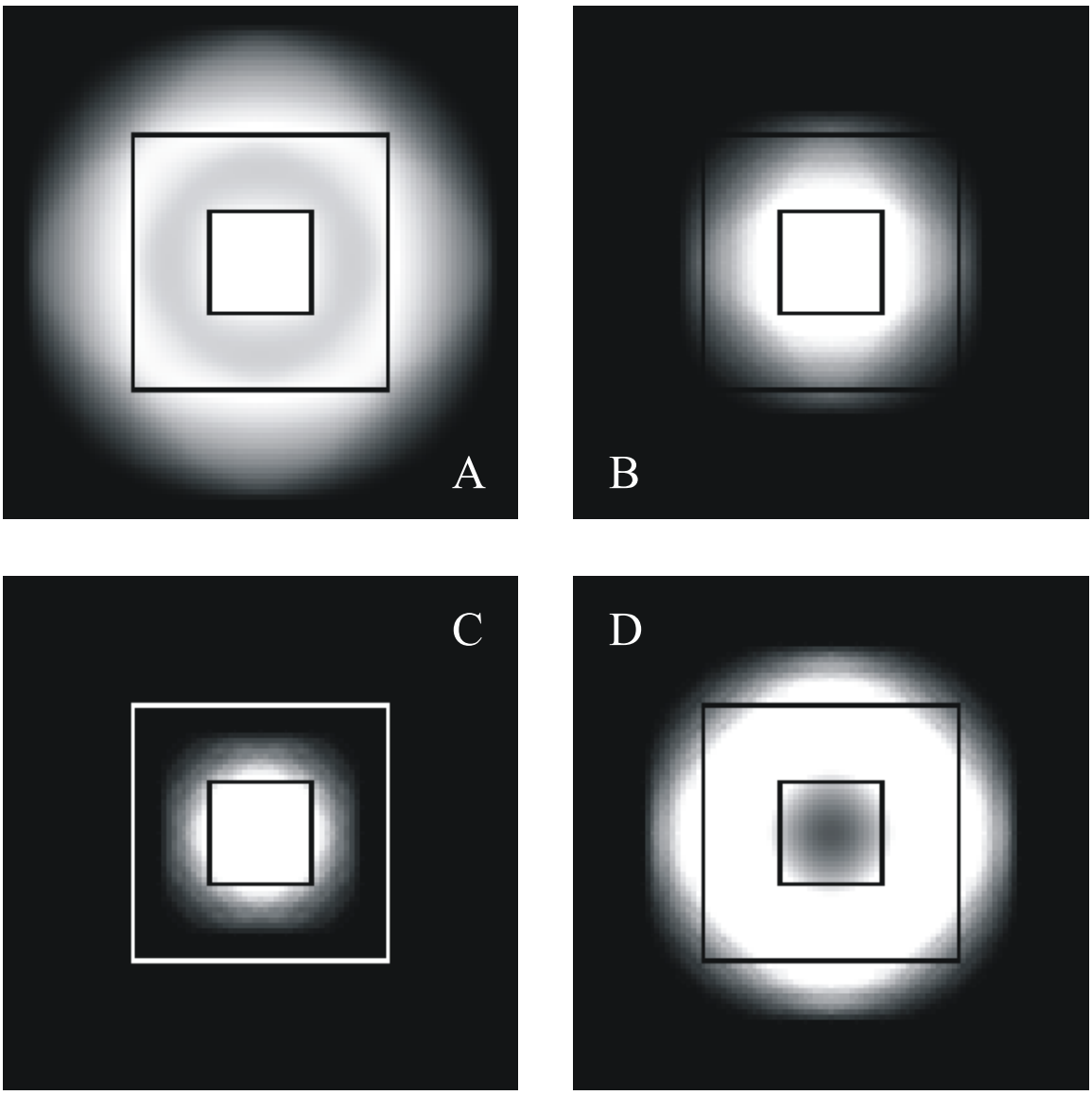

Figure 3.24: Electron beam intensity profile $I(x, y)$ for each pixel of the FEA with different focusing methods and operating conditions: A: magnetic focusing with V_t =20 V. B: magnetic focusing with V_t =10 V. C: magnetic focusing with V_t =5 V. D: electrostatic focusing. The boundary of each graph measures 100 μm × 100 μm, the outer square shows the pixel size of 50 μm × 50 μm; and the small square in the center shows the emitting area of 20 μm × 20 μm. All graphs are plotted with the same grey scale representation of beam intensity.

3.4.4 Pixel aperture function

The spatial distribution of the image charge on the HARP target read out by each FEA pixel, $Q_a(x, y)$, was obtained using Eq. 3.15. Besides the parameters listed in Table 3.01, the pixel readout time t_p and the initial target potential, V_t, also affect $Q_a(x, y)$. In breast tomosynthesis, which is an emerging 3D imaging technique using digital mammography detectors, a readout rate of 2~6 frames/s is required. This translates to t_p = 1~3 μS if we divide the ITO electrode of SAPHIRE into N_s = 128 strips. For simplicity of analysis, V_t = 20V was chosen for the calculation of $Q_a(x, y)$. As shown in Fig. 3.13, this target potential corresponds to a detector exposure of 7 mR for tomosynthesis, which is 3.5 times the mean exposure. For screening mammography, V_t = 20V corresponds to the mean detector exposure of 20 mR. The results of $Q_a(x, y)$ calculation for both magnetic and electrostatic focusing methods are shown in Fig. 3.25. Since $Q_a(x, y)$ has circular symmetry, the result is plotted as a function of x only (with y = 0). It shows that the shape of Q_a for electrostatic focusing is essentially flat across the pixel, despite the lower $I(x, y)$ intensity at the center. This is because the absolute values of $I(x, y)$ are sufficient to read out 100 % of the image charge within t_p of 3 μs. However, with the magnetic focusing design, a higher fraction of the signal is read out from the center than the periphery of the pixel. This is because the electron beam shrinks as V_t decreases during readout, as shown in Fig. 3.23. Therefore, readout using electrostatic focusing is more efficient.

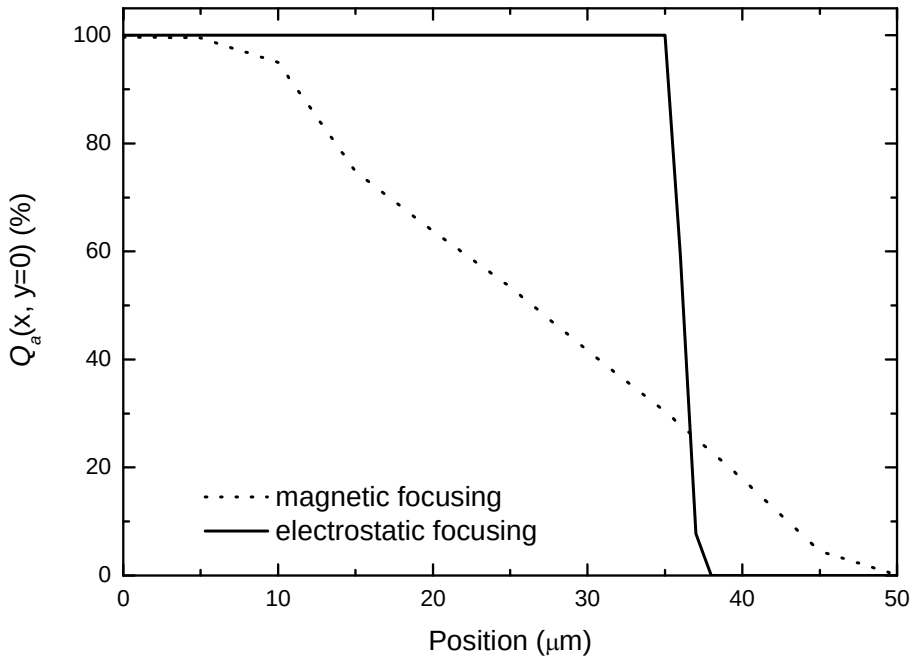

Figure 3.25: Spatial distribution of image charge on target**,** $Q_a(x, y=0)$, that is read out by each FEA pixel. The initial V_t = 20 V.

The pixel aperture functions for magnetic and electrostatic focusing, MTF_{FEA_B} and MTF_{FEA_E}, respectively, were then derived from the Fourier transform of $Q_a(x, y)$ using Eq. 3.16, and the results are shown in Fig. 3.26. At 5 cycles/mm, the values for MTF_{FEA_B} and MTF_{FEA_E} are 86% and 84%, respectively. At 10 cycles/mm, which is the Nyquist frequency for a detector with pixel size d_{el} = 50 μm, the values decrease to 53% and 46%. For comparison, the inherent MTF for SHARP, and the total detector MTF for both focusing methods are also shown in Fig. 3.26. The figure shows that the inherent resolution of SHARP is the dominant source of blur in SAPHIRE. Overall, electrostatic focusing is the better method because it provides a MTF that is independent of V_t, and allows more efficient and faster readout.

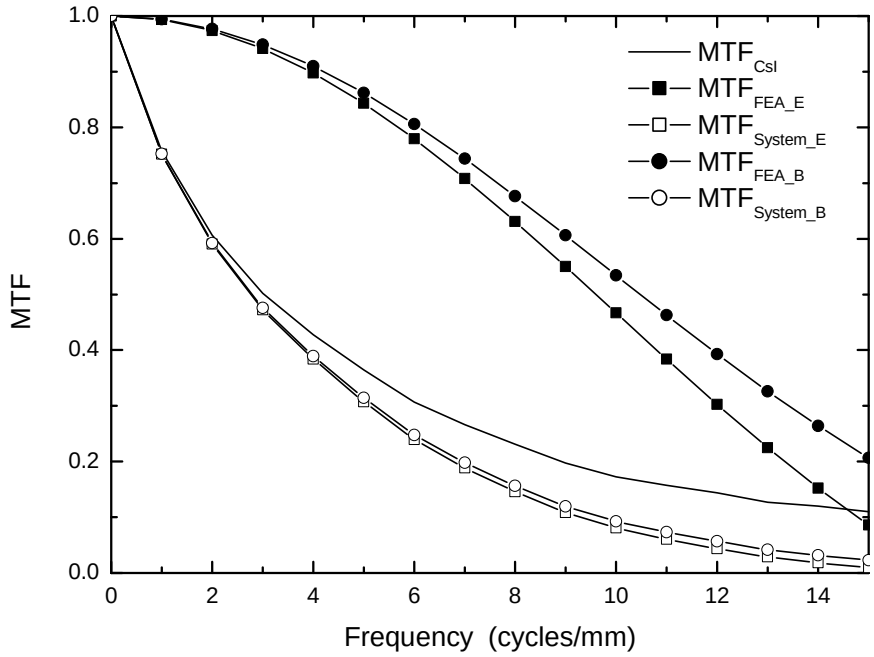

Figure 3.26: The presampling MTF calculated from $Q_a(x,y)$ in Fig. 3.25 for the FEA readout method with both magnetic focusing (denoted as _B in subscript) and electrostatic focusing (denoted as _E) methods. The presampling MTF for SHARP combination (from Fig. 3.12) and the resulting system MTF for SAPHIRE are shown in the same graph.

3.4.5 Effect of electron interaction

As mentioned in subsection 3.3.2, the lateral spread of the electron beam was calculated based on the trajectories of a single electron in the electromagnetic field with different detector geometries and bias conditions. This method assumes that the effect of interaction between electrons emitted from the same tip or neighboring tips is negligible. The main source of interaction between electrons is the space charge effect due to the electric field generated by other electrons. This effect is proportional to the electron beam intensity and the square of the electron travel time, t_{gt}, and inversely proportional to the width of the electron beam. The space charge effect for the electron beam in a Vidicon has been investigated previously [102]. It was found that for a distance of 2 cm between

the last focusing electrode and the target, the additional spread due to the space charge effect was 11 μm with a beam current of 1.6 μA and beam radius of 166 μm at the mesh electrode [102]. For FEA readout with a similar beam current (2 μA/pixel), the additional spread due to the space charge effect is expected to be < 1 μm because the travel distance, L_{gt}, is only 1 mm, which results in a travel time (~0.18 nS) that is more than an order of magnitude smaller than that in the Vidicon (~2.13 nS) [102]. Therefore this effect can be ignored in our calculation of lateral spread.

3.5 Conclusions

A new detector concept SAPHIRE is being investigated to improve the low dose x-ray imaging performance of indirect FPI. In this Chapter, we investigated the spatial resolution aspect of the imaging performance of SAPHIRE. The lateral spread of the electron beam from the FEA and the resulting pixel aperture function of the FEA readout method were investigated for three different electron-optical designs: mesh-electrode-only, magnetic focusing, and electrostatic focusing. It was found that electrostatic focusing is the only method with a pixel aperture function that is independent of the x-ray signal. It also provides the highest beam current by allowing more emitted electrons to reach the target. Therefore it is the most promising electron-optical focusing method to be incorporated in the design of SAPHIRE for high-resolution, low-dose x-ray imaging applications.

Chapter 4

Temporal Performance: Lag

In the previous chapter, we have investigated the spatial resolution of SAPHIRE. In this chapter, we investigate the temporal performance, i.e. lag, of SAPHIRE. Lag is a temporal effect which may cause smearing of subsequent images when the illumination levels change. There are multiple factors affecting lag values. Since the temporal performance of x-ray detection materials, i.e. the structured scintillator and avalanche amorphous selenium photoconductor, have been studied previously, our investigation is focused on lag due to the FEA readout method. The principle of FEA readout is similar to that of scanning electron beam readout used in camera tubes, where the dominant source of lag is the energy spread of electrons. Since the principles of emission and beam focusing methods for FEA are different from thermionic emission used in camera tubes, its electron beam energy spread and lag would be expected to be different. In the present work, the energy spread of the electrons emitted from a FEA was investigated theoretically by analyzing different contributing factors due to FEA design and operation:

the inherent energy spread of field emission, the FEA driving pulse delay, and the angular distribution of emitted electrons. The electron energy spread determines the beam acceptance characteristic curve (BACC) of the photoconductive target, i.e. the accepted beam current (I_a) as a function of target potential (V_t), from which lag can be calculated numerically. Lag calculation was performed using FEA parameters for two prototype HARP-FEA image sensors. The results were compared with experimental measurements. Excellent agreement was observed for both prototype sensors. Strategies for reducing lag in SAPHIRE were proposed and analyzed. Our results showed that for typical cardiac detector parameters, SAPHIRE with 128 parallel strips can provide real-time readout (30 frames/second) with first frame lag of ~4 %.

4.1 Introduction

The temporal performance of an x-ray imaging detector is usually characterized by lag and ghosting, which measures the residual signal and change in sensitivity from previous x-ray exposures of the detector, respectively [103]. Three major detector components of SAPHIRE may contribute to the lag and ghosting, which are: (1) the structured scintillator for x-ray detection; (2) HARP layer for optical photon detection; and (3) the FEA readout method. In a fluoroscopic system, lag is usually required to be less than 10% after the first frame [104], and the values measured from most indirect active matrix FPIs (AMFPIs) are between 2 % – 10 % depending on the x-ray exposure and detector operation [105-107]. The temporal performance of CsI (Tl) has been studied extensively for indirect AMFPI. It was found that the lag due to the afterglow of the CsI (Tl) is ~ 0.1% after 5 ms, and the typical values of ghosting are 1 % and 3 % at the

exposure levels of 1 mGy and 10 mGy, respectively [108] (1 R = 8.76 mGy). Therefore lag in existing indirect AMFPI is dominated by the charge trapping and detrapping in a-Si photodiodes. The lag and ghosting in *a*-Se photoconductors exposed to optical photons depends on the density and the depth of the charge traps. We will provide a brief analysis in section 4.2 to show that its contribution to lag and ghosting in SAPHIRE is negligible. Therefore our study is focused on the temporal properties associated with the FEA readout method, which is expected to introduce readout lag in SAPHIRE.

FEA has been widely used in display devices and shown advantages at high emission current and low operating voltages [88]. However there have been very few studies on its fundamental properties related to imaging devices. The principle of FEA readout is similar to the scanning electron beam readout method used in camera tubes (e.g. Vidicon, Saticon) except the following two differences: (1) cold source based on field emission as opposed to thermionic emission used in an electron gun of a camera tube; (2) separate electron source for each pixel that is electronically scanned versus the electro-magnetically scanned single electron beam in camera tubes. It has been established in studies of camera tubes that the main mechanism for lag due to the electron beam readout is the incomplete readout of the image charge on the target surface. This is often referred to as beam discharge lag. It depends on the energy spread of the electron beam, the capacitance of the photoconductive target, and the input signal current [48]. While the target capacitance and signal current of a HARP-FEA sensor are essentially identical to its camera tube counterpart, i.e. HARP tube, the energy spread of the electron beam is expected to be different due to the difference in emission mechanism and operating scheme.

In the present work, we have identified the following factors of the FEA design and operation that can contribute to the energy spread of electron beam: (1) inherent energy spread of emitted electrons, which results from the different probabilities of field emission for electrons at different energy levels within the atoms; (2) the delay of driving pulses for the operation of the FEA, which result in uncertainty in the potential applied to each pixel; and (3) the angular distribution of the emitted electrons. In this chapter we will provide a description of the physical mechanisms responsible for the electron beam energy spread in FEA, develop a theoretical framework to quantitatively predict energy spread with different FEA design and operating conditions, and finally these theoretical foundationd will be applied to understand experimental measurements from a small area prototype HARP-FEA sensor. Based on this framework, we will predict the beam discharge lag for SAPHIRE and propose methods to improve its temporal performance.

4.2 Theory and backgrounds

4.2.1 Photoconductive Lag in HARP

In this subsection we will present a simple analysis to show that the photoconductive lag in HARP layer is negligible. Photoconductive lag occurs when charge carriers generated in one frame are carried-over to and read out in the subsequent frame. This is caused by trapping and detrapping of photo-generated carriers when they move across the thickness of the *a*-Se layer, d_{Se}. As shown in Fig. 1.09, the holes generated by optical photons in HARP undergo avalanche multiplication when they move across the *a*-Se layer. The electrons created upon impact ionization move towards the positive ITO bias electrode. Under an electric field of E_{Se}, the charge transit time T_R is given by [109, 110]:

$$T_R = \frac{d_{Se}}{\mu_C E_{S_e}}, \tag{4.01}$$

where μ_C is the drift mobility of charge carriers in *a*-Se. At avalanche field strength (E_{Se} > 80 V/μm), the mobilities for electrons and holes are 0.06 cm^2/Vs and 1.0 cm^2/Vs, respectively [46]. The drift mobility accounts for the time a carrier spends in shallow traps. Therefore T_R provides the total transit time of a carrier from one bias electrode to the other. For HARP thickness of d_{Se} = 25μm, T_R can be calculated from Eq. 4.01 as 0.04 μS for electrons and 2.5 nS for holes. These values are much smaller than the frame time (T_F =33 mS for real time readout) therefore it is reasonable to conclude that photoconductive lag in HARP is negligible.

This is consistent with the experimental findings in optical HARP image pickup tubes which are using scanning electron beams [61, 111], where lag was dominated by the image readout (beam discharge) lag. A typical lag was 1.2% after 50 ms with a target capacitance of 400 pF and an effective beam temperature of T = 3000K.

4.2.2 Mechanisms of Energy Spread

In electron beam readout, the amount of image charge read out from each pixel is determined by the integral of the actual beam current accepted by the target (i.e. the signal current I_a) over the pixel readout time (t_p). Although the effective emission current (I_e) from each FEA pixel is typically 2 μA or higher to ensure a wide dynamic range, not all the emitted electrons can reach the target to contribute to readout. Shown in Fig. 4.01 is a schematic diagram depicting the different energy levels an emitted electron possesses when it traverses from the FE tip to the HARP target. When an electron is emitted through tunneling mechanism, its initial energy corresponds to the energy state it

occupied within the atom. As the electron travels through the gate and mesh electrodes, it gains kinetic energies corresponding to the potential differences between the electrodes. After passing the mesh electrode, the electron decelerates since the target potential (V_t), which is usually on the order of tens of volts as a result of optical exposure, is lower than the mesh potential V_m (300 ~700V). Only those electrons with sufficient kinetic energy can reach the target after deceleration, and the others will return to and be absorbed by the mesh electrode. As shown in Fig. 4.01, the electrons can reach the target only if V_t is greater than the initial energy of the electrons. As V_t approaches the initial energy of the electrons, the inherent energy spread of the emitted electrons plays an important role in how efficient the electron beam reads out image charge, i.e. lag.

The energy spread of the emitted electrons is the dominant factor for beam discharge lag. There are several contributing factors to the final energy spread: (1) inherent energy spread due to field emission process, (2) variation in base potential V_b due to the driving pulse delay and (3) angular distribution of emitted electrons after passing through the gate electrode. The mesh electrode is essentially employed in order to minimize the lateral spread of electrons [99, 101]. It does not increase or decrease the energy spread. Here we will describe the mechanism for each factor separately.

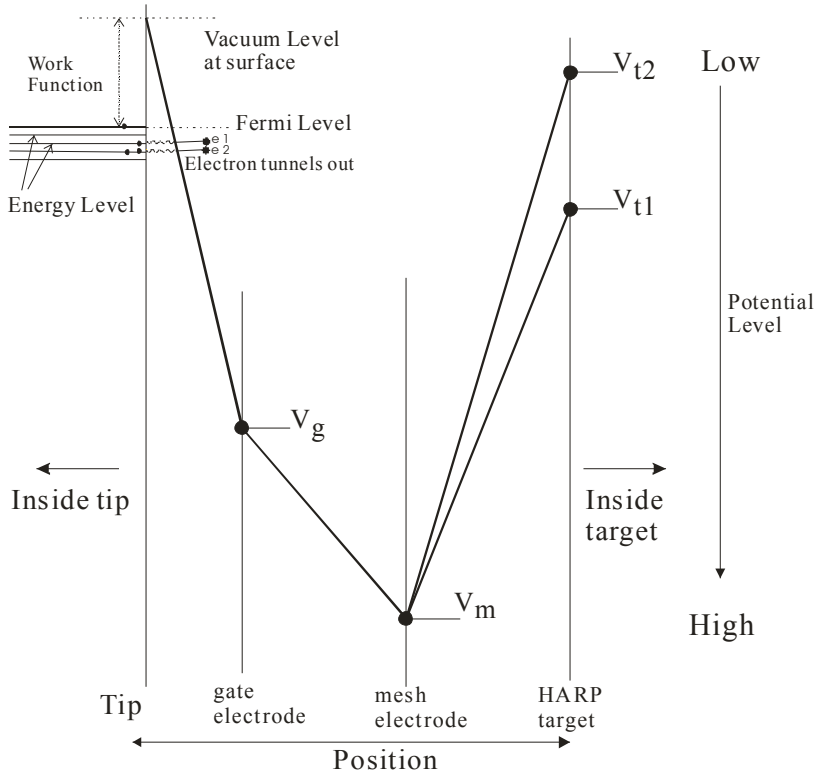

Figure 4.01: Schematic diagram showing the electron energy levels inside a HARP-FEA image sensor. The thick, black solid lines depict the change in energy of an emitted electron as it traverses from the FE tip to the HARP target. It shows that the electron can only land on the target with sufficiently high target potential (V_{t1}), otherwise (e.g. with V_{t2}) the electron does not have sufficient kinetic energy to travel to the target and will return to the mesh electrode.

1. Inherent Energy Spread

The inherent energy, E_i, refers to the energy level occupied by an electron inside the FE tip. The probability of field emission through tunneling increases with the energy level of the electron [86, 87, 90, 112]. The probability of an electron occupying a higher energy level follows the Fermi-Dirac distribution, while the tunneling probability is determined by the electric field, E_{FE}. For a given FE tip material and operation temperature (room temperature T = 300 K), the inherent energy spread of emitted electrons is only affected by E_{FE}.

2. Driving Pulse Delay

As shown in Fig. 4.01, when an emitted electron passes the gate electrode, it gains a kinetic energy $E_{bg} = q(V_g - V_b)$ due to the change in potential, where q is the elementary charge. In reality, the base potential, V_b, is not constant during the pixel readout time due to the delay of driving pulses. The FEA is operated with a passive driving scheme, where a potential difference is applied across orthogonal base and gate lines (Fig. 1.08). Each pixel is addressed by applying a forward bias between the gate and the base electrode, as shown in Fig. 4.02. At the beginning of each line, a positive bias is applied to the gate while the base of each pixel is also biased positively so that no field emission occurs. A pixel is turned on by applying 0 V to its corresponding base electrode, resulting in a forward bias between the gate and base. The driving pulse width for each pixel is typically t_p = 160 nS for an image sensor with 256 × 192 pixels and 30 frames per second readout rate [101].

In a passive driving scheme, the impedance of each gate and base electrode can be represented by a distributed resistance-capacitance (RC) network. The rectangular driving pulse for the base electrode, which constitutes the pixel clock, is delayed as it propagates through the RC load. This base potential delay results in a variation in E_{bg} and hence further energy spread. The electrons emitted with higher V_b will require higher V_t to reach the target. Furthermore, driving pulse delay also results in variation in E_{FE}, which affects the initial energy spread. The driving pulse delay also occurs on the gate line. However since the gate line bias is applied well before the pixel clocks begin, it would not cause variation in E_{bg}.

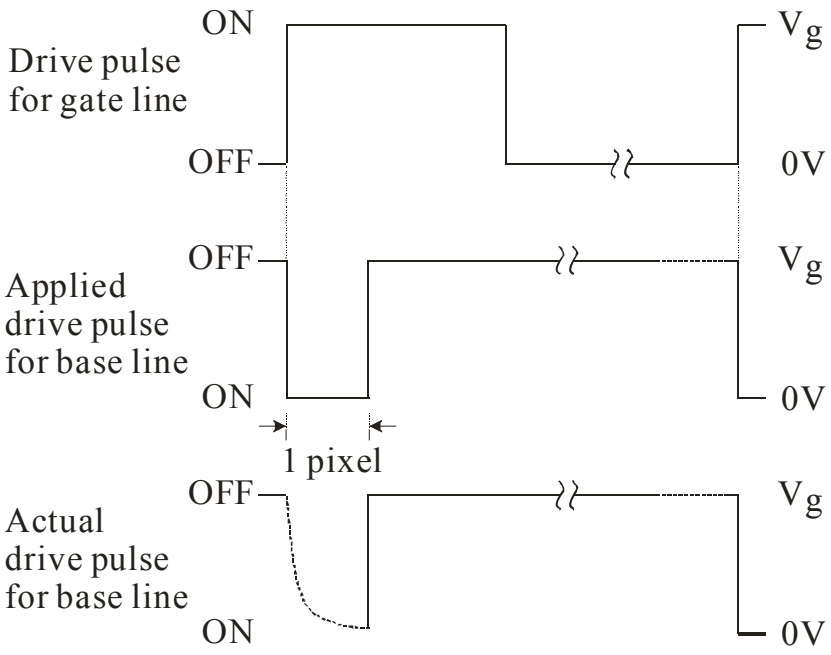

Figure 4.02: Diagrams showing the driving scheme for the FEA: the top two waveforms depict the driving pulses applied to the gate line and base line, respectively, and the bottom waveform shows conceptually the delay of the driving pulses due to the RC load of each base line.

3. Angular Distribution

The emitted electrons pass the gate electrode with some kinetic energy (E_g). However it has been shown both theoretically and experimentally that the electrons are emitted with a wide angular distribution [2]. Only the "vertical component" of kinetic energy, E_z, determines whether an electron can reach the target: $E_z = \frac{1}{2} m v_z^2$, where m is the electron mass and v_z is the vertical component of velocity. The angular distribution of emitted electrons causes further spread in E_z. The effect of angular distribution of electrons on energy spread in camera tubes has been investigated previously [48, 113]. It plays a minor role in lag because the incident angle at the last mesh electrode (θ_m) is < 5° with a

well designed electron beam focusing system [113]. In FEA, however, the angular spread of emitted electrons is up to 40° ~ 50° [2]. Although the electrons at extreme angles will not reach the target due to insufficient v_z, there could still be a substantial angular spread under typical operating conditions. The maximum θ_m of electron beam is ~15° when V_t and V_m are 20V and 300V, respectively [114]. This indicates that the angular distribution is an important source for electron energy spread and lag in an FEA image sensor.

4.2.3 Beam Acceptance Characteristic Curve (BACC)

Because of the energy spread, the amount of electrons landing on the target (i.e. I_a) varies as target potential, V_t, changes. The amount of image charge read out during t_p is determined by the integral of I_a, which decreases as V_t gradually decreases during the readout process. To determine how much charge is left on the target after each readout, i.e. beam discharge lag, it is important to investigate the dependence of I_a on V_t, i.e., $I_a(V_t)$, which is called the beam acceptance characteristic curve (BACC). BACC provides information about the energy spread (specifically, the spread in the vertical kinetic energy comportment E_z) of the electron beam. Assuming E_{z0} is the lowest E_z with which the electron can reach the target at potential, V_t, the BACC can be related to the energy spread $P_z(E_z)$ through:

$$I_a(V_t) = \int_{E_{z0}}^{+\infty} P_z(E_z) dE_z \,, \tag{4.02}$$

which is the complementary cumulative distribution function of $P_z(E_z)$.

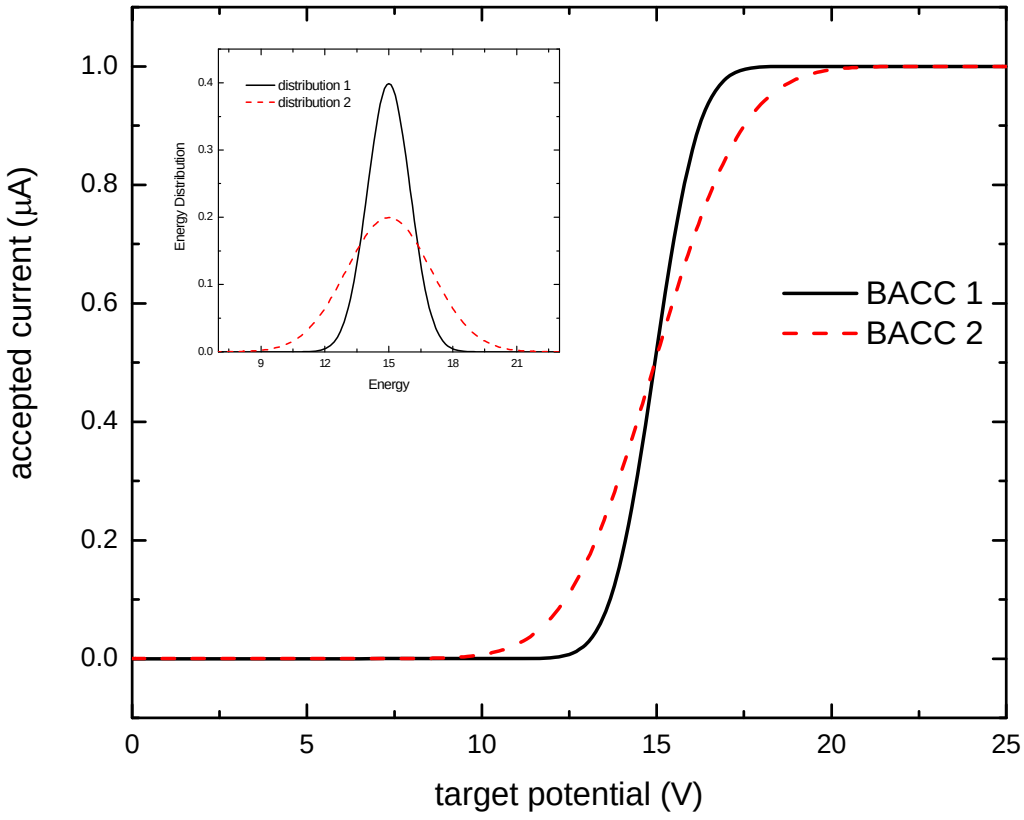

Figure 4.03: Two hypothetical beam acceptance characteristic curves (BACC) to illustrate their dependence on the energy spread of an electron beam. The corresponding energy distribution functions of the electrons are shown in the inset graph. A wider energy spread results in a shallower slope of the BACC.

Shown in Fig. 4.03 are two conceptual BACC curves with their corresponding probability distribution functions for electron energy spread. Electron beams with wider energy spread would result in a shallower rising slope on the BACC. As V_t continues to increase, I_a reaches saturation when electrons with the lowest energy are able to reach the target.

BACC has been investigated extensively for camera tubes to quantify beam discharge lag [113, 115]. When the photocurrent in the target changes abruptly from I_{p1} to I_{p2} as a result of the changes in light exposure, the target potential changes accordingly by ΔV_t.

However, the readout signal current, I_a, changes gradually following the relationship [116, 117]:

$$\Delta Q = C_t \Delta V_t = \left(I_{p2} - I_a(t) \right) \Delta t \,, \tag{4.03}$$

where C_t is the target capacitance. Eq. 4.03 describes the relationship between the amount of charge (ΔQ) read out by the electron beam and the corresponding change in the target potential (ΔV_t) during a beam dwelling time interval (Δt). To describe how to derive lag using the BACC, we assume a starting equilibrium condition of $I_a = I_{p1}$ at time $t = 0$, when the light exposure increases abruptly to I_{p2}. Image charge begins to accumulate on the free surface, i.e., $\Delta Q > 0$, which causes V_t to increase. Based on the BACC, this leads to an increase in I_a until a new equilibrium is established with $I_a(t) = I_{p2}$. With a steep slope for the BACC, a small increase in V_t would result in a substantial increase in I_a, resulting in a rapid transition into the new equilibrium, i.e. small lag. Using Eq. 4.03 and the BACC the time dependence of signal, which quantifies lag, can be predicted.

4.3 Methods

Theoretical and experimental methods were developed to understand the lag of FEA imaging sensors. Our theoretical method was to predict the energy spread of the electron beam and its associated BACC. From the BACC the lag for a FEA image sensor with a given target structure and readout speed can be predicted. Then, the predicted lag was compared with the experimental measurements from two prototype FEA image sensors with different HARP layer thickness.

4.3.1 Energy Spread and BACC

All three factors contributing to the energy spread of an electron beam were investigated theoretically: 1. inherent energy spread associated with field emission; 2. FEA driving pulse delay; and 3. angular distribution of emitted electrons. Here we will describe the method for each factor separately.

1. Inherent Energy Spread

The energy distribution of electrons from field emission has been investigated extensively [86, 87, 90]. Theoretical [89] and experimental [118, 119] studies have shown that the probability distribution of electrons emitted with inherent energy, E_i, is given by

$$P_i(E_i)dE_i = \frac{4\pi md}{h^3} e^{\left(-c+\frac{\varphi}{d}\right)} e^{\left(\frac{E_i-\varphi}{d}\right)} \left(e^{\left(\frac{E_i}{kT}\right)} + 1 \right)^{-1} dE_i , \qquad (4.04)$$

where h is the Planck's constant, k is the Boltzmann constant, φ is the work function of the emitter material, and c and d are two functions related to the applied electric field, E_{FE} [112].

As shown in Fig. 4.01, in order for an electron to reach the target with potential, V_t, it needs to have an initial energy $E_i \geq q(V_b - V_t)$. Therefore the signal current, $I_a(V_t)$, can be obtained by integrating the emitted electrons in this energy range:

$$I_a(V_t) = qA_e \int_{q(V_b-V_t)}^{\infty} P_i(E_i)dE_i , \qquad (4.05)$$

where A_e is the effective emission area. Eq. 4.05 provides the BACC associated with the inherent energy spread only.

2. Driving Pulse Delay

The driving pulse delay is mainly associated with the base electrode line, which contains the pixel clock. The time response of the driving pulse was simplified using a single exponential decay function:

$$V_b(t) = V_g \exp(-t/\tau) \tag{4.06}$$

where τ is the RC time constant for the total resistive and capacitive load for each line. When an emitted electron passes through the gate electrode, the probability for it to accumulate a kinetic energy of $E_{bg} = q(V_g - V_b)$ is proportional to the amount of emitted electrons, $I_e(V_b)\times \mathrm{d}t$:

$$P_b(E_{bg})dE_{bg} = N_b I_e(V_b)dt = N_b I_e(V_b)\frac{dt}{dE_{bg}}dE_{bg}, \tag{4.07}$$

where N_b is a normalization factor to ensure a total probability of unity. The emission current density, I_e, under different operation conditions can be obtained using the method in ref. [90]. Eq. 4.07 is solved numerically by dividing t_p into infinitesimal small dt and calculating the amount of emitted electrons during dt. In order for an emitted electron to reach the target, its initial kinetic energy, E_{bg}, must be sufficient to overcome the potential difference between the gate electrode and the target, i.e., $E_{bg} \geq q(V_g - V_t)$. Hence the total beam current reaching the target with potential, V_t, can be obtained by:

$$I_a(V_t) = \int_{q(V_g - V_t)}^{\infty} P_b(E_{bg})dE_{bg}. \tag{4.08}$$

Eq. 4.08 can be used to derive a BACC that includes only the effect of variation in V_b due to driving pulse delay.

3. Angular Distribution

For the present investigation, we used the angular distribution of electrons emitted from Spindt-type FEA for the calculation of energy spread. This type of FEA was incorporated in the HARP-FEA image sensors used in the experimental measurement of lag. It was also used as an example in our previous investigation of spatial resolution of SAPHIRE [114]. Here, the same angular distribution adapted from ref. [2] was used in our calculation, as shown in Fig. 3.11 for the electron beam intensity as a function of emission angle, θ, i.e., $I(\theta)$. The angular distributions are slightly different for different sizes of the Spindt-type FE tips, however, this difference is very trivial and is ignored here.

For electrons with a kinetic energy of E_g at the gate electrode [99], their vertical components E_z can be calculated using $E_z = E_g \cos^2\theta$. Its probability distribution can be derived (in Appendix D) as:

$$P_z(E_z) = N_0 \frac{I(\theta)}{\cos\theta}, \tag{4.09}$$

where N_0 is a normalization factor. If E_z is greater than the potential difference between the target and the gate electrode (V_g), i.e., $E_z > q(V_g - V_t)$, the electron can land on the target and contribute to I_a:

$$I_a(V_t) = \int_{q(V_g - V_t)}^{\infty} P_z(E_z) dE_z \ . \tag{4.10}$$

Eq. 4.10 defines the BACC that only includes the energy spread due to the angular distribution of emitted electrons.

4. Total energy spread

The energy spread of electrons due to the first two factors, which are given in Eqs.

4.04 and 4.07, were first combined to provide the total energy E_g of an electron at the gate electrode:

$$E_g = E_i + E_{gb}\,. \tag{4.11}$$

The joint probability distribution for E_g is given by:

$$P_g(E_g) = \sum_{E_i} P_i(E_i) \bullet P_b(E_g - E_i)\,. \tag{4.12}$$

Eq. 4.12 was then substituted with Eq. 4.09 to obtain the total energy (z-component) spread as $P_o(E_z)$:

$$P_o(E_z) = \sum_{E_g} P_g(E_g) \bullet \frac{I(\theta)}{\cos(\theta)}, \tag{4.13}$$

To obtain the BACC due to the total energy spread, Eq. 4.13 was substituted into Eq. 4.10:

$$I_a(V_t) = \int_{q(V_g - V_t)}^{\infty} P_0(E_z) dE_z\,. \tag{4.14}$$

4.3.2 Prediction of Lag

When the photocurrent in the HARP target changes from I_{p1} to I_{p2} due to exposure change at time t =0, the beam discharge lag, $L(t)$, can be expressed as

$$L(t) = \frac{I_a(t) - I_{p2}}{I_{p1} - I_{p2}} \times 100\%\,. \tag{4.15}$$

When $I_{p1} > I_{p2}$, it is called turn-off lag or white-to-black lag; otherwise, it is called turn-on lag. The turn-on lag in electron beam readout is usually smaller than the turn-off lag due to the same shape of the BACC [48], We will thus focus our study on the turn-off lag.

To calculate $L(t)$, we need to obtain the time dependent signal current $I_a(t)$. As

described in subsection 4.2.3, the BACC and Eq. 4.03 can be used to solve for $I_a(t)$. Since we cannot obtain an analytical expression for the BACC of field emission, as for thermionic emission [116], we solve the equations numerically by dividing t into small time intervals Δt ($\sim t_p /10^4$ in our calculation) and updating V_t and I_a in real time.

4.3.3 Experimental Measurement of Lag

The experimental measurement of lag was performed on two small area HARP-FEA prototype optical image sensors with different HARP layer thicknesses [99]. The geometry and structure of the prototype sensor were identical to those used in our previous investigation of the spatial resolution of SAPHIRE [114]. The FEA contains 256 × 192 pixels, with pixel size of d_{el} = 50 μm. The emitting area of d_a = 20 μm, which contains 17 × 17 Spindt-type FE tips, is located in the center of each pixel. The FEA was turned on pixel by pixel using a passive driving scheme with t_p =160 nS and V_g = 48 V. The HARP layer thicknesseses in the two prototype sensors were d_{Se} = 4 μm and 25 μm, with corresponding high voltage bias (applied to ITO electrode) of 440 V and 2580 V, respectively.

4.4 Results and discussion

4.4.1 Beam discharge Lag

1. Inherent Energy Spread

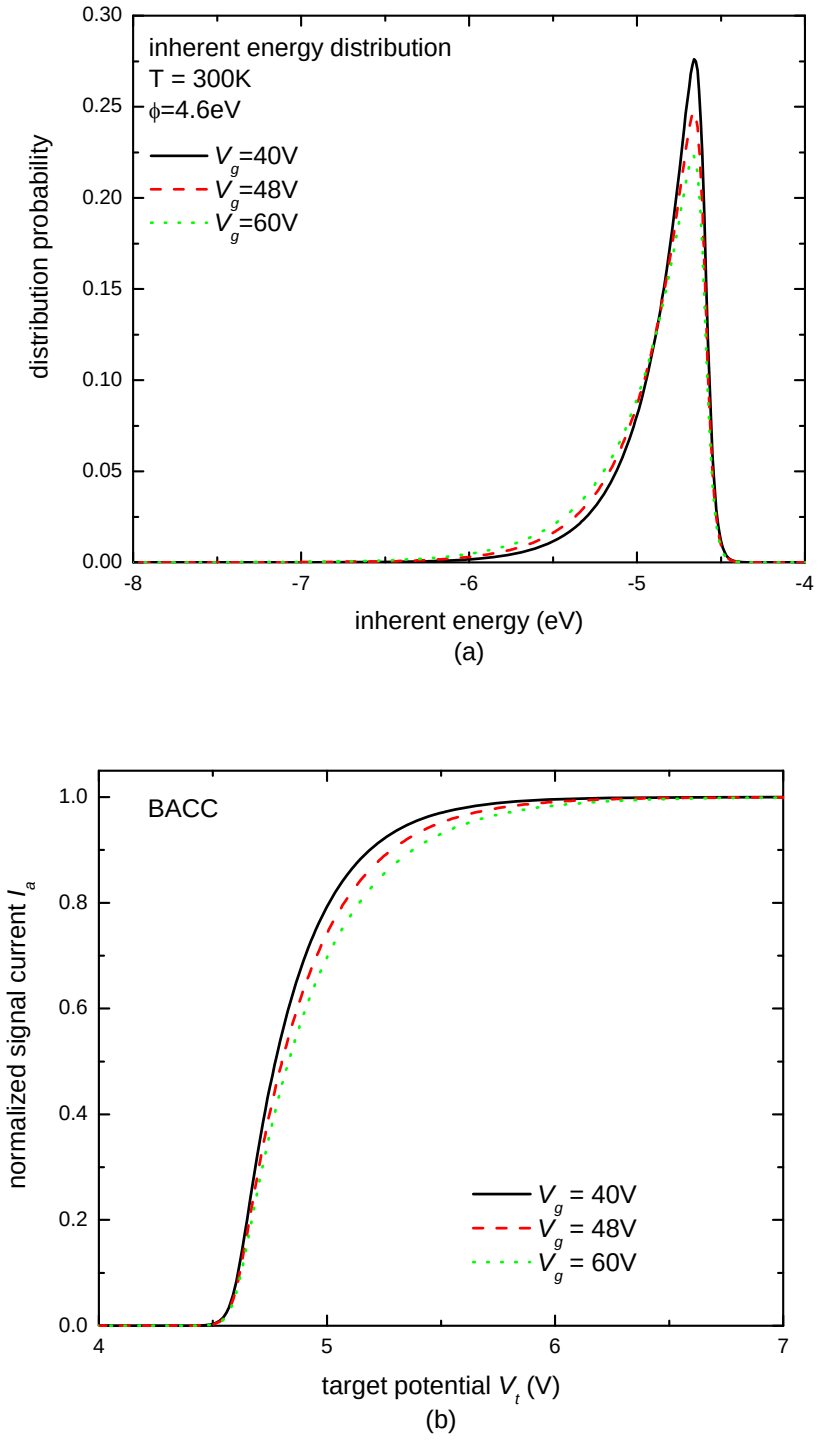

Figure 4.04: (a) The inherent energy (E_i) distribution of emitted electrons at different V_g for Mo emitters at room temperature. (b) The BACCs associated with the inherent energy spread in Fig. 4.04 (a) at different V_g.

The inherent energy distribution for electrons through field emission is given by Eq. 4.04. For Spindt-type FEA with Mo emitters which is operated at room temperature, φ = 4.6 eV and T = 300 K. Typically E_{FE} needs to be > 10^9 V/m to maintain a reasonable field emission current [88]. It was estimated that E_{FE} of ~ 7×10^9 V/m was maintained with V_g = 48 V for Spindt-type FEA in our prototype sensors. Fig. 4.04 (a) plots the inherent energy distributions at V_g = 48 V in comparison with V_g = 40 V and 60V. Their corresponding BACC were calculated using Eq. 4.05. Since both emission current and energy spread change as a function of V_g, the calculated BACC curves were normalized, as shown in Fig. 4.04, to facilitate the comparison of energy spread, which is reflected by the slope of the curves.

Fig. 4.04 (a) shows that the maximum energy E_i of emitted electrons is ~ -4.6 eV for all three V_g. This is because the energy is defined relative to the vacuum level and the work function for Mo is Φ = 4.6 eV. At T =300K, the energy for most electrons are below the Fermi level. Fig. 4.04 (a) also shows that the standard deviations, σ_i, of the inherent energy spread increases as E_{FE} increases. They are 0.26, 0.34 and 0.42 eV, respectively, for V_g values of 40, 48 and 60 V. This is because at higher V_g (i.e., higher E_{FE}), more electrons with lower E_i can emit through tunneling. The inherent energy spread is smaller than that in thermionic emission (used in electron tubes), which is typically 0.6 ~ 0.7 eV in theory [89]. Fig. 4.04 (b) shows that a smaller V_g leads to a sharper rising slope, however with smaller emission current.

2. Driving Pulse Delay

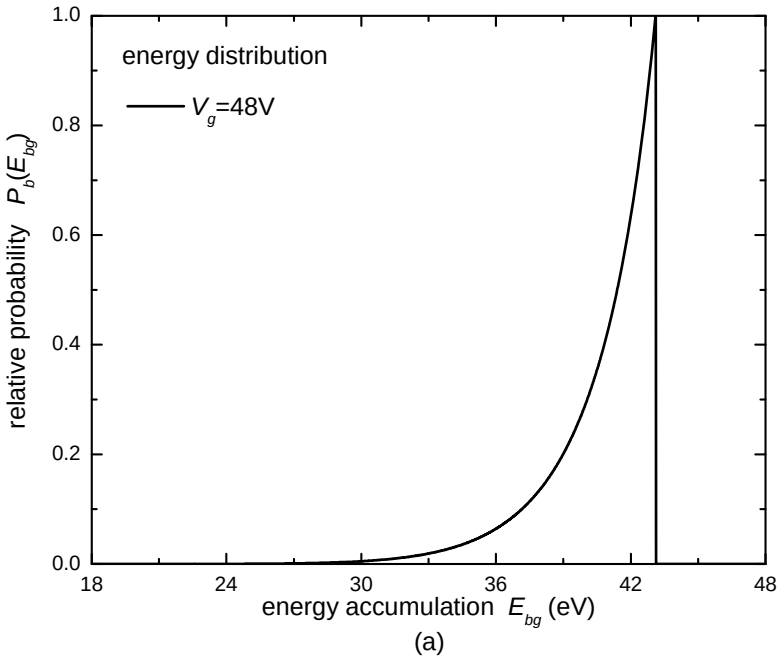

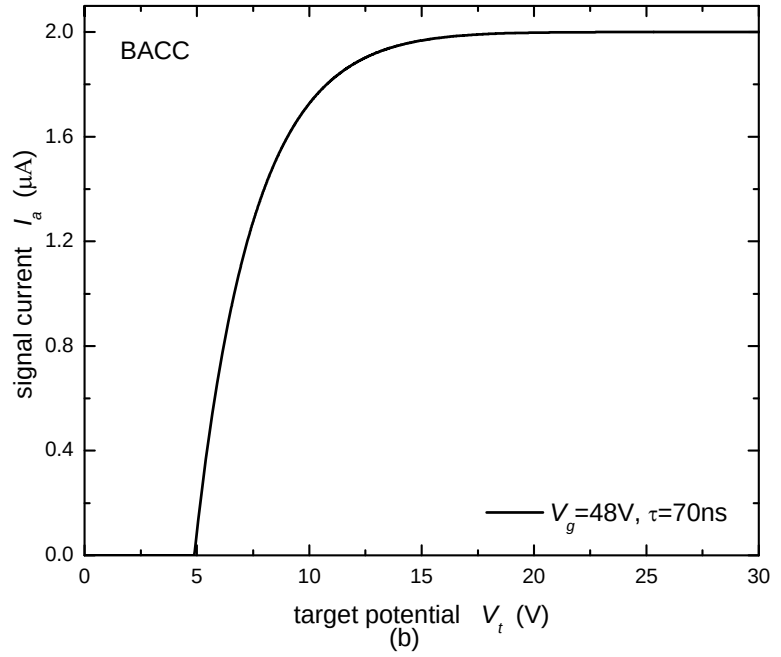

Figure 4.05: (a) The distribution of energy accumulation (E_{bg}) of electrons due to the delay of driving pulses as they pass through the gate with V_g = 48V and delay time constant τ =70 nS. (b) The BACC associated with the energy spread due to driving pulse delay shown in Fig. 4.05 (a).

The variation in base potential, V_b, due to driving pulse delay results in a variation in energy gain as the emitted electrons pass the gate electrode. The value for V_b was calculated using Eq. 4.06 with τ = 70 nS. The distribution of energy gain, E_{bg}, was calculated using Eq. 4.07 and the results are shown in Fig. 4.05 (a) for a gate bias potential of V_g = 48V. The corresponding BACC was obtained using Eq. 4.08 and shown in Fig. 4.05 (b).

Fig. 4.05 (a) shows that more electrons are emitted with higher E_{bg} (as V_b approaches 0 V). This is because a lower V_b results in higher E_{FE} and emission current. The standard deviation of E_{bg} distribution, σ_b, was obtained using Eq. 4.07 as 2.61eV, which is substantially larger than σ_i. Listed in Table 4.01 are the σ_b values calculated for different FEA operating conditions. Since V_g is usually selected to ensure sufficient emission current (e.g. 2 μA per pixel) for a wide dynamic range, the preferred method for decreasing σ_b is to increase the ratio of t_p / τ . Fig. 4.05 (b) shows that with driving pulse delay, the slope of the BACC becomes shallower, and the intercept with the horizontal axis also increases by ~ 5 V.

Table 4.01: Standard deviation of energy spread σ_b due to driving pulse delay under different conditions:

(a) σ_b as function of V_g at τ = 70 nS

V_g (V)	40	48	60
σ_b (eV)	1.96	2.61	3.69

(b) σ_b as function of τ at V_g = 48V

τ (nS)	60	70	80
σ_b (eV)	2.54	2.61	2.65

3. Angular Distribution

The angular distribution of electron beam intensity in Fig. 3.11 was used to calculate the distribution of E_z using Eq. 4.09, and the results are shown in Fig. 4.06 (a) for three values of E_g. Their corresponding BACCs, calculated using Eq. 4.10, are shown in Fig. 4.06 (b). To facilitate comparison all curves were normalized.

Fig. 4.06 (a) shows that the maximum E_z corresponds to its associated E_g value. The shape of E_z is consistent with that of the angular distribution curve in Fig. 3.11. The standard deviation of E_z spread, σ_z, increases as E_g increases, as shown in Table 4.02. This is because E_z is proportional to E_g through $E_z = E_g \cos^2 \theta$. Fig. 4.06 (b) shows that a larger energy spread (e.g. E_g = 60 eV) leads to a shallower slope for the BACC curve.

Table 4.02: Standard deviation of energy spread σ_z due to angular distribution under different operating conditions:

E_g (eV)	40	48	60
σ_z (eV)	5.03	6.04	7.55

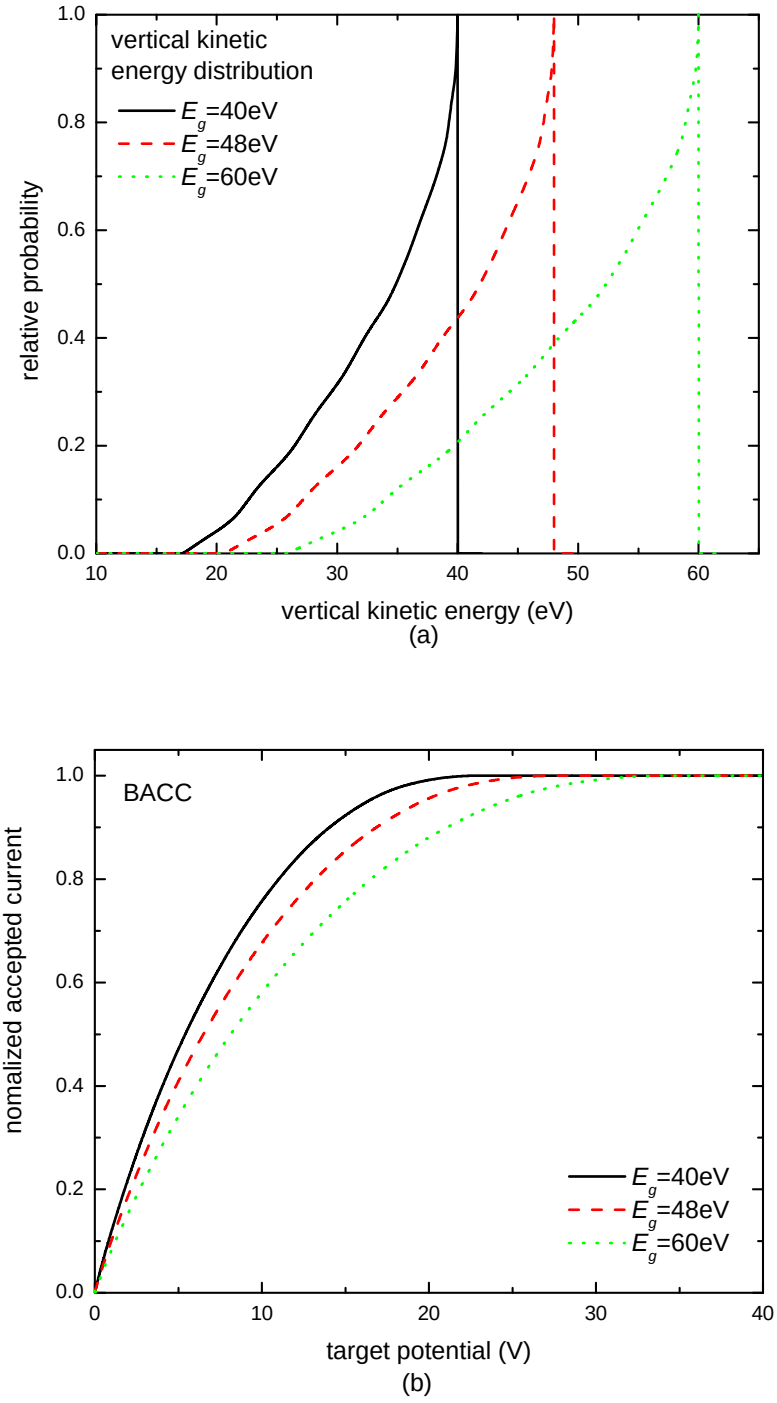

Figure 4.06: (a) The distribution of the vertical component of kinetic energy (E_z) due to the angular distribution of emitted electrons. The total kinetic energy accumulated by the electrons as they pass through the gate, E_g, was assumed to be constant. (b) The normalized BACCs associated with the E_z distributions in Fig. 4.06 (a).

4. Total Energy Spread

To combine all factors, the distribution of E_g, ($P_g(E_g)$) due to the first two factors, was calculated using Eq. 4.12 as the first step, then the total E_z distribution $P_o(E_z)$ was obtained using Eq. 4.13. The results for $P_g(E_g)$ and $P_o(E_z)$ are shown in Fig. 4.07 (a). The FEA operating parameters used in the calculation were chosen based on the prototype FEA sensors, i.e., V_g = 48 V.

Fig. 4.07 (a) shows that the first two factors result in a combined energy spread of σ_g = 2.65 eV for E_g, and a reduction of the maximum E_g to ~ 38 eV, as shown in Fig. 4.07 (a). After inclusion of the angular distribution, the standard deviation for the total energy spread in E_z is σ_z = 5.51 eV. The corresponding BACC is given in Fig. 4.07 (b), which shows that the BACC has an intercept of ~10 V with the horizontal axis (i.e. V_t) and the rise of I_a occurs over a V_t span of ~20 V. These results are consistent with the total energy spread in E_z shown in Fig. 4.07 (a).

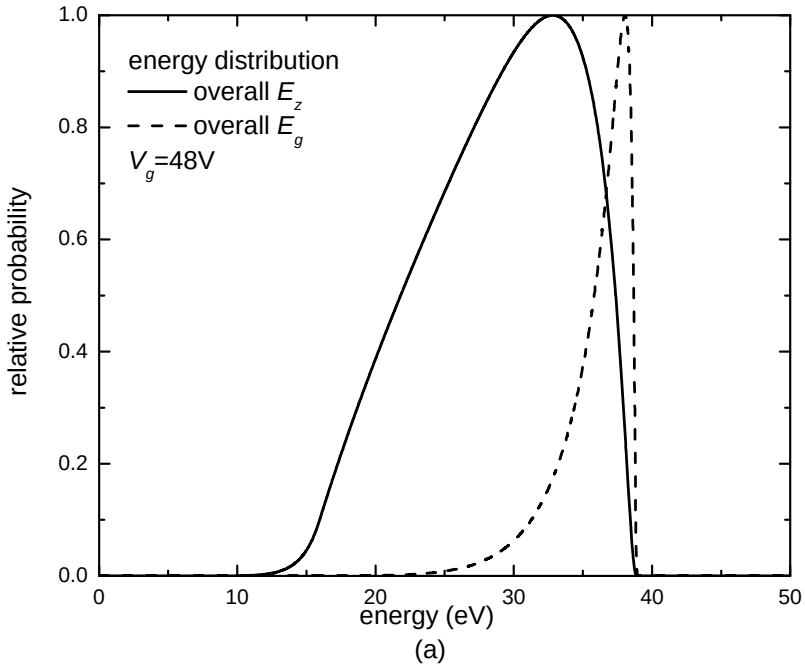

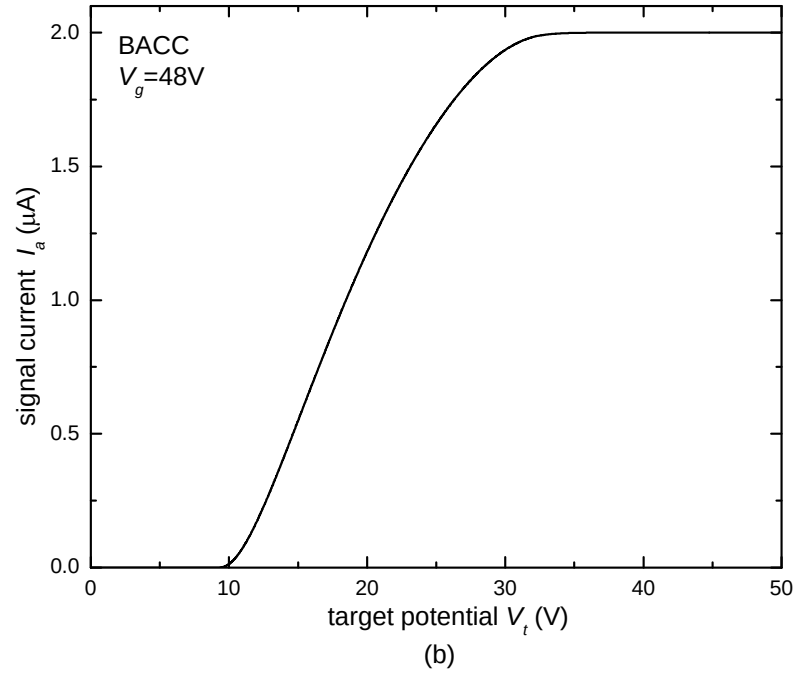

Figure 4.07: (a) The energy spread in E_g (dashed line) due to the first two factors, and the total energy spread in E_z (solid line) due to all three factors at V_g = 48V. (b) The BACC corresponding to the total energy spread in E_z due to all three factors at V_g = 48V.

4.4.2 Prediction of Lag

The BACC in Fig. 4.07 (b) was used to predict the beam discharge lag using Eqs. 4.03 and 4.15. The operational parameters were chosen based on the prototype HARP-FEA sensors, where the emission current was I_e = 2 μA/pixel at V_g = 48V. The initial photocurrent was I_{p1} = 200 nA, i.e. the maximum signal current experienced by the prototype sensor. The thickness of the HARP target for the two prototype sensors was d_{Se} = 4 μm and 25 μm. The final signal current, I_{p2}, was selected to be the dark current (i.e. no optical exposure), which is < 1 nA in avalanche mode. The calculated lag curves for both prototype sensors are shown in Fig. 4.08. Lag was normalized to the signal prior to the exposure change, as defined in Eq. 4.05. The first frame lag (at 33 ms or second field) is 60.3 % and 9.2 % for d_{Se} = 4 μm and d_{Se} = 25 μm, respectively.

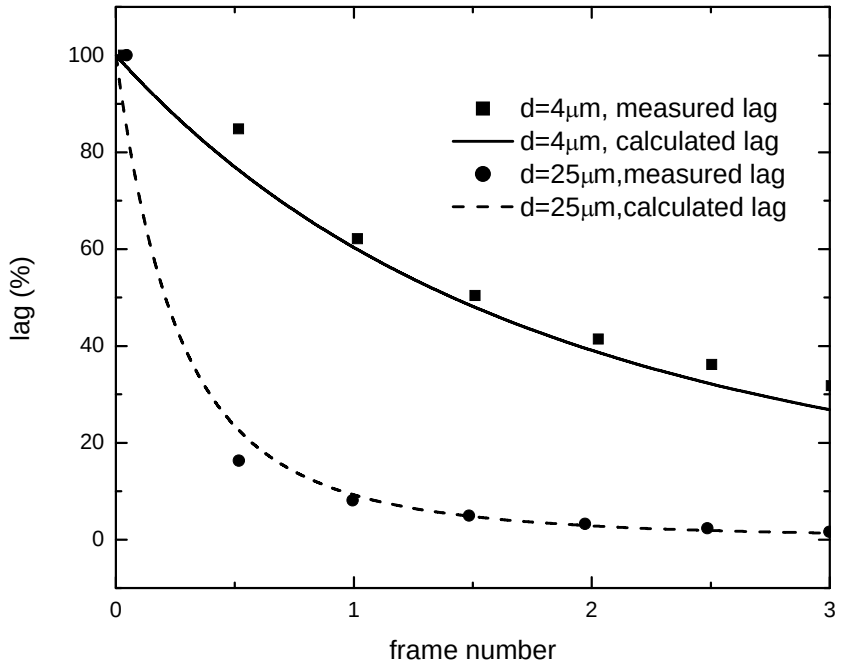

Figure 4.08: Comparison between calculated and measured lag as a function of frame number (at 30 frames/second) for two prototype HARP-FEA image sensors. The HARP layer thickness was d_{Se} = 4μm and 25μm.

4.4.3 Measurement of Lag

The turn-off lag was measured for both prototype HARP-FEA optical sensors using the method described in subsection 4.3.3, and the results are plotted in Fig. 4.08 together with the theoretical calculations for both HAPR layer thicknesses. The measured first frame lag was 62.1% and 9.1% for d_{Se} = 4 μm and d_{Se} = 25 μm, respectively. The lower lag for thicker HARP target is due to the smaller C_t under the same FEA operating conditions. The measurement and theoretical calculations are in excellent agreement.

4.4.4 Strategies for lag reduction with FEA readout method

Our results showed that the measured lag agrees well with the theoretical calculation, which validates our understanding of the mechanisms. However the amplitude of lag is much larger than that for electron tube devices. Methods for reducing lag are needed before the FEA readout method can be used in practical imaging applications. Here we will discuss several strategies for reducing lag based on our understanding of its mechanisms.

1. Reducing energy spread of electrons

To improve the spatial resolution of SAPHIRE, an electrostatic beam focusing method is being investigated [114]. The additional focusing electrode, which is built directly above each single FE tip using photolithography, will redirect the electrons emitted at large angles to the vertical direction. Therefore it has the potential to reduce the angular spread of emitted electrons, which is the dominant source of energy spread and lag. Once a FEA with focusing electrode is manufactured, the angular distribution of

emitted electrons will be investigated and its corresponding change in E_z calculated to estimate the improvement in lag.

2. Alternative driving schemes

One of the advantages of the FEA over the scanning electron beam is its array structure, which makes it possible to turn on multiple FEA pixels at the same time. A lag clearance procedure can be implemented between the readout of subsequent frames. At the end of each frame, all the FEA pixels will be turned on simultaneously for a lag clearance period t_c that is equal to the time required to reset the target potential V_t. For example to reduce lag to 2 % in a 25 μm thick HARP target, $t_c = 3\ t_p$ is required according to Fig. 4.08. This method is equivalent to reading out the pixel for four consecutive frames although only the signal from the first frame is recorded. For image sensors with a large number of pixels, e.g. 1000 × 1000, the total current needs to be drawn from the FEA driving circuit may be prohibitive. In this case, the clearance procedure can be implemented between subsequent rows or a number of rows.

3. Lag reduction in SAPHIRE

With the lag clearance procedure described above, the lag of a small-area (2.54cm diameter) HARP-FEA image sensor can be reduced to a negligible level. However, the size of SAPHIRE for x-ray imaging is much larger and major changes are needed to allow real time readout without lag. A 25 cm × 20 cm cardiac detector with 200 μm pixel size has 1250 × 1000 pixels and requires $t_p < 30$ ns with pixel-by-pixel readout in 30 frames/second. Lag with such short t_p would be unacceptable, hence a parallel beam

readout method has been proposed [120]. The ITO electrode of SAPHIRE is divided into N_s parallel strips, each connected to an individual charge amplifier, as shown in Figs. 3.06 and 3.07. In parallel beam readout, N_s pixels are turned on simultaneously thus increasing t_p by a factor of N_s compared to the pixel-by-pixel approach. This in turn will minimize driving pulse delay for large area FEA, which also helps reduce lag.

To quantitatively illustrate the effects of pixel size, detector size and N_s on the lag of SAPHIRE, we provide an example lag calculation for a hypothetical SAPHIRE with d_{Se} = 25 μm, d_{el} = 200 μm and a detector size of 25 cm × 20cm. The signal current chosen for lag calculation, I_{p1} = 2 μA, corresponds to the mean detector exposure of 1 μR/frame in fluoroscopy. For real-time applications with higher exposures (e.g. cine and angiography), the range of signal current is expected to be similar to that in fluoroscopy since the avalanche gain of HARP will be reduced [52, 114]. The operating condition for Spindt-type FEA is assumed to be V_g = 48 V. Compared to the optical HARP-FEA sensor with 50 μm pixel size discussed earlier, the pixel size of a SAPHIRE is 16 times larger, which increases both I_e and C_t by a factor of 16. According to Eq. 4.03, the lag for SAPHIRE should be independent of pixel size. The calculated lags with different N_s values are shown in Fig. 4.09. With N_s = 1, t_p for SAPHIRE is ~ 26 nS with pixel-by-pixel readout. Even if we ignore driving pulse delay with such a short t_p, the first frame lag is 42 %, which is unacceptable. With N_s = 16 and parallel readout, t_p increases to 420 nS, and the first frame lag is reduced to 8 %. With N_s = 128 and further increase in t_p to 3.4 μS, the first frame lag is 4.3%, which is within the range of lag values measured in AMFPIs [105-107]. Further reduction in lag could be realized by incorporating the charge clearance procedure described in subsection 4.4.4.2. It is important to note that the lag

calculation results in Fig. 4.09 only included the effects of the inherent energy spread and angular distribution, which results in underestimation of lag for $N_s < 40$ due to driving pulse delay. However driving pulse delay is negligible in the preferred detector configuration of $N_s = 128$.

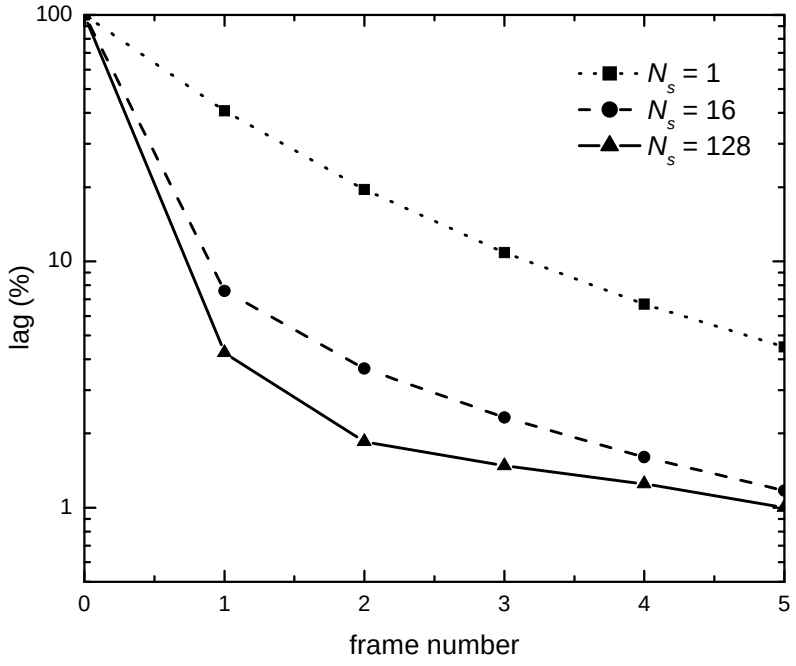

Figure 4.09: The prediction of lag for SAPHIRE with and without parallel beam readout. The detector parameters used were: d_{Se} = 25 μm, I_{p1} = 2 μA, I_{p2} = 0 and V_g = 48V.

4.5 Conclusions

In this chapter, we investigated the temporal performance of the new proposed detector concept, SAPHIRE. The beam discharge lag is the dominant lag source, which is due to the energy spread among electron beams. The mechanism of field emission electron beam on FEA is investigated by including three main factors: the inherent energy spread, the base potential delay effect and the angular distribution effect. The dominant source of the energy spread is the angular distribution. Our prediction agrees very well with

experiments on a small area optical HARP-FEA sensor. Due to the large size of SAPHIRE, several methods are designed based on the mechanism of field emission to improve its temporal performance. Parallel beam readout can increase the pixel turn-on time and remove the base potential delay effect, as well as help to reduce beam discharge lag. With proper design, the lag of SAPHIRE is expected to be less than 5% after the first frame. It can be optimized by a flushing method to remove the residual signals. Electrostatic focusing method has the potential reduce the angular distribution effect greatly.

Chapter 5

Experimental Investigation of a Prototype Image Sensor

Previously we investigated the signal detection of Scintillator/HARP and theoretical resolution of FEA separately. In this chapter, the imaging characteristics of FEA readout method, including spatial resolution and noise characteristics, were investigated experimentally by using a prototype 15-μm-thick optical HARP-FEA image sensor with magnetic focusing. The FEA pixel size is set at 20 μm for better resolution. The FEA is also used to read out charge information generated by HARP to investigate its sensitivity. The avalanche gain of HARP depends on both *a*-Se thickness and applied electric field, E_{Se}. As expected, at E_{Se} > 80 V/μm, the avalanche gain can enhance the signal at low dose (e.g. fluoroscopy), allowing the detector to be x-ray quantum noise limited down to a single x-ray photon. At high exposure (e.g. radiography), the avalanche gain can be turned off by decreasing E_{Se} to < 80 V/μm. The potential x-ray imaging performance of SAPHIRE, especially the advantage of programmable gain to ensure wide dynamic range and x-ray quantum noise limited performance at the lowest exposure in fluoroscopy, was investigated in experiments

5.1 Introduction

Two of advantages of the proposed SAPHIRE detectors are: (1) programmable avalanche gain g_{av}, ensures a wide dynamic range for the detector; and (2) FEA readout can provide smaller pixel sizes than possible with TFTs. In previous chapters, we have developed a cascaded linear system model to predict the fundamental x-ray image quality of indirect FPI with avalanche gain [52, 53] and demonstrated the advantages of programmable avalanche gain, g_{av}, to ensure a wide dynamic range. We also theoretically investigated the spatial resolution of SAPHIRE with three different electron-optical designs [114]: (1) a mesh electrode inserted half way between the HARP and the FEA, as shown in Fig. 1.09; (2) an external magnetic focusing and (3) an integrated electrostatic focusing electrode in addition to the mesh electrode. It was found that with magnetic or electrostatic focusing, SAPHIRE can satisfy the highest spatial resolution requirement for x-ray imaging. From the investigation of SAPHIRE with FEA pixel size of 50 μm, we found that the scintillator (CsI) is the limiting factor for the resolution of SAPHIRE. To investigate the spatial performance of HARP-FEA experimentally, we first used an optical source, instead of x-rays, removing the necessity of using a scintillaotor. The FEA pixel size is reduced to 20 μm. As shown in Fig. 1.08, the overlapping area between the base and gate electrodes defines the pixel size. Smaller pixel FEAs require thinner passive addressing lines and essentially no increase in cost. A small quantity of FE tips (121 tips) can be included in the pixel size of d_{el} = 20 μm and still provide sufficient emission current required for a wide dynamic range. Thus by using a prototype HARP-FEA optical sensor with an optical source the spatial performance can be better investigated.

In this chapter, we will experimentally investigate these two properties of the imaging performance of a 1" prototype HARP-FEA image sensor with magnetic focusing and FEA pixel size of 20 μm. The optical sensitivity, spatial resolution and noise characteristics were measured, and the results were compared with theoretical predictions using the HARP and FEA physical parameters. We also investigated the potential x-ray imaging performance of SAPHIRE by coupling the prototype HARP-FEA image sensor to the output of an x-ray imaging intensifier (XRII).

5.2 Materials and methods

5.2.1 Description of a prototype optical HARP-FEA image sensor

A 1" prototype optical HARP-FEA image sensor was used to investigate the imaging performance of the FEA readout method. A photograph of the sensor is shown in Fig. 5.01 (a). The FEA consists of 640 × 480 pixels with pixel size of 20 × 20 μm. The HARP target is 1" in diameter with an *a*-Se layer thickness of d_{Se} = 15 μm. The external driving electronics were bonded to the edge of the FEA substrate. The high voltage bias for the HARP layer was established through a metal pin inserted through the glass substrate. The images were read out at 30 frames per second in interlace mode. The output video signal can be digitized with a standard analog frame grabber. A micrograph of the FEA pixels is shown in Fig. 5.01 (b). Each pixel contains a matrix of 11 × 11 field emitter (FE) tips, which occupy an area of 14 × 14 μm in the center. To turn on field emission, the cone-shaped molybdenum (Mo) cathode is biased at ground potential and a positive bias, V_g (40-100 V), is applied to the gate electrode. This bias condition results in a very high electric field around the emitter tip due to its small area [88, 96] (~ 13Å^2) and causes field

emission. An active driving circuitry was built for the FEA using metal-oxide-semiconductor field effect transistors (MOSFET) technology. Each FEA pixel is addressed sequentially by turning on the MOSFET to apply the desired gate potential [50, 121]. The geometric parameters and the operating conditions of the prototype HARP-FEA image sensor are summarized in Table 5.01.

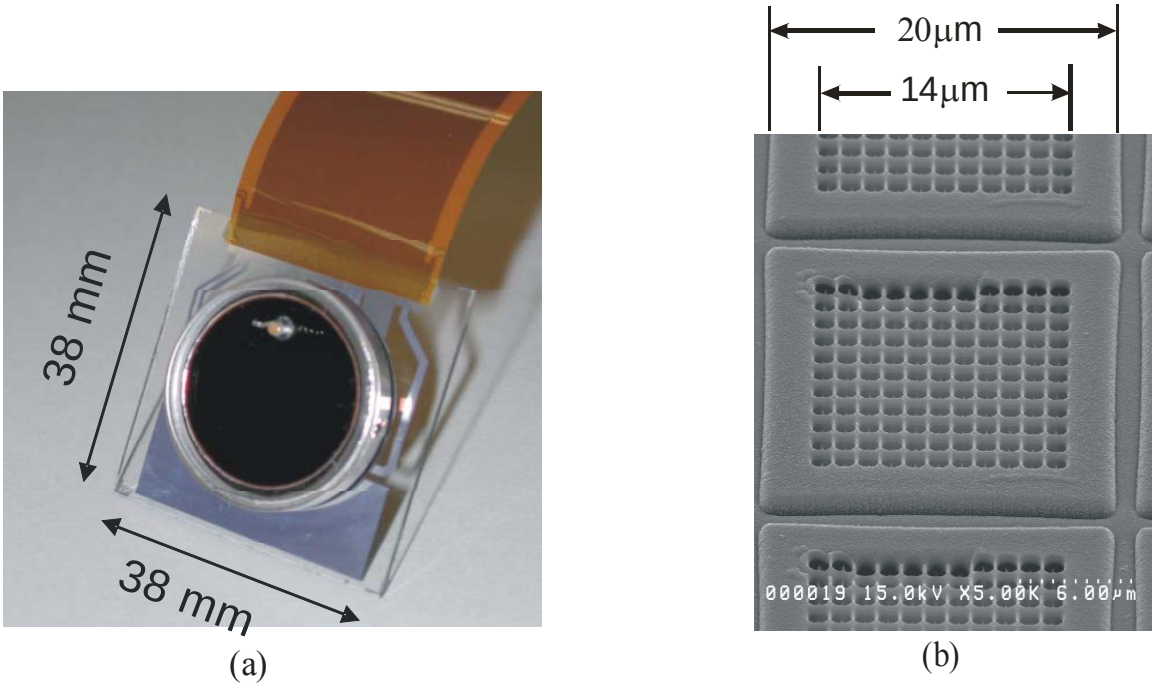

Figure 5.01: (a) A photography of the 1" optical HARP-FEA sensor with 640 × 480 pixels and a 15 μm thick *a*-Se layer; (b) A micrograph of the FEA pixels. The pixel pitch is 20 × 20 μm, and each pixel contains 121 FEA tips.

Table 5.01: Geometric parameters and operating conditions of the prototype HARP-FEA image sensor

HARP layer thickness	d_{Se}	15 μm
Pixel number	N_p	640 × 480
Pixel size	d_{el}	20 μm × 20 μm
Emitting area	d_a	14 μm × 14 μm
Magnetic field	B	0.125 T
Gate electrode potential	V_g	60 V
Mesh electrode potential	V_m	700 V

Effective emission current	I_e	7 μA
Distance between gate and mesh	L_{gm}	1.25 mm
Distance between mesh and target	L_{mt}	1.25 mm
FE tips number per pixel	n_p	11 × 11
Pixel turn-on time	t_p	80 ns

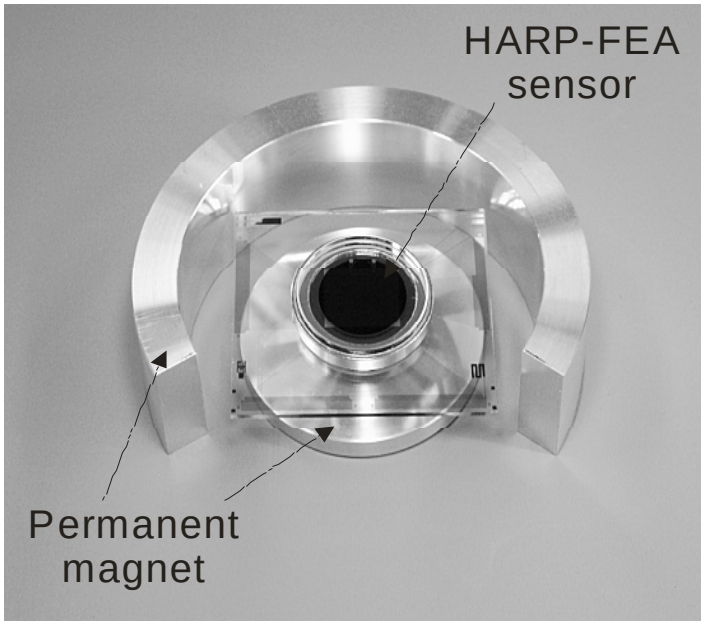

Figure 5.02: Photograph of prototype HARP-FEA sensor with permanent magnets.

As described in previous chapters [114], the electron beam emitted from the FEA spreads laterally before reaching the HARP target due to the oblique angle of emission. Although the mesh electrode inserted between the HARP target and FEA (Fig. 1.09) could reduce the lateral spread of electrons, it could still be significant (> 400 μm), depending on the signal intensity on the HARP target. This is a major source of image blur for SAPHIRE. To alleviate this problem, an external magnetic field was applied to the entire image sensor to focus the electron beam. Shown in Fig. 5.02 is a photograph of the sensor and its focusing magnets. Fig. 5.03 illustrates the principle of magnetic focusing. Under the external magnetic field, B, which is perpendicular to the surface of the HARP target, electrons emitted with an oblique angle follows a spiral trajectory

before landing on the HARP target. Hence, the lateral spread is less compared to without focusing (Fig. 1.09). It should be noted that it is virtually impossible to maintain a uniform external magnetic field for a large area SAPHIRE. Therefore, the electrostatic focusing method, which is accomplished by an integrated focusing electrode at each FE tip, is under investigation [114].

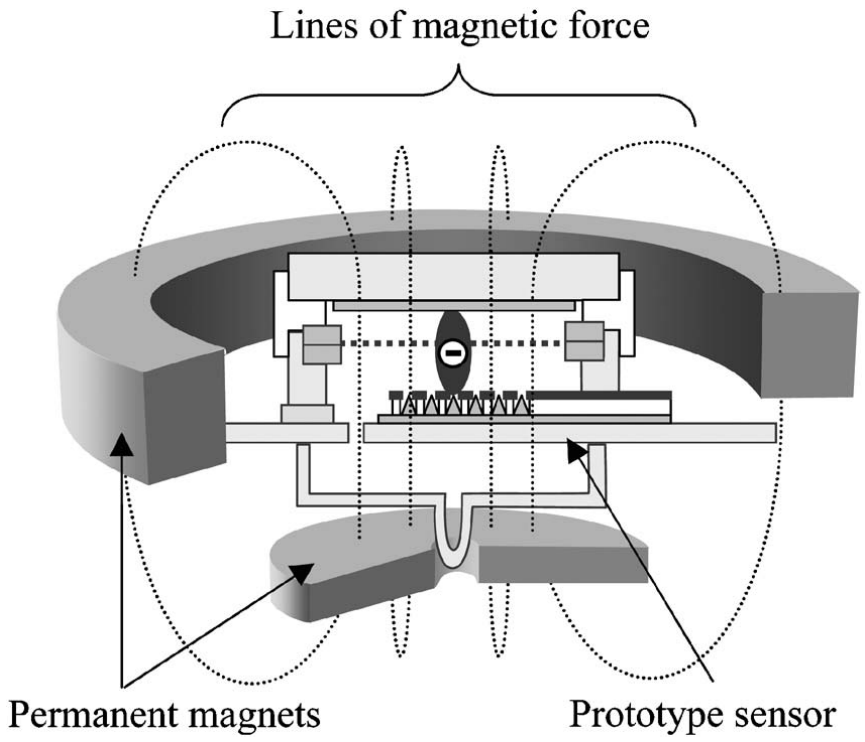

Figure 5.03: Schematic diagram showing the concept of magnetic focusing used for minimizing electron beam spread in the 1" prototype HARP-FEA image sensor

5.2.2 Optical sensitivity of the HARP-FEA image sensor

The effective quantum efficiency, η^*, of a HARP image sensor is defined as the total number of charge carriers produced by a single incident optical photon. It is the product of the optical quantum efficiency (η) and the avalanche multiplication gain (g_{av}):

$$\eta^* = \eta \times g_{av} . \qquad (5.01)$$

Both η and g_{av} have been investigated previously as a function of d_{Se} and E_{Se} [47, 52, 61, 62, 66]. The optical quantum efficiency of HARP follows Onsager theory, and depends on both E_{Se} and the wavelength, λ, of the optical photon [66]. The avalanche gain can be determined from E_{Se} using the expression [52].

$$g_{av} = \exp\left(d_{Se}\beta_1 \exp\left(-\beta_2 / E_{Se}\right)\right), \tag{5.02}$$

where $\beta_1 = 5.5 \times 10^3$ /μm and $\beta_2 = 1.029 \times 10^3$ V/μm are fitted constants from experimental measurements in Chapter 2.

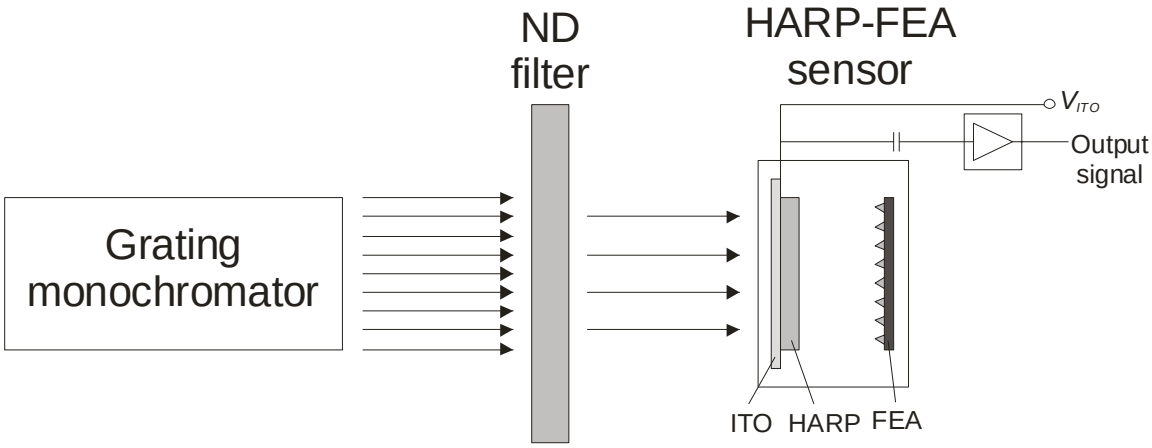

Figure 5.04: Schematic diagram showing the experimental setup for the measurement of optical sensitivity of HARP-FEA sensor.

The optical sensitivity of the prototype sensor was measured using green light with wavelength λ = 540 nm, which is closely matched to the peak emission wavelength of Thallium (Tl) doped CsI scintillators in SAPHIRE. The experimental setup is shown in Fig. 5.04. The signal current of the HARP-FEA image sensor was measured as a function of the HARP target bias potential V_{ITO}, which determines E_{Se} via $E_{Se} = \dfrac{V_{\mathrm{ITO}}}{d_{Se}}$. As g_{av} increases with V_{ITO}, the incident light intensity was attenuated with neutral density (ND) filters to avoid saturation of signal current in HARP. Therefore, the signal current per unit

incident photon intensity was recorded, which is expected to be proportional to η^*. The linearity of optical response was also measured at different V_{ITO} values.

5.2.3 Spatial Resolution

In this subsection, we will first predict the spatial resolution of the HARP-FEA image sensor. We start with the trajectories of the emitted electrons and the optimal choice for the magnetic field. We then calculate the spatial distribution of the electron beam intensity and the amount of signal charge read out from the target. The experiment measurement of MTF will be also presented.

A. Theoretical investigation

The concept of magnetic focusing has been shown in Figs. 3.09 and 5.03. The magnetic field results in a spiral trajectory for the emitted electrons. The steps of the theoretical calculation are similar to Chapter 3. However, since the geometry size (e.g., distance between target and FEA) and bias potential (e.g. V_m) have been changed, we may expect different optimal magnetic fields and subsequent calculations.

The first step is to investigate the lateral spread of electrons as a function of their emission angle θ [101]. This spiral trajectory of the emitted electrons projects to a circle in the x-y plane, which is parallel to the HARP surface. As derived in previous chapters, the lateral spread, *LS*, of the electrons is determined by the chord length between the starting and finishing points on the projected circle, which is given by:

$$LS = \frac{2}{B}\sqrt{\frac{2mV_g}{q}}\sin\theta \cdot \left|\sin\left(\frac{qBt_{gt}}{2m}\right)\right|, \tag{5.03}$$

where m is the mass of an electron, q is the elementary charge and t_{gt} is the time for an electron to travel from the gate to the HARP target:

$$t_{gt} = \frac{L_{gm}}{V_m - V_g}\sqrt{\frac{2m}{q}}\left(\sqrt{V_m - V_g \sin^2\theta} - \sqrt{V_g}\cos\theta\right) + \frac{L_{mt}}{V_m - V_t}\sqrt{\frac{2m}{q}}\left(\sqrt{V_m - V_g \sin^2\theta} - \sqrt{V_t - V_g \sin^2\theta}\right) \quad (5.04)$$

where V_t is the free surface potential of the HARP layer due to image charge accumulation, and the definitions and values of the HARP-FEA design parameters such as L_{gm}, L_{mt}, V_g and V_m are listed in Table 5.01. The lateral spread of electrons was calculated using Eq. 5.03 up to the critical emission angle θ_C, beyond which the emitted electrons do not have sufficient kinetic energy to reach the HARP target. θ_C is given by $\theta_C = \arcsin\left(\sqrt{V_t/V_g}\right)$ [99]. The focusing magnetic field only changes the direction of the lateral component of the electron velocity; hence it does not affect θ_C.

The next step is to determine the spatial distribution of the electron beam intensity as it reaches the HARP target, $I(x, y)$, for each pixel of the FEA with d_{el} = 20 μm × 20 μm. The electron beam intensity from a single tip, $I_0(x, y)$, was first obtained by substituting the inverse of the relationship between lateral spread and θ in Eq. 5.03 into the angular intensity distribution of field emission, $I_\theta(\theta)$, from a single tip and then converting the result to Cartesian coordinates:

$$I_0(x, y) = I_\theta\left(LS^{-1}(x, y)\right). \quad (5.05)$$

The distribution of $I_\theta(\theta)$ used in our calculation is shown in Fig. 3.11. The beam intensity for one pixel was then calculated by integrating $I_0(x, y)$ over all FE tips in the x and y directions with $N_x = N_y = 11$:

$$I(x,y) = \sum_{N_x}\sum_{N_y} I_0(x - n_x d_t, y - n_y d_t)\,. \tag{5.06}$$

The final step is to derive the pixel aperture function of the FEA readout method, $\mathrm{MTF}_{\mathrm{FEA}}(f_x, f_y)$ [114], which has been discussed in Chapter 3. It was calculated by taking the two-dimensional Fourier transform of the spatial distribution of the image charge on the target, $Q_a(x,y)$, that was read out by each FEA pixel. $Q_a(x, y)$ is given by the integral of $I(x, y)$ within the pixel readout time t_p:

$$Q_a(x,y) = \int_0^{t_p} I(x,y)dt\,. \tag{5.07}$$

$\mathrm{MTF}_{\mathrm{FEA}}(f_x, f_y)$ can then be obtained as the normalized Fourier transform of $Q_a(x,y)$:

$$\mathrm{MTF}_{\mathrm{FEA}}(f_x, f_y) = \frac{\left|\mathrm{FT}\left(Q_a(x,y)\right)\right|}{\left|\mathrm{FT}\left(Q_a(x,y)\right)\right|_{f_x=f_y=0}}\,. \tag{5.08}$$

where FT denotes the Fourier transform. The photo-electric conversion and avalanche process in HARP has been shown to have negligible blur in high definition optical HARP cameras that operates with an effective pixel size of 10~20 μm [61, 62]. Hence $\mathrm{MTF}_{\mathrm{FEA}}$ can be regarded as the presampling MTF of the HARP-FEA image sensor.

B. Experiment measurement of the MTF

The spatial resolution of the optical HARP-FEA image sensor was measured using the slanted edge method, which involves focusing a sharp optical edge onto the HARP target through lens. To facilitate quantitative evaluation of the images, the output video signal from the HARP-FEA sensor was digitized with an 8-bit analog frame grabber. The full range of the 8-bit digitization corresponds to a maximum signal current of 200 nA. To ensure good linearity of the measurement, the light intensity at each V_{ITO} was adjusted

such that the maximum digital count is < 200, which corresponds to ~ 160 nA of signal current and well within the linear range of the HARP sensitivity curves.

5.2.4 Noise characteristics

The optical noise power spectrum (NPS) of the HARP-FEA image sensor was measured as a function of light intensity and target bias potential, V_{ITO}. At each V_{ITO}, the light intensity was adjusted such that the mean signal current is well within the linear range of the HARP-FEA sensor response. At each operating condition, 60 image frames were acquired under uniform optical illumination of the HARP target. A region of interest (ROI) with 128 pixels × 128 pixels was selected, resulting in a total of 120 sub-images for the computation of 2D NPS. The 2D NPS was calculated as the ensemble average of the square of the Fourier transform of all mean subtracted ROI noise images [122]:

$$NPS(u,v) = \frac{d_x d_y}{N_x N_y} \left(\left| FT\left[I(x,y) - \bar{I}(x,y) \right] \right| \right)^2, \qquad (5.09)$$

where $I(x, y)$ and $\bar{I}(x,y)$ represent the image data and the average signal of each ROI, respectively. N_x and N_y are the numbers of elements in each ROI, and d_x and d_y are the pixel dimensions.

5.2.5 Potential x-ray imaging performance of SAPHIRE

In SAPHIRE, the CsI scintillator needs to be placed in direct contact with the HARP layer or coupled through a fiber optic faceplate (FOP) to minimize any loss of light and additional blur. Since the prototype HARP-FEA sensor has a 1 mm thick regular glass

faceplate, direct coupling with a CsI layer will introduce significant image blur. For the purpose of the present work, which is to demonstrate the advantages of HARP versus optical sensors without avalanche (e.g. a-Si photodiodes), we used lens coupling to focus an x-ray image onto the HARP target. Due to the limited light collection efficiency of lens coupling, we used the amplified optical image at the output of an x-ray image intensifier (XRII) so that the combined optical gain (XRII * lens coupling efficiency) was comparable to that of CsI(Tl) directly coupled to HARP in SAPHIRE. A diagram showing the experimental setup is shown in Fig. 5.05. This approach allowed us to investigate the noise characteristics of SAPHIRE. However, the spatial resolution may be limited by the additional conversion steps in the XRII/lens imaging chain.

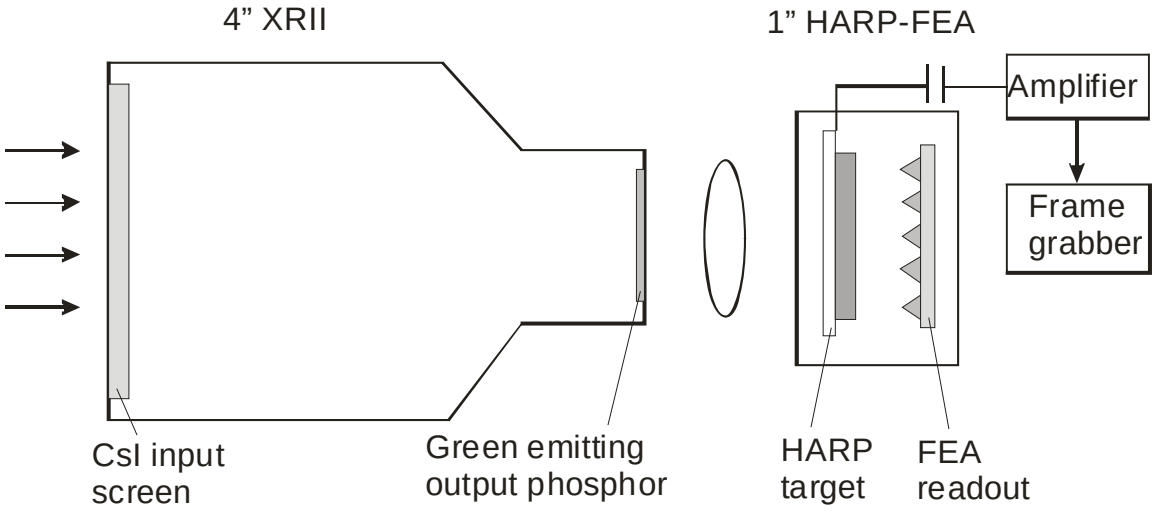

Figure 5.05: Diagram showing the imaging chain used to investigate the potential signal-to-noise performance of HARP-FEA structure in SAPHIRE.

The XRII used in our investigation has a 4" field of view (V7227, Hamamatsu Photonics, Hamamatsu, Japan). The input phosphor is a CsI(Na) screen with mass loading of ~90 mg/cm^2, and the peak emission wavelength of the output phosphor is 545 nm. The combined demagnification factor of the XRII and lens is ~ 6, resulting in an effective pixel size of 122 μm for the x-ray images read out by the HARP-FEA image

sensor. The total optical gain of the XRII/lens combination was estimated to be 1000 photons per 40 keV absorbed x-ray photon. Both conversion gain and pixel size are within the range expected for SAPHIRE. The peak wavelength of the light exiting the XRII is also similar to the emission spectrum of CsI (Tl) proposed for usage in SAPHIRE.

The x-ray imaging system was operated in continuous fluoroscopy mode using a micro-focal spot x-ray tube with tungsten target (L9631, Hamamatsu Photonics). An x-ray spectrum of 80 kVp with 2 mm Al and 1 mm Cu filter was used to simulate a typical spectrum with patient attenuation in fluoroscopy. During the x-ray experiment, the optical coupling of the imaging chain was fixed. The x-ray exposure rate to the input of the XRII varied from 0.2 to 78 μR per frame. The slanted edge method was used to measure the presampling MTF of the HARP-FEA based x-ray imaging chain. For NPS measurement, our investigation was focused on the programmable gain aspect of HARP. While the optical gain of the system was kept constant, the HARP target bias potential V_{ITO} was increased while the x-ray exposure rate decreased. This is to ensure an x-ray quantum noise limited performance. The V_{ITO} settings at different exposure rates are listed in Table 5.02. For each operating condition, 30 image frames were obtained under uniform x-ray exposures to compute the 2D NPS.

Table 5.02: Comparison of exposure, V_{ITO} settings, and the associated gain of the HARP layer used in the x-ray NPS measurement.

Exposure rate (μR/s)	0.20	1.20	3.91	19.85
HARP bias V_{ITO} (V)	1570	1540	1500	1420

5.3 Results and discussion

5.3.1 Optical sensitivity of the HARP-FEA image sensor

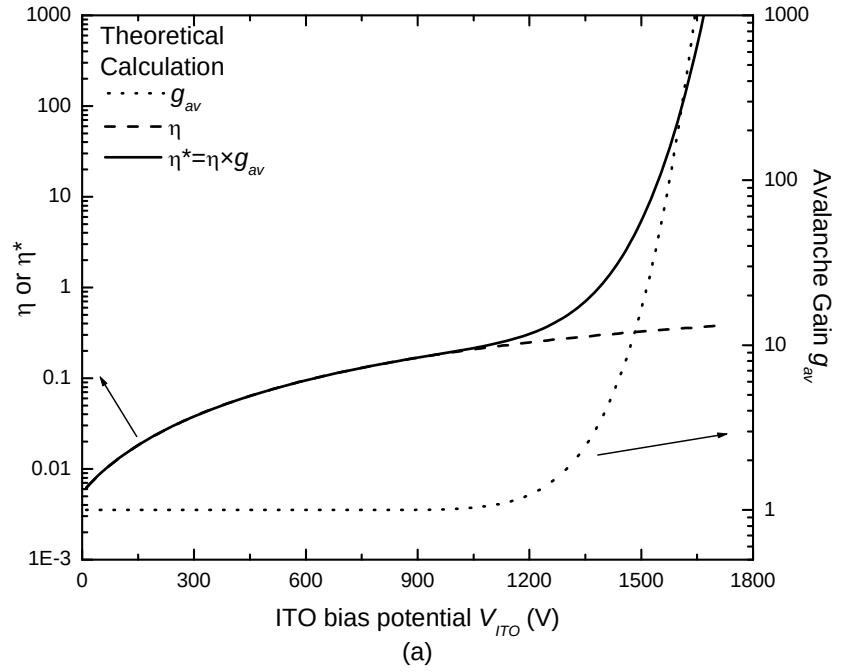

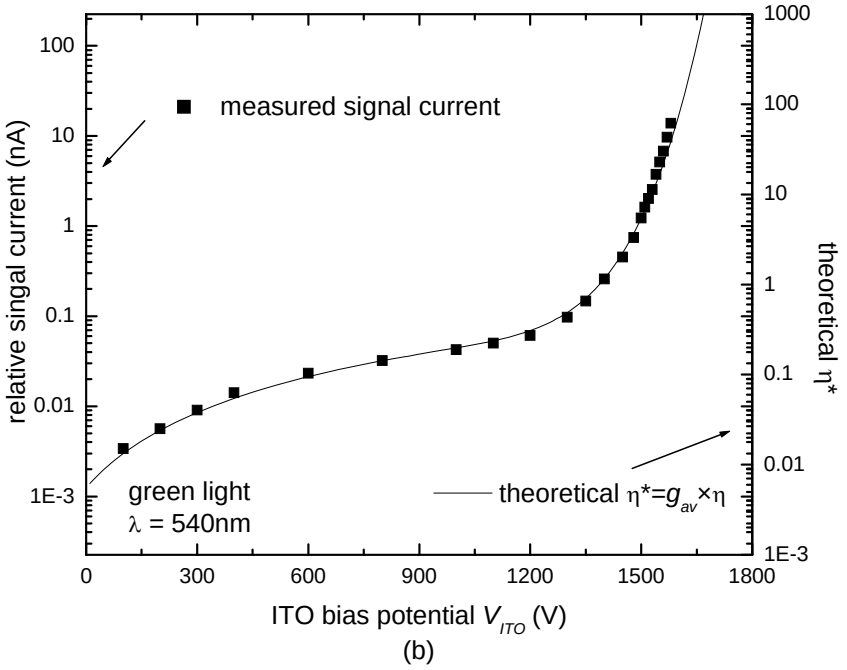

Figure 5.06: (a) Theoretical calculation of the effective quantum efficiency η* of the HARP-FEA sensor for green light (λ = 540 nm) as well as the optical quantum efficiency η and avalanche gain g_{av}. (b) Measured signal current per unit incident photon intensity for green light. The theoretical value of η* is plotted for comparison. The shapes of measured and calculated results are in excellent agreement.

The optical quantum efficiency, η, was obtained for λ = 540 nm as a function of V_{ITO} and shown in Fig. 5.06 (a). Plotted in the same figure are the calculated avalanche gain, g_{av}, using Eq. 5.02 and the resulted effective quantum efficiency, η*. Fig. 5.06 (a) shows that for V_{ITO} < 1200 V, which corresponds to E_{Se} = 80 V/μm for d_{Se} = 15 μm, there is no avalanche gain. Therefore η* is equal to η, which increases sub-linearly as a function of E_{Se} for green light. As V_{ITO} increases above 1200 V, avalanche starts to occur and g_{av} increases exponentially, as does η*. The experimental measurement of the signal current as a function of V_{ITO} is shown in Fig. 5.06 (b). Plotted in the same figure for comparison is the calculated η*. The shapes of the two curves match very well. With further increase in V_T, the signal current increases exponentially, indicating the onset of avalanche gain in *a*-Se. Increasing V_{ITO} = 1300 V to 1570 V, the signal current increases by two orders of magnitude. The sensitivity of the HARP increases considerably.

Shown in Fig. 5.07 is the linearity measurement of the HARP-FEA image sensor with V_{ITO} = 1200 V, 1500V, and 1560V, respectively. Plotted in the same figure is the linear fitting of the data. It shows that for signal current I_S < 200 nA, the signal response has good linear performance at V_{ITO} = 1200 V and 1500V. I_S = 200 nA corresponds to a potential of ~ 15 V on the bottom (free) surface of the HARP layer due to the accumulation of holes. This is ~ 1 % of the bias potential on the ITO and therefore, will not decrease E_{Se} significantly. At higher incident light intensity, the reduction of E_{Se} due to accumulated holes will start to decrease sensitivity and make the curve sub-linear, as shown in Fig. 5.07. At V_{ITO} = 1560 V, the linear performance is only good up to 100nA, due to the reason the self-reduction of g_{av} is more significantly at high E_{Se} as we described in Chapter 2. At higher bias potentials, the sensitivity curve shifts to the left

due to the higher avalanche gain. The decrease in sensitivity as exposure increases is advantageous for ensuring a wide dynamic range of the detector. For the purpose of linear system analysis and measurement of detector performance, the HARP layer should be operated in the linear range. Otherwise linearization needs to be performed before calculation of MTF and NPS.

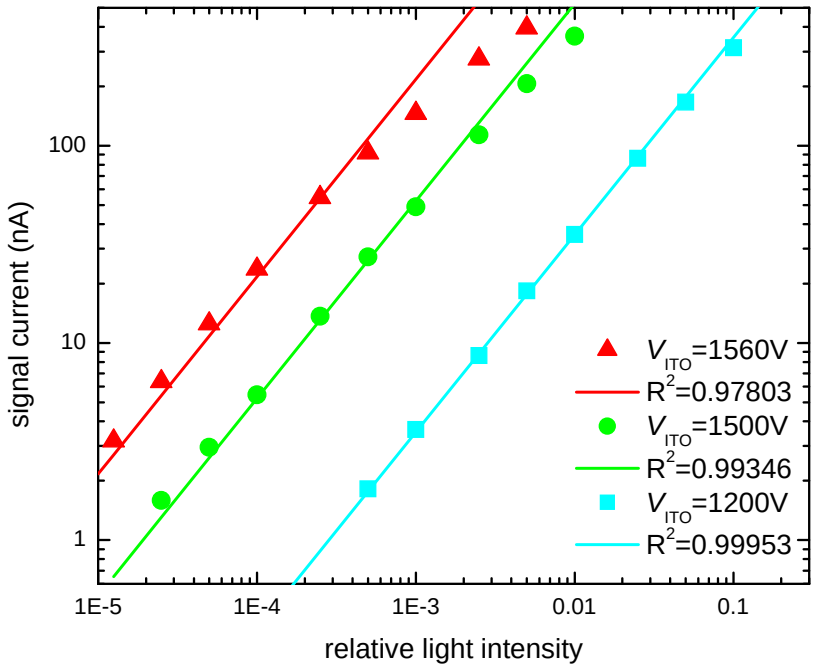

Figure 5.07: The signal current of the HARP-FEA sensor measured as a function of the incident light intensity at different target bias potentials to show the linearity.

5.3.2 Spatial Resolution

1. Theoretical investigation

The lateral spread of electrons with magnetic focusing was calculated using Eq. 5.03 with the FEA parameters listed in Table 5.01. Shown in Fig. 5.08 are the calculated values of lateral spread as a function of B with V_t = 1.5V, 6V, 12V and 20V at $\theta = \theta_C$. Fig. 5.08 shows that there are local minimums for lateral spread, which correspond to

complete rotations of electrons in their spiral trajectory, i.e. multiples of 360°. The first minimums for different V_t are within a close range of B values (0.12 – 0.13 T). Shown in Fig. 5.09 is the calculated lateral spread as a function of electron emission angle θ (up to θ_c) for different V_t at B = 0.125T. It shows that the lateral spread of the electron beam can be as high as 30 μm and its maximum values LS_{max} does not occur at $\theta = \theta_C$. The LS_{max} in Fig. 5.09 was then determined for each V_t value, and plotted as a function of V_t in Fig. 5.10 for three magnetic fields: B = 0.12 T, 0.125 T and 0.13 T. It shows that B = 0.125 T provides the smallest lateral spread. This magnetic field strength was chosen for the prototype HARP-FEA image sensor.

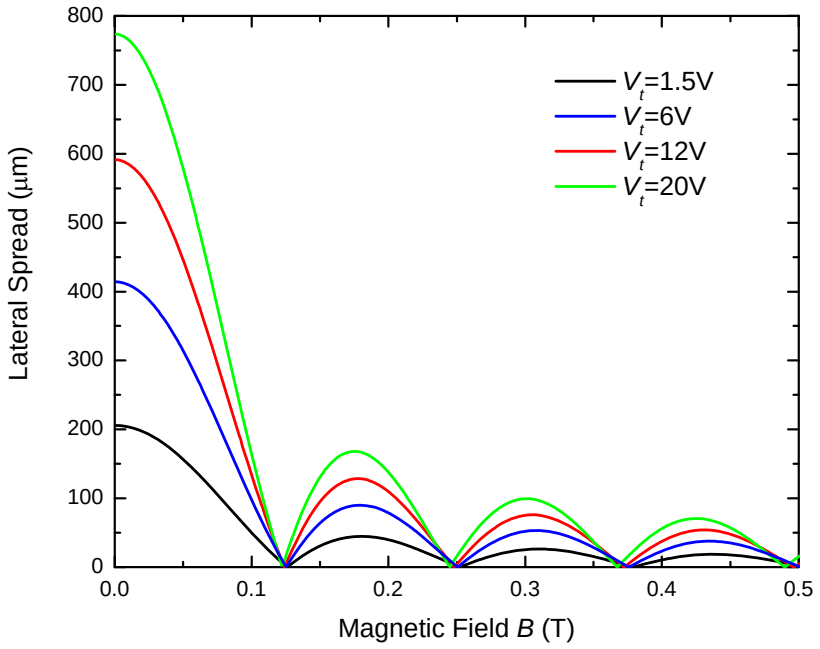

Figure 5.08: Lateral spread as function of magnetic field for electrons with $\theta = \theta_C$. The other conditions are listed in Table 5.01.

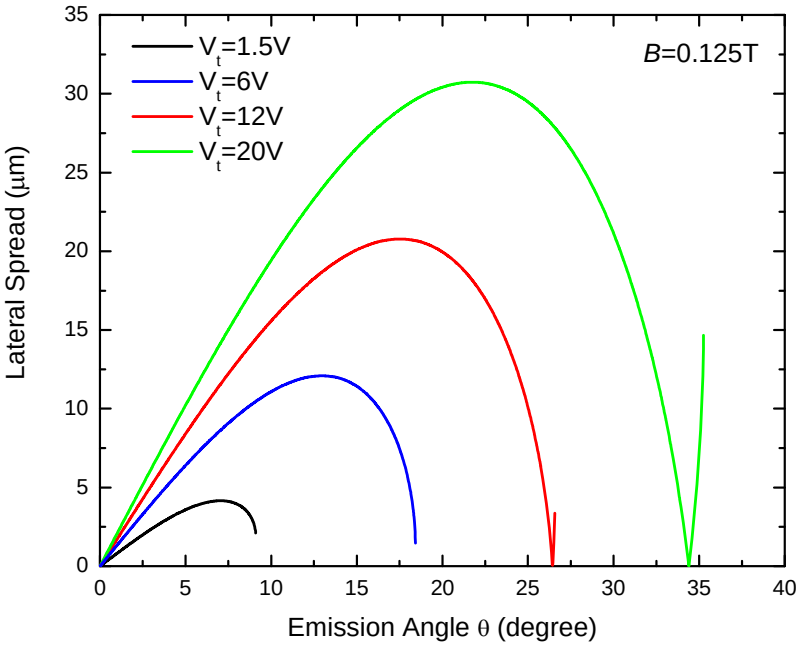

Figure 5.09: Lateral spread as function of emission angle up to θ_C at different V_t with B = 0.125 T. The other conditions are listed in Table 5.01.

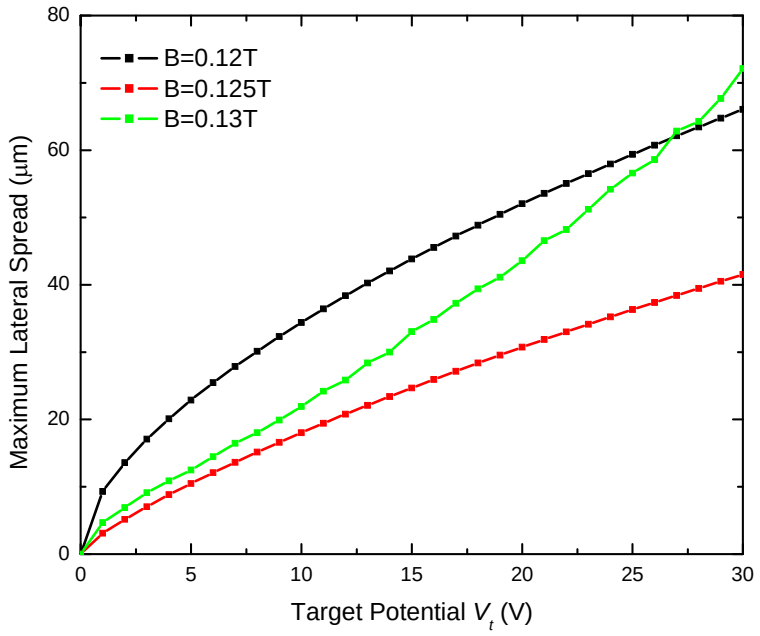

Figure 5.10: Maximum lateral spread as function of V_t at three different B-values. The other conditions are listed in Table 5.01. The optimal choice is B = 0.125 T.

The spatial distribution of the electron beam intensity from one single FE tip, $I_0(x, y)$, was obtained using Eq. 5.05. The inverse relation between the lateral spread $LS(x, y)$ and θ was obtained from Eq. 5.03. Since $I_0(x, y)$ has circular symmetry, the results of the $I_0(x, y)$ calculation are shown in Fig. 5.11 as a function of x only (with $y = 0$). These results are consistent with those shown in Fig. 5.09. At higher V_t (e.g., V_t = 12V), electrons emitted with larger θ can complete one rotation in the spiral trajectory and return to the origin, resulting in high beam intensity near the origin, whereas lower V_t (e.g., V_t = 6V) would not permit complete rotation for electrons, hence the intensity near the origin is smaller.

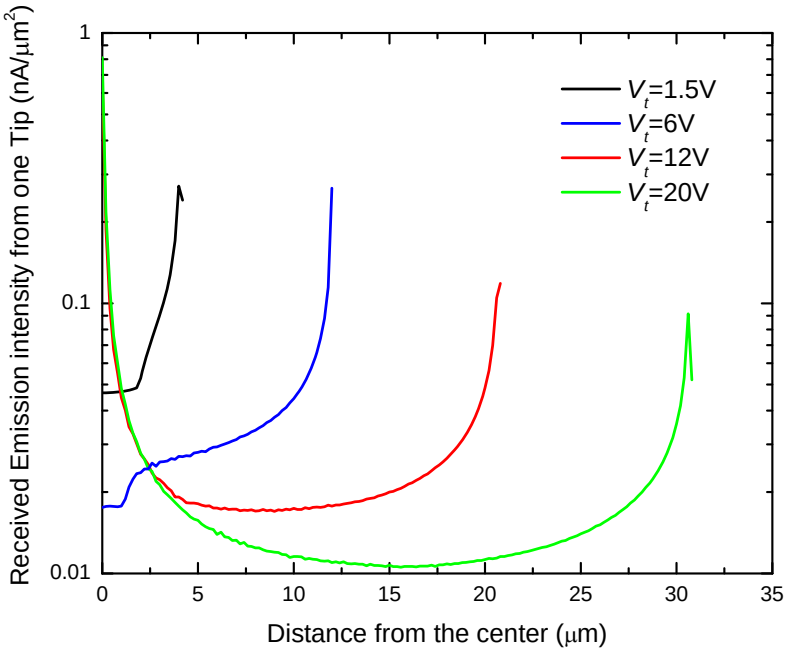

Figure 5.11: Maximum lateral spread as function of V_t at three different B-values. The other conditions are listed in Table 5.01. The optimal choice is B = 0.125 T.

The results of $I_0(x, y)$ shown in Fig. 5.11 were used to calculate $I(x, y)$ for an entire pixel with 121 FE tips using Eq. 5.06, and the results are shown in Fig. 5.12. For each intensity image of $I(x, y)$ in Fig. 5.12, the square in the center represents the emission area

of 14 μm × 14 μm, the outer square represents the pixel size d_{el} = 20 μm of the FEA, and the boundary of 100 μm × 100 μm shows the extent of electron beam spreading. It shows that the readout electron beam spot shrinks as the HARP target free surface potential V_t drops during readout. This results in signal dependence of spatial resolution, whereas the spatial resolution of FEA with electrostatic focusing, proposed by us previously, is independent of signal [114].

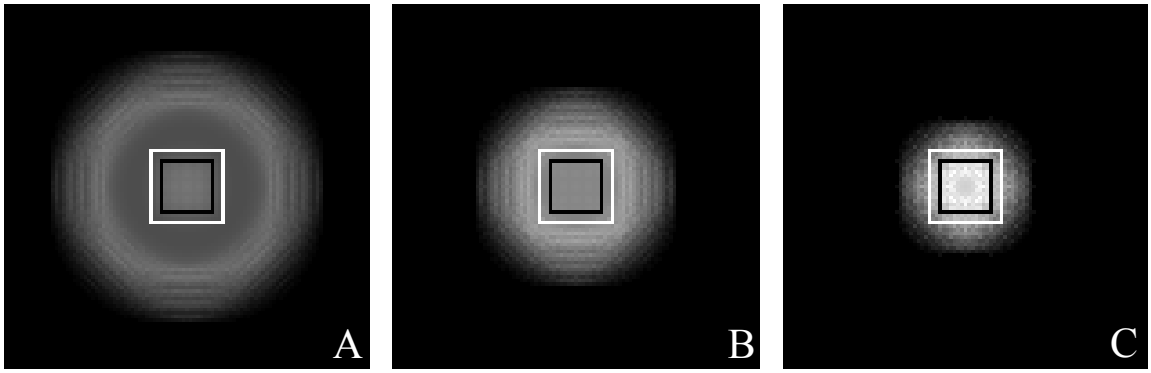

Figure 5.12: Electron beam intensity profile $I(x, y)$ for one pixel of the FEA with different HARP target free surface potential V_t: A: V_t = 20V; B: V_t = 12V; and C: V_t =6V. The boundary of each graph measures 100 μm × 100 μm, the outer square shows the pixel size of 20 μm× 20 μm; and the inner square shows the emitting area of 14 μm × 14 μm. All figures are plotted with the same grey scale representation of beam intensity.

The spatial distribution of the image charge read out by each FEA pixel, $Q_a(x, y)$, was obtained using Eq. 5.07, which shows that the initial target surface potential, V_t, also affects $Q_a(x, y)$. The results of $Q_a(x, y)$ with readout time t_p = 80 ns are shown in Fig. 5.13 for different V_t values. Since $Q_a(x, y)$ has circular symmetry, the results are plotted as a function of x only (with y = 0). It shows that the shape of Q_a is essentially flat for the majority of the pixel area, indicating complete charge readout. At the pixel boundary Q_a drops more quickly for lower V_t due to the smaller lateral spread of electron beams.

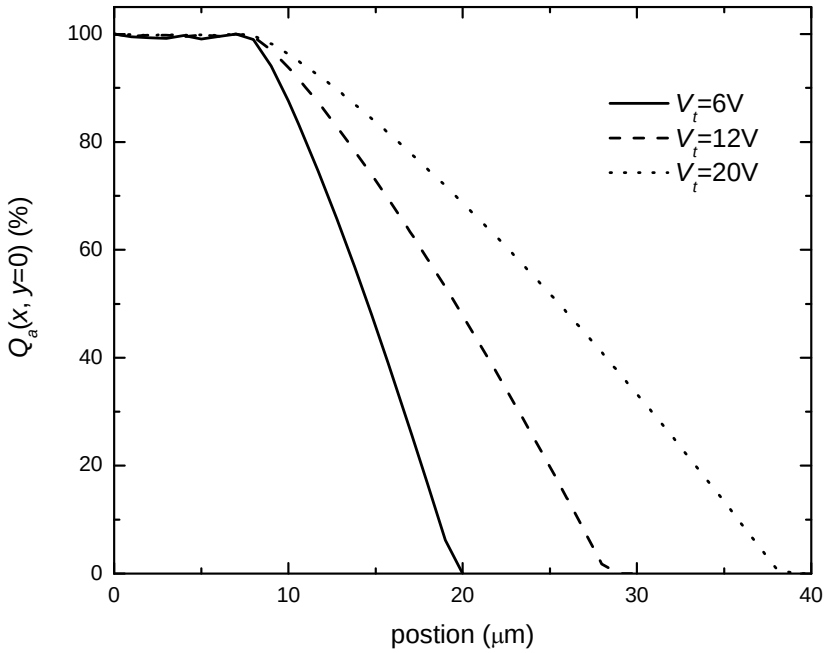

Figure 5.13: The spatial distribution of image charge, $Q_a(x, y=0)$, that is read out from each pixel of the FEA within t_p = 80 ns. The initial target surface potential V_t are 6V, 12V and 20V.

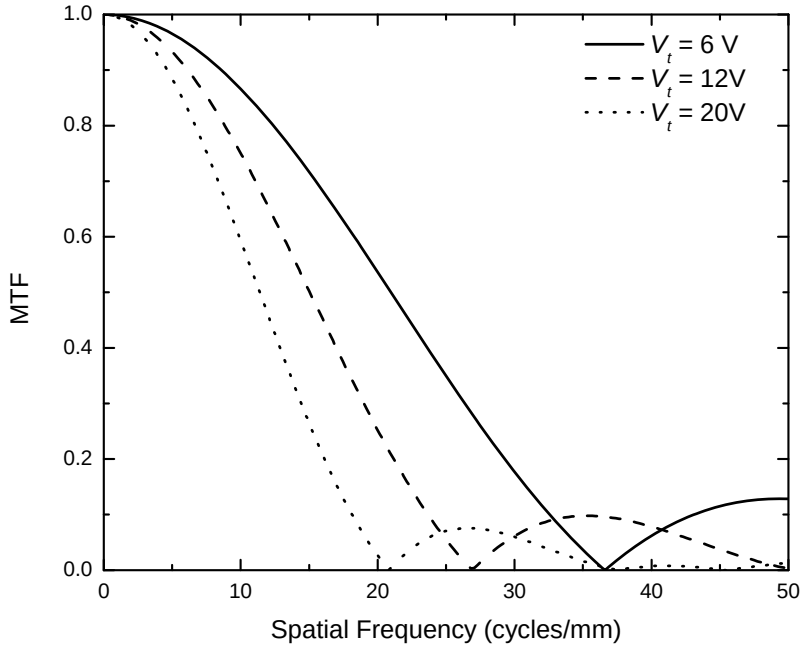

Figure 5.14: The calculated presampling MTF of the HARP-FEA image sensor with different initial V_t. The MTF has circular symmetry.

The pixel aperture function, $MTF_{FEA}(f_x, f_y)$ was then calculated as the Fourier transform of $Q_a(x, y)$ using Eq. 5.08. The results are shown in Fig. 5.14 as a function of f_x due to circular symmetry. At 10 cycles/mm, the values for MTF_{FEA} are 86%, 75% and 60%, for V_t = 6V, 12V and 20V, respectively. It shows that MTF is better with small signal levels.

2. Experimental measurement of the presampling MTF

Fig. 5.15 shows the measured presampling MTF of the HARP-FEA image sensor in the horizontal (scanning) and vertical (cross-scanning) directions. In the vertical direction, the first zero is at 45 cycles/mm, which is slightly lower than the first zero of 50 cycles/mm for a square aperture function of 20 μm pixel size. It indicates that the magnetic focusing method is able to limit the lateral spread of the electron beam to within the pixel size. The MTF is considerably lower in the horizontal direction, with the MTF dropping to 10 % at 20 cycles/mm. This is due to the temporal low pass filter connected to the output of the video amplifier. The temporal frequency of the TV signal can be related to the spatial frequency of the images through $1/t_p = 1/d_{el}$, where t_p = 80 ns is the time spent on reading out one pixel of the FEA sensor. Therefore the temporal frequency bandwidth of 5 MHz corresponds to a spatial frequency bandwidth of 20 cycles/mm. The measured MTF in the vertical direction should thus be used as the spatial resolution of the FEA readout method.

The edge image used for MTF calculation has V_t values ranging from 1.5 V (dark) to 11 V (bright), and 1 ~ 2 pixels in each line where the edge intercepts have intermediate pixel values. The theoretical prediction of presampling MTF at V_t = 6 V, which is the

average pixel values of the edge image, is shown in Fig. 5.15 for comparison. Reasonable agreement was observed between the theoretical calculation and the measured presampling MTF in the vertical direction.

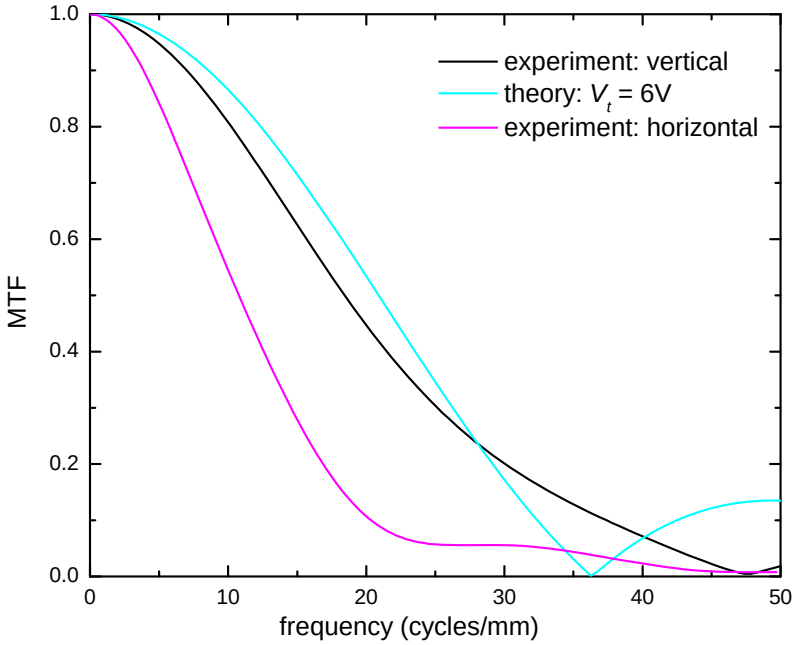

Figure 5.15: Measured presampling MTF in two directions of the 1" optical HARP-FEA sensor with 20 μm FEA pixel size, compared with the theoretical prediction of MTF at different conditions. The theory (blue line) is close to the measurement (black line).

5.3.3 Noise characteristics

The 2D NPS of the HARP-FEA sensor was measured under uniform illumination. Fig. 5.16 shows the measured NPS in both directions at V_{ITO} = 1560 V. In the horizontal direction (scanning direction), the shape of the NPS follows the square of the MTF, which suggests that quantum noise is the dominant source of noise. In the vertical direction (cross-scanning direction), however, the NPS first drops with frequency and then increases. This is due to the interlace readout of the HARP-FEA camera. The effects of different interlace readout schemes on the shape of the NPS in x-ray imaging systems

have been investigated thoroughly by Lai and Cunningham [123]. Here we will provide a brief description. The sampling frequency for each image field in interlace readout is one half of that in progressive readout. While the interleaving of two image fields recovered the full sampling frequency of the signal, the undersampled (and aliased) NPS cannot be recovered. In addition, the two image fields are only correlated for one half of the frame time. Therefore, there is a white noise component.

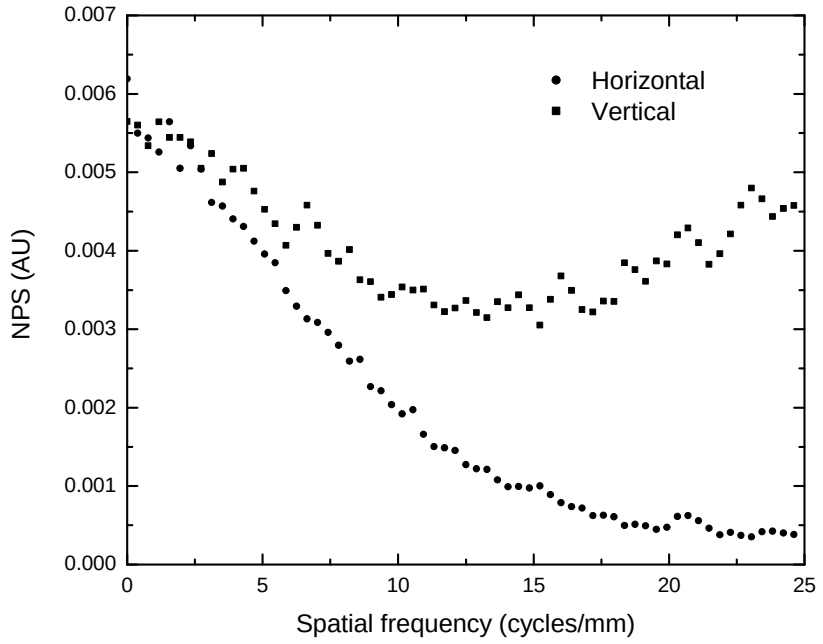

Figure 5.16: In both the horizontal and vertical directions of the HARP-FEA image sensor measured at V_T = 1560 V.

5.3.4 Potential x-ray image performance of SAPHIRE

The presampling MTF of the imaging chain was measured using the slanted edge method. Shown in Fig. 5.17 are the results in both directions of the FEA image sensor. Using the measured optical MTF (Fig. 5.15) and taking into account the optical demagnification factor of ~ 6, the presampling MTF due to the HARP-FEA sensor is

expected to be 0.73 at 2 cycles/mm in the vertical direction. Fig. 5.17 shows that the combined MTF of the imaging chain is 0.26 at 2 cycles/mm. We can thus deduce that the blur due to XRII is responsible for two thirds of the MTF drop.

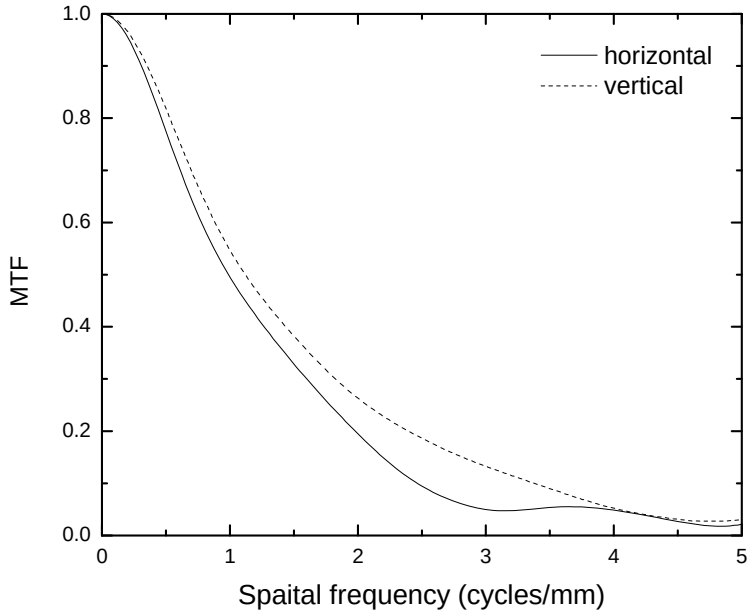

Figure 5.17: Measured x-ray presampling MTF of the imaging chain in both horizontal and vertical directions.

Shown in Fig. 5.18 (a) are the normalized NPS (NNPS) in both horizontal and vertical directions, calculated from uniform x-ray images made with detector exposure of 0.2 μR per frame and V_{ITO} = 1570 V. The signal is less than 50 nA and it can be regarded as being operated in linear range. The NNPS is calculated by dividing NPS by the square of the mean signal. The avalanche gain g_{av} at V_{ITO} = 1570 V is calculated to be 84 from Eq. 5.03. Fig. 5.18 (a) shows that the NPS in the horizontal direction follows the square of the MTF, indicating x-ray quantum noise limited performance. In the vertical direction, the NPS first shows a decrease following the square of the MTF, then an increase, which is the signature of interlaced image readout.

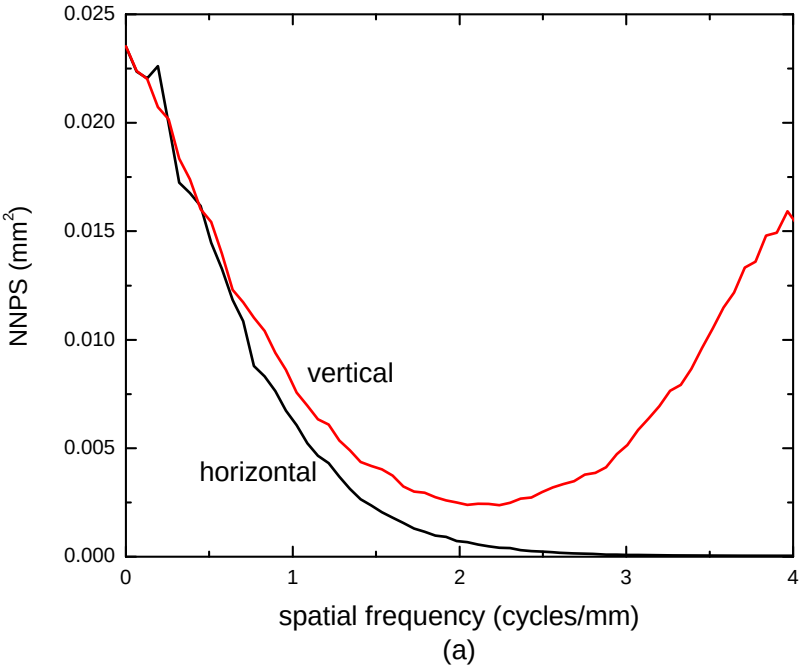

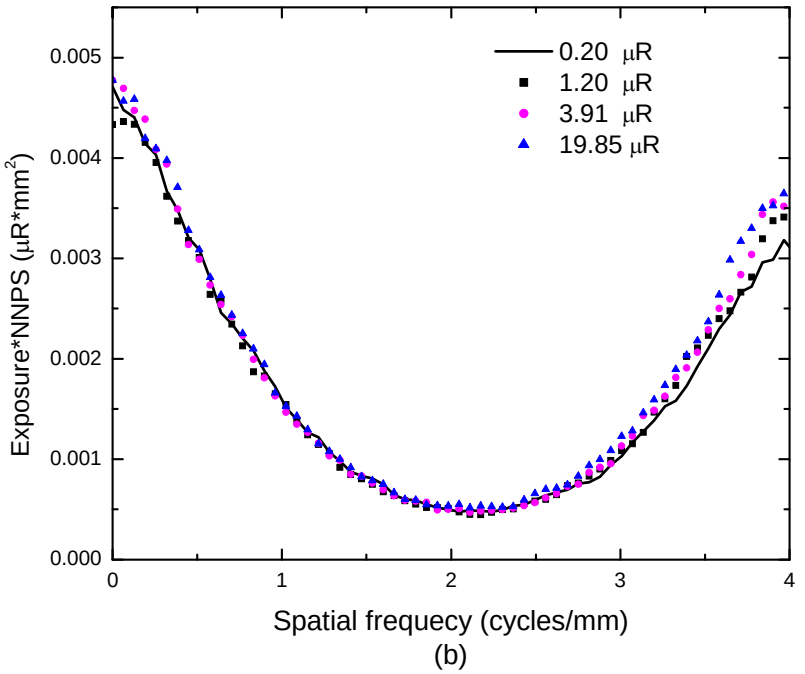

Figure 5.18: (a) Measured NPS from the imaging chain: NPS normalized by square of mean signal at 0.2 μR/frame; and (b) the product of exposure and NNPS at different exposures and avalanche gain.

Fig. 5.18 (b) shows the exposure normalized NPS, which is defined as the product of the x-ray exposure with the NNPS, for the exposure values listed in Table 5.02. The corresponding avalanche gains are 4.8, 16.5, 39 and 84 for the four different exposure rates, respectively. For clarity, only the NPS data in the vertical direction are shown. The curves virtually overlap with each other, indicating that x-ray quantum noise limited performance is maintained throughout the exposure range by increasing the avalanche gain of the HARP layer at low x-ray exposures.

5.4 Discussion and conclusions

In the present chapter we investigated the sensitivity, spatial resolution and noise properties of a prototype HARP-FEA image sensor and its potential x-ray imaging performance. Our results show that a wide dynamic range can be obtained with the programmable avalanche gain of HARP-FEA. With magnetic focusing of the emitted electron beam, the measured presampling MTF is comparable to the pixel width of the FEA. It is important to point out that the magnetic focusing method used in the prototype 1" HARP-FEA image sensor is not intended for large-area SAPHIRE. Electrostatic focusing method by integrating an additional focusing electrode onto the FEA substrate is being investigated for SAPHIRE, and its performance is expected to be more uniform and signal independent compared to magnetic focusing [124, 125].

In order to demonstrate the advantages of programmable avalanche gain of HARP for SAPHIRE, an XRII-lens imaging chain was used to focus a minified x-ray image onto the HARP target of the FEA image sensor. It has equivalent x-ray to optical photon conversion gain and effective pixel size expected for SAPHIRE. This approach allowed

us to investigate the potential signal and noise characteristics of the FEA readout method when used in SAPHIRE. Our results show that a HARP target thickness of d_{Se} = 15 μm is sufficient to produce x-ray quantum noise limited images at the lowest exposures expected for fluoroscopy. One of our ongoing investigations is to make the HARP multi-layer structure on top of a FOP substrate (instead of a regular glass substrate) so that the HARP-FEA image sensor can be placed in direct contact with CsI (Tl) x-ray scintillators.

Chapter 6

Future work

Our SAPHIRE was proposed to improve the digital detector's low dose performance with high resolution. It is made by optically coupling a scintillator with a thin layer of HARP, and the charge image is read out by the electron beams generated by Spindt-type FEA. It has two major advantages: (1) HARP layer has programmable avalanche gain, which can be turned on to enhance the detector's low dose performance and turned off at high exposure, so that it ensures a wide dynamic range; (2) FEA can provide small pixel size and rapid readout, which can preserve more information.

Based on the current study, some work may be undertaken in the future

6.1 Experimental investigation of Spindt-type FEA with inherent electrostatic focusing

As we described in Chapter 3, one of the advantages of Spindt-type FEA is its more stable emission and relatively smaller angular distribution. Spindt-type FEA, along with

other types of FEA, has been widely applied to field emission displays where the target (phosphor) is biased with a potential higher than thousand volts. However, for image sensors, as we see in Chapter 3, the lateral spread of emitted electrons can be more than 400 μm under some conditions if there is no additional focusing design. Magnetic focusing was proposed as a solution [101]. It can not only reduce the lateral spread but also relax requirements such as the distance between HARP and FEA as well as the bias potential. It has been successfully applied as a small area image sensor, however, it is difficult to implement in a larger area medical image detector while maintaining a uniform magnetic field.

It would be very interesting to fabricate a Spindt-type FEA with an inherent electrostatic focusing design, as shown in Fig. 3.10. This multi-layer structure of Spindt-type FEA is widely believed to limit angular distribution of emission, which is good in two aspects of SAPHIRE: 1, it can further improve spatial performance; 2, it can reduce the effective energy spread among emitted electrons, where angular distribution is the dominant source as we analyzed in Chapter 4. This would improve its temporal performance, i.e. lag, significantly. It would be very fruitful to repeat the experiment using Spindt-type FEA with inherent electrostatic focusing design.

6.2 Alternative type of FEA

Besides Spindt-type FEA, a new type of FEA with metal-insulator-semiconductors (MIS) structure is being investigated for applying in image sensor [126]. In contrast to Spindt-type FEA, its advantages include a simple structure and its electron emission characteristics, which are insensitive to operating pressure. Its disadvantage is that the

electron-emission efficiency, which is defined as the ratio of the emission current to the total tunneling current flowing through the diode, is very low (1%). Some efforts are being made to increase the electron-emission efficiency and an active matrix High Efficiency Electron-emission Device (HEED) has been reported to have an electron-emission efficiency as high as 28% and been applied in image sensors [127].

Bibliography

[1] W. Zhao, D. C. Hunt, K. Tanioka and J. A. Rowlands, "Indirect flat-panel detector with avalanche gain," Medical Imaging 2004: Physics of Medical Imaging, **5368**, pp. 150-161 (2004).

[2] S. Itoh, T. Watanabe, K. Ohtsu, M. Taniguchi, S. Uzawa and N. Nishimura, "Experimental Study of Field-Emission Properties of the Spindt-Type Field Emitter," Journal of Vacuum Science & Technology B **13**, 487-490 (1995).

[3] W. Zhao, G. Ristic and J. A. Rowlands, "X-ray imaging performance of structured cesium iodide scintillators," Medical Physics **31**, 2594-2605 (2004).

[4] "Cancer Facts and Figures 2008", (American Cancer Society, 2008), pp. 1-70. http://www.cancer.org/docroot/STT/stt_0_2008.asp?sitearea=STT&level=1

[5] S. H. Landis, T. Murray, S. Bolden and P. A. Wingo, "Cancer statistics, 1999," Ca-a Cancer Journal for Clinicians **49**, 8-31 (1999).

[6] "Cancer Facts and Figures 2007", (American Cancer Society, 2007), pp. 1-54. http://www.cancer.org/docroot/STT/stt_0_2007.asp?sitearea=STT&level=1

[7] "Breast Cancer Facts and Figures 2007-2008", (American Cancer Society, 2008), pp. 1-34. http://www.cancer.org/docroot/STT/stt_0_2008.asp?sitearea=STT&level=1

[8] M. J. Yaffe, "Digital Mammography," in *Categorical Course in Diagnostic Radiology Physics: Physical Aspects of Breast Imaging - Current and Furture Considerations,* edited by A. G. H. a. M. J. Yaffe (RSNA, 1999), pp. 229-238.

[9] S. A. Feig, "Decreased breast-cancer mortality through mammographic screening - results of clinical trials," Radiology **167**, 659-665 (1988).

[10] S. A. Feig, "Estimation of currently attainable benefit from mammographic screening of women aged 40-49 years," Cancer **75**, 2412-2419 (1995).

[11] C. T. Chantler, K. Olsen, R. A. Dragoset, J. Chang, A. R. Kishore, S. A. Kotochigova and D. S. Zucker, "X-Ray Form Factor, Attenuation and Scattering Tables,"(2005), Available: http://physics.nist.gov/ffast, (National Institute of Standards and Technology, 2005), Accessed on 2009, March 5

[12] P. C. Johns and M. J. Yaffe, "X-ray characterization of normal and neoplastic breast tissues," Physics in Medicine and Biology **32**, 675-695 (1987).

[13] M. J. Yaffe, "Digital mammography," in *Handbook of Medical Imaging*, *Vol. 1: Physics and Psychophysics,* edited by J. Beutel, H. L. Kundel and R. L. Van Metter (SPIE Press, Bellingham, 2000), pp. 329-372.

[14] V. P. Jackson, R. E. Hendrick, S. A. Feig and D. B. Kopans, "Imaging of the radiographically dense breast," Radiology **188**, 297-301 (1993).

[15] N. F. Boyd, B. Osullivan, J. E. Campbell, E. Fishell, I. Simor, G. Cooke and T. Germanson, "Mammographic patterns and bias in breast-cancer detection," Radiology **143**, 671-674 (1982).

[16] A. Karellas, S. Vedantham and S. Suryanarayanan, "Digital Mammography Image Acquisition Technology," in *Categorical Courses in Diagnostic Radiology Physics: Advances in Breast Imaging: Physics, Technology, and Clinical Applications,* edited by A. Karellas and M. Giger (RSNA, 2004), pp. 87-101.

[17] S. A. Feig and M. J. Yaffe, "Digital mammography," Radiographics, 893-901 (1998).

[18] M. M. Tesic, M. F. Piccaro and B. Munier, "Full field digital mammography scanner," European Journal of Radiology **31**, 2-17 (1999).

[19] J. G. Mainprize, N. L. Ford, S. Yin, T. Tumer and M. J. Yaffe, "A slot-scanned photodiode-array/CCD hybrid detector for digital mammography," Medical Physics **29**, 214-225 (2002).

[20] S. Muller, "Full-field digital mammography designed as a complete system," European Journal of Radiology **31**, 25-34 (1999).

[21] B. T. Polischuk, H. Rougeot, K. Wong, A. Debrie, E. Poliquin, M. Hansroul, J.-P. Martin, T.-T. Truong, M. Choquette, L. Laperriere and Z. Shukri, "Direct conversion detector for digital mammography," Medical Imaging 1999: Physics of Medical Imaging, **3659**, pp. 417-425 (1999).

[22] E. L. Gingold, D. L. Y. Lee, L. S. Jeromin, B. G. Rodricks, M. G. Hoffberg and C. L. Williams, "Development of a novel high-resolution direct conversion x-ray detector," Medical Imaging 2000: Physics of Medical Imaging, **3977**, pp. 185-193 (2000).

[23] J. A. Rowlands and J. Yorkston, "Flat panel detectors for digital radiography," in *Handbook of Medical Imaging*, *Vol. 1: Physics and Psychophysics,* edited by J. Beutel, H. L. Kundel and R. L. Van Metter (SPIE Press, Bellingham, 2000), pp. 223-328.

[24] D. B. Kopans, "Future directions for breast imaging," in *Categorical Course in Diagnostic Radiology Physics: Physical Aspects of Breast Imaging – Current and Future Considerations,* edited by A. G. H. a. M. J. Yaffe (RSNA, 1999), pp. 243-247.

[25] L. T. Niklason, B. T. Christian, L. E. Niklason, D. B. Kopans, D. E. Castleberry, B. H. OpsahlOng, C. E. Landberg, P. J. Slanetz, A. A. Giardino, R. Moore, D. Albagli, M. C. DeJule, P. F. Fitzgerald, D. F. Fobare, B. W. Giambattista, R. F. Kwasnick, J. Q. Liu, S. J. Lubowski, G. E. Possin, J. F. Richotte, C. Y. Wei and R. F. Wirth, "Digital Tomosynthesis in breast imaging," Radiology **205**, 399-406 (1997).

[26] S. Suryanarayanan, A. Karellas, S. Vedantham, S. J. Glick, C. J. D'Orsi, S. P. Baker and R. L. Webber, "Comparison of tomosynthesis methods used with digital mammography," Academic Radiology **7**, 1085-1097 (2000).

[27] X. Liu and C. C. Shaw, "a-Si:H/CsI(Tl) flat-panel versus computed radiography for chest imaging applications: image quality metrics measurement," Medical Physics **31**, 98-110 (2004).

[28] P. Monnin, D. Gutierrez, S. Bulling, D. Lepori, J. F. Valley and F. R. Verdun, "Performance comparison of an active matrix flat panel imager, computed radiography system, and a screen-film system at four standard radiation qualities," Medical Physics **32**, 343-350 (2005).

[29] S. Vedantham, A. Karellas, S. Suryanarayanan, D. Albagli, S. Han, E. J. Tkaczyk, C. E. Landberg, B. Opsahl-Ong, P. R. Granfors, I. Levis, C. J. D'Orsi and R. E. Hendrick, "Full breast digital mammography with an amorphous silicon-based flat panel detector: Physical characteristics of a clinical prototype," Medical Physics **27**, 558-567 (2000).

[30] W. Zhao, W. G. Ji, A. Debrie and J. A. Rowlands, "Imaging performance of amorphous selenium based flat-panel detectors for digital mammography: Characterization of a small area prototype detector," Medical Physics **30**, 254-263 (2003).

[31] B. Zhao and W. Zhao, "Characterization of a direct full-field flat-panel digital mammography detector," Medical Imaging 2003: Physics of Medical Imaging, **5030**, pp. 157-167 (2003).

[32] K.-W. Jee, L. E. Antonuk, Y. El-Mohri, M. Maolinbay and Q. Zhao, "Evaluation of direct detection and indirect detection active matrix flat-panel imagers (AMFPIs) for digital mammography," Medical Imaging 2001: Physics of Medical Imaging, **4320**, pp. 13-23 (2001).

[33] J. T. Rahn, F. Lemmi, R. L. Weisfield, R. Lujan, P. Mei, J.-P. Lu, J. Ho, S. E. Ready, R. B. Apte, P. Nylen, J. B. Boyce and R. A. Street, "High-resolution high fill factor a-Si:H sensor arrays for medical imaging," Medical Imaging 1999: Physics of Medical Imaging, **3659**, pp. 510-517 (1999).

[34] D. Albagli, H. Hudspeth, G. E. Possin, J. U. Lee, P. R. Granfors and B. W. Giambattista, "Performance of advanced a-Si/CsI-based flat-panel x-ray detectors for mammography," Medical Imaging 2003: Physics of Medical Imaging, **5030**, pp. 553-563 (2003).

[35] D. C. Hunt, S. S. Kirby and J. A. Rowlands, "X-ray imaging with amorphous selenium: X-ray to charge conversion gain and avalanche multiplication gain," Medical Physics **29**, 2464-2471 (2002).

[36] N. Matsuura, W. Zhao, Z. Huang and J. A. Rowlands, "Digital radiology using active matrix readout: Amplified pixel detector array for fluoroscopy," Medical Physics **26**, 672-681 (1999).

[37] K. S. Karim, Y. K. Vygranenko, A. Avila-Munoz, D. A. Striakhilev, A. Nathan, S. Germann, J. A. Rowlands, G. Belev, C. Koughia, R. Johanson and S. O. Kasap, "Active pixel image sensor for large-area medical imaging," Medical Imaging 2003: Physics of Medical Imaging, **5030**, pp. 38-47 (2003).

[38] J. P. Lu, K. Van Schuylenbergh, J. Ho, Y. Wang, J. B. Boyce and R. A. Street, "Flat panel imagers with pixel level amplifiers based on polycrystalline silicon thin-film transistor technology," Applied Physics Letters **80**, 4656-4658 (2002).

[39] M. M. Schieber, H. Hermon, R. A. Street, S. E. Ready, A. Zuck, A. I. Vilensky, L. Melekhov, R. Shatunovsky, E. Meerson and Y. Saado, "Radiological x-ray response of polycrystalline mercuric-iodide detectors," Medical Imaging 2000: Physics of Medical Imaging, **3977**, pp. 48-55 (2000).

[40] R. A. Street, K. S. Shah, S. E. Ready, R. B. Apte, P. R. Bennett, M. Klugerman and Y. N. Dmitriyev, "Large-area x-ray image sensing using a Pbl[sub 2] photoconductor," Medical Imaging 1998: Physics of Medical Imaging, **3336**, pp. 24-32 (1998).

[41] R. A. Street, S. E. Ready, K. Van Schuylenbergh, J. Ho, J. B. Boyce, P. Nylen, K. Shah, L. Melekhov and H. Hermon, "Comparison of PbI_2 and HgI_2 for direct detection active matrix x-ray image sensors," Journal of Applied Physics **91**, 3345-3355 (2002).

[42] M. Z. Kabir and S. O. Kasap, "Charge collection and absorption-limited sensitivity of x-ray photoconductors: Applications to a-Se and HgI2," Applied Physics Letters **80**, 1664-1666 (2002).

[43] W. Zhao, G. DeCrescenzo and J. A. Rowlands, "Investigation of lag and ghosting in amorphous selenium flat-panel x-ray detectors," Medical Imaging 2002: Physics of Medical Imaging, **4682**, pp. 9-20 (2002).

[44] J. G. Mainprize, N. L. Ford, S. Yin, T. O. Tumer, E. Gordon, W. J. Hamilton and M. J. Yaffe, "Semiconductor materials for digital mammography," Medical Imaging 2000: Physics of Medical Imaging, **3977**, pp. 152-158 (2000).

[45] D. R. Ouimette, S. Nudelman and R. S. Aikens, "New large-area x-ray image sensor," Medical Imaging 1998: Physics of Medical Imaging, **3336**, pp. 470-476 (1998).

[46] G. Juska and K. Arlauskas, "Impact Ionization and Mobilities of Charge-Carriers at High Electric-Fields in Amorphous Selenium," Physica Status Solidi a-Applied Research **59**, 389-393 (1980).

[47] K. Tsuji, Y. Takasaki, T. Hirai, J. Yamzaki and K. Tanioka, "Avalanche Phenomenon in Amorphous Selenium," OptoElectronics-Devices and Technologies **9**, 367-378 (1994).

[48] R. Luhta and J. A. Rowlands, "Feasibility of a large area x-ray sensitive vidicon for medical fluoroscopy: Resolution and lag factors," Medical Physics **24**, 621-631 (1997).

[49] S. Itoh and M. Tanaka, "Current status of field-emission displays," Proceedings of the IEEE, **90**, pp. 514-520 (2002).

[50] M. Nanba, Y. Hirano, Y. Honda, K. Kiyakawa, Y. Ookawa, T. Watabe, S. Okazaki, N. Egami, K. Miya, K. Nakamura, M. Taniguchi, S. Itoh and H. Kobayashi, "640X480 pixel HARP image sensor with active-matrix Spindt-type FEA," Procedings of 13th international Display Workshop, pp. 1817-1820 (2006).

[51] N. Negishi, Y. Matsuba, R. Tanaka, T. Nakada, K. Sakemura, Y. Okuda, A. Watanabe, T. Yoshikawa, K. Ogasawara, M. Nanba, S. Okazaki, K. Tanioka, N. Egami and N. Koshida, "Development of a high-resolution active-matrix electron emitter array for application to high-sensitivity image sensing," Journal of Vacuum Science & Technology B **25**, 661-665 (2007).

[52] W. Zhao, D. Li, A. Reznik, B. J. M. Lui, D. C. Hunt, J. A. Rowlands, Y. Ohkawa and K. Tanioka, "Indirect flat-panel detector with avalanche gain: Fundamental

feasibility investigation for SHARP-AMFPI (scintillator HARP active matrix flat panel imager)," Medical Physics **32**, 2954-2966 (2005).

[53] W. Zhao, D. Li, A. Reznik, B. Lui, D. C. Hunt, K. Tanioka and J. A. Rowlands, "Indirect flat-panel detector with avalanche gain: design and operation of the avalanche photoconductor," Medical Imaging 2005: Physics of Medical Imaging, **5745**, pp. 352-360 (2005).

[54] L. E. Antonuk, Y. El-Mohri, J. H. Siewerdsen, J. Yorkston, W. Huang, V. E. Scarpine and R. A. Street, "Empirical investigation of the signal performance of a high-resolution, indirect detection, active matrix flat-panel imager (AMFPI) for fluoroscopic and radiographic operation," Medical Physics **24**, 51-70 (1997).

[55] K. W. Jee, L. E. Antonuk, Y. El-Mohri and Q. H. Zhao, "System performance of a prototype flat-panel imager operated under mammographic conditions," Medical Physics **30**, 1874-1890 (2003).

[56] D. C. Hunt, B. Lui and J. A. Rowlands, "An Experimentally Validated Theoretical Model of Avalanche Multiplication X-ray Noise in Amorphous Selenium," Proc. SPIE, **3977**, pp. 106-116 (2000).

[57] A. Rose, "The sensitivity performance of the human eye on an absolute scale," Journal of the Optical Society of America **38**, 196-208 (1948).

[58] J. C. Danty, and Shaw, R, *Image Science, principle, anlyasis and evaluation of photographic-type imaging processing*. (Academic Press, 1974).

[59] J. Beutel, Harold L. Kundel, and Richard L. Van Metter *Handbook of Medical Imaging, Volume 1. Physics and Psychophysics*. (SPIE, 2000).

[60] R. F. Wagner and D. G. Brown, "Unified SNR analysis of medical imaging systems," Physics in Medicine and Biology **30**, 489-518 (1985).

[61] M. Kubota, T. Kato, S. Suzuki, H. Maruyama, K. Shidara, K. Tanioka, K. Sameshima, T. Makishima, K. Tsuji, T. Hirai and T. Yoshida, "Ultrahigh-sensitivity new Super-HARP camera," Ieee Transactions on Broadcasting **42**, 251-258 (1996).

[62] K. Tanioka, J. Yamazaki, K. Shidara, K. Taketoshi, T. Kawamura, T. Hirai and Y. Takasaki, "Avalanche-Mode Amorphous Selenium Photoconductive Target for Camera Tube," Advances in Electronics and Electron Physics **74**, 379-387 (1988).

[63] A. Reznik, B. J. M. Lui and J. A. Rowlands, "An amorphous selenium based positron emission mammography camera with avalanche gain," Technology in Cancer Research and Treatment, **4**, pp. 61-67 (2005).

[64] L. Onsager, "Deviations from Ohm's Law in Weak Electrolytes," The Journal of Chemical Physics **2**, 599-615 (1934).

[65] L. Onsager, "Initial recombination of ions," Physical Review **54**, 554-557 (1938).

[66] D. M. Pai and R. C. Enck, "Onsager mechanism of photogeneration in amorphous selenium," Physical Review B **11**, 5163-5174 (1975).

[67] K. K. Thornber, "Applications of scaling to problems in high-field electronic transport," Journal of Applied Physics **52**, 279-290 (1981).

[68] S. M. Sze, *Physics of Semiconductor Devices*, 2nd Edition ed. (John Wiley & Sons, New York, 1981).

[69] T. Ohshima, K. Tsuji, K. Sameshima, T. Hirai, K. Shidara and K. Taketoshi, "EXCESS NOISE IN AMORPHOUS SELENIUM AVALANCHE PHOTODIODES," Japanese Journal of Applied Physics Part 2-Letters **30**, L1071-L1074 (1991).

[70] S. Nitta, S. Takeuchi, K. Ogawa, T. Furukawa, T. Itoh and S. Nonomura, "Anomalous Reflectance in Random Amorphous Multilayers A-Si:H/$Si_{1-x}N_x$ and Classical Localization of Light," Journal of Non-Crystalline Solids / Proceedings of the Fourteenth International Conference on Amorphous Semiconductors-Science and Technology, **137-138 part 2**, pp. 1095-1098 (1991).

[71] K. Tsuji, Y. Takasaki, T. Hirai, J. Yamazaki and K. Tanioka, "Avalanche Phenomenon in Amorphous Selenium," OptoElectronics-Devices and Technologies **9**, 367-378 (1994).

[72] I. A. Cunningham and R. Shaw, "Signal-to-noise optimization of medical imaging systems," Journal of the Optical Society of America a-Optics Image Science and Vision **16**, 621-632 (1999).

[73] K. Rossmann, "Measurement of the Modulation Transfer Function of Radiographic Systems Containing Fluorescent Screens," Physics in Medicine and Biology **9**, 551-& (1964).

[74] K. Rossmann, "The spatial frequency spectrum: a means for studying the quality of radiographic imaging systems," Radiology **90**, 1-13 (1968).

[75] K. Rossmann, "Point spread-function, line spread-function, and modulation transfer function. Tools for the study of imaging systems " Radiology **93**, 257-272 (1969).

[76] J. C. Dainty and R. Shaw, *Image science: principles, analysis and evaluation of photographic-type imaging processes*. (Academic Press, New York, 1974).

[77] J. D. Gaskill., *Linear systems, Fourier transforms, and optics*. (John Wiley & Sons, New York, 1978).

[78] A. Papoulis, *Systems and transforms with applications in optics*. (McGraw-Hill, New York, 1968).

[79] K. Doi, K. Rossmann and A. G. Haus, "Image quality and patient exposure in diagnostic radiology," Photographic Science and Engineering **21**, 269-277 (1977).

[80] C. E. Metz and K. Doi, "Transfer function analysis of radiographic imaging systems," Physics in Medicine and Biology **24**, 1079-1106 (1979).

[81] H. H. Barrett and W. Swindell., *Radiological imaging :the theory of image formation, detection, and processing*. (Academic Press, New York, 1981).

[82] I. A. Cunningham, "Applied linear-system theory," in *Handbook of Medical Imaging*, *Vol. 1: Physics and Psychophysics,* edited by J. Beutel, H. L. Kundel and R. L. Van Metter (SPIE Press, Bellingham, 2000), pp. 79-160.

[83] G. Lubberts, "Random noise produced by x-ray fluorescent screens," Journal of the Optical Society of America **58**, 1475-1482 (1968).

[84] A. Koch, "Influence of optical gaps on signal and noise properties of luminescent screen x-ray detectors," Medical Imaging 2004: Physics of Medical Imaging, **5368**, pp. 221-225 (2004).

[85] D. C. Hunt, B. Lui and J. A. Rowlands, "Experimentally validated theoretical model of avalanche multiplication x-ray noise in amorphous selenium," Medical Imaging 2000: Physics of Medical Imaging, **3977**, pp. 106-116 (2000).

[86] R. Gomer, *Field Emission and Field Ionization*. (American Institute of Physics, New York City, 1993).

[87] R. H. Fowler and L. Nordheim, "Electron emission in intense electric fields," Proceedings of the Royal Society of London Series a-Containing Papers of a Mathematical and Physical Character, **119**, pp. 173-181 (1928).

[88] I. Brodie and C. A. Spindt, "Vacuum Microelectronics," Advances in Electronics and Electron Physics **83**, 1-106 (1992).

[89] R. D. Young, "Theoretical Total-Energy Distribution of Field-Emitted Electrons," Physical Review **113**, 110-114 (1959).

[90] G. Fursey, *Field Emission in Vacuum Microelectronics*. (Kluwer Academic / Plenum Publishers, New York, 2005).

[91] M. Nakamoto, "Advances in Field Emission Displays," XXIInd. International Symposium on Discharges and Electrical Insulation in Vacuum, 2006. ISDEIV '06. , **2**, pp. 871-874 (2006).

[92] H. Sato, H. Takegawa, H. Yamaji, H. Miyake, K. Hiramatsu and Y. Saito, "Fabrication of carbon nanotube array and its field emission property," Journal of Vacuum Science & Technology B **22**, 1335-1337 (2004).

[93] N. Koshida, T. Ozaki, X. Sheng and H. Koyama, "Cold Electron-Emission from Electroluminescent Porous Silicon Diodes," Japanese Journal of Applied Physics Part 2-Letters **34**, L705-L707 (1995).

[94] T. Komoda, T. Ichihara, Y. Honda, K. Aizawa and N. Koshida, "Ballistic Electron Surface-Emitting Cold Cathode by Porous Polycrystalline Silicon Film Formed on Glass Substrate," Materials Research Society Symposium Proceeding **638**, pp. page F4.1 (2000).

[95] K. Sakemura, N. Negishi, T. Yamada, H. Satoh, A. Watanabe, T. Yoshikawa, K. Ogasawara and N. Koshida, "Development of an advanced high efficiency electro-emission device," Journal of Vacuum Science & Technology B **22**, 1367-1371 (2004).

[96] C. A. Spindt, I. Brodie, L. Humphrey and E. R. Westerberg, "Physical-Properties of Thin-Film Field-Emission Cathodes with Molybdenum Cones," Journal of Applied Physics **47**, 5248-5263 (1976).

[97] S. Itoh, M. Tanaka and T. Tonegawa, "Development of field emission displays," Journal of Vacuum Science & Technology B **22**, 1362-1366 (2004).

[98] S. Itoh, M. Tanaka, T. Tonegawa, Y. Obara, Y. Naito, H. Kobayashi and Y. Sato, "Development of Field Emission Display," Proceedings of the 11th International Display Workshops, **1189-1192**, pp. (2004).

[99] Y. Takiguchi, M. Nanba, K. Osada, T. Watabe, S. Okazabi, N. Egami, K. Tanioka, M. Tanaka and S. Itoh, "256×192 pixel field emitter array image sensor with high-gain avalanche rushing amorphous photoconductor target," Journal of Vacuum Science & Technology B **22**, 1390-1395 (2004).

[100] A. R. Lubinsky, W. Zhao, G. Ristic and J. A. Rowlands, "Screen optics effects on detective quantum efficiency in digital radiography: Zero-frequency effects," Medical Physics **33**, 1499-1509 (2006).

[101] N. Egami, M. Nanba, Y. Takiguchi, K. Miyakawa, T. Watabe, S. Okazaki, K. Osada, Y. Obara, M. Tanaka and S. Itoh, "50×50 μm pixel magnetic focus field emitter array image sensor with high-gain avalanche rushing amorphous

photoconductor target," Journal of Vacuum Science & Technology B **23**, 2056-2062 (2005).

[102] R. P. Luhta, PH.D. Thesis, University of Toronto, 1997.

[103] B. Zhao and W. Zhao, "Temporal performance of amorphous selenium mammography detectors," Medical Physics **32**, 128-136 (2005).

[104] J. E. Gray, J. G. Stears, F. Lopez and M. A. Wondrow, "Fluoroscopic imaging - Quantitation of image lag or smearing," Radiology **150**, 563-567 (1984).

[105] J. H. Siewerdsen and D. A. Jaffray, "A ghost story: Spatio-temporal response characteristics of an indirect-detection flat-panel imager," Medical Physics **26**, 1624-1641 (1999).

[106] P. R. Granfors, R. Aufrichtig, G. E. Possin, B. W. Giambattista, Z. S. Huang, J. Liu and B. Ma, "Performance of a 41 x 41 cm[sup 2] amorphous silicon flat panel x-ray detector designed for angiographic and R&F imaging applications," Medical Physics **30**, 2715-2726 (2003).

[107] D. C. Hunt, O. Tousignant and J. A. Rowlands, "Evaluation of the imaging properties of an amorphous selenium-based flat panel detector for digital fluoroscopy," Medical Physics **31**, 1166-1175 (2004).

[108] M. Overdick, T. Solf and H.-A. Wischmann, "Temporal artifacts in flat dynamic x-ray detectors," Medical Imaging 2001: Physics of Medical Imaging, **4320**, pp. 47-58 (2001).

[109] A. Rose, *Concepts in Photoconductivity and Allied Problems*. (Interscience Publishers, New York, 1963).

[110] W. Zhao and J. A. Rowlands, "X-ray imaging using amorphous selenium: Feasibility of a flat panel self-scanned detector for digital radiology," Medical Physics **22**, 1595-1604 (1995).

[111] W. D. Park and K. Tanioka, "Avalanche-type high sensitive image pickup tube using an a-Se photoconductive target," Japanese Journal of Applied Physics Part 2-Letters **42**, L209-L211 (2003).

[112] R. H. Good and E. W. Muller, *Field Emission*. (Springer-Verlag, Berlin, 1956).

[113] L. J. v. d. Polder, "Target-Stabilization Effects in Television Pick-up Tubes," Philips Research Reports **22**, 178-207 (1967).

[114] D. Li and W. Zhao, "SAPHIRE (scintillator avalanche photoconductor with high resolution emitter readout) for low dose x-ray imaging: Spatial resolution," Medical Physics **35**, 3151-3161 (2008).

[115] B. Meltzer and P. L. Holmes, "Beam Temperature, Discharge Lag and Target Biasing in Some Television Pick-up Tubes," British Journal of Applied Physics **9**, 139-143 (1958).

[116] J. M. Sandrik, *The video camera for medical imaging*. (AIP, New York, 1984).

[117] O. Yoshida and Y. Kiuchi, "Calculations of Image Lag in Vidicon-Type Camera Tubes .1. Beam Discharge Lag and Total Image Lag, Including Photoconductive Lag," Japanese Journal of Applied Physics **10**, 1203-& (1971).

[118] R. D. Young and E. W. Muller, "Experimental Measurement of the Total-Energy Distribution of Field-Emitted Electrons," Physical Review **113**, 115-120 (1959).

[119] L. W. Swanson and L. C. Crouser, "Total-Energy Distribution of Field-Emitted Electrons and Single-Plane Work Functions for Tungsten," Physical Review **163**, 622-& (1967).

[120] D. Li and W. Zhao, "SAPHIRE (Selenium Avalanche Photoconductor with High Resolution Emitter readout): Investigation of Parallel Beam Readout," RSNA annual meeting, pp. pp 270 (2007).

[121] N. Negishi, R. Tanaka, T. Nakada, K. Sakemura, Y. Okuda, H. Satoh, A. Watanabe, T. Yoshikawa, K. Ogasawara, M. Nanba, S. Okazaki, K. Tanioka, N. Egami and N. Koshida, "Fabrication of active-matrix high-efficiency electron emission device and its application to high-sensitivity image sensing," Journal of Vacuum Science & Technology B **24**, 1021-1025 (2006).

[122] J. T. Dobbins, D. L. Ergun, L. Rutz, D. A. Hinshaw, H. Blume and D. C. Clark, "Dqe(F) of 4 Generations of Computed Radiography Acquisition Devices," Medical Physics **22**, 1581-1593 (1995).

[123] H. Lai and A. Cunningham, "Noise aliasing in interline-video-based fluoroscopy systems," Med Phys **29**, 298-310 (2002).

[124] D. Li and W. Zhao, "SAPHIRE (Scintillator Avalanche Photoconductor with High Resolution Emitter readout) for low dose x-ray imaging: lag," Submitted to Medical Physics (2008).

[125] J. Itoh, Y. Tohma, K. Morikawa, S. Kanemaru and K. Shimizu, "Fabriaction of Double-Gated Si Field Emitter Arrays for Focused Electron-Beam Generation," Journal of Vacuum Science & Technology B **13**, 1968-1972 (1995).

[126] N. Negishi, T. Chuman, S. Iwasaki, T. Yoshikawa, H. Ito and K. Ogasawara, "High efficiency electron-emission in Pt/SiOx/Si/Al structure," Japanese Journal of Applied Physics Part 2-Letters **36**, L939-L941 (1997).

[127] N. Negishi, T. Sato, Y. Matsuba, R. Tanaka, T. Nakada, K. Sakemura, Y. Okuda, A. Watanabe, T. Yoshikawa, K. Ogasawara, M. Nanba, S. Okazaki, K. Tanioka, N. Egami and N. Koshida, "Development of a super-high-sensitivity image sensor using 640x480 pixel active-matrix high-efficiency electron emission device," Journal of Vacuum Science & Technology B **26**, 711-715 (2008).

Appendix

Appendix A: derivation of avalanche gain g_{av}

We already have

$$M(x) = 1 + \int_0^x \alpha M(y)dy + \int_x^L \beta M(y)dy \,. \tag{2.01}$$

We may differentiate Eq. 2.01 and obtain

$$\frac{dM(x)}{dx} = (\alpha - \beta)M(x) \,. \tag{A.01}$$

Its solutions is

$$M(x) = M(0)\exp\left(\int_0^x (\alpha - \beta)dy\right). \tag{A.02}$$

or

$$M(x) = M(L)\exp\left(-\int_x^L (\alpha - \beta)dy\right). \tag{A.03}$$

Substitute Eq. A.03 into Eq. 2.01 and let $x = L$, we obtain

$$M(L) = \frac{1}{1 - \int_0^L \alpha \exp\left(-\int_x^L (\alpha - \beta)dy\right)dx} \,. \tag{A.04}$$

Substitute Eq. A.04 back to Eq. A.03 and simplify it, we get $M(x)$ as Eq.2.03:

$$M(x) = \frac{(\beta - \alpha)e^{((\beta-\alpha)(L-x))}}{\beta - \alpha e^{(\beta-\alpha)L}} \,. \tag{2.03}$$

According to Lambert-Beers law $N = N_0 e^{-\mu x}$, where μ is the linear attenuation coefficient for *a*-Se, the number of photons absorbed in a layer with depth of x and thickness of Δx is given by

$$\Delta N = -\frac{dN}{dx}\Delta x = \mu N_0 e^{-\mu x}\Delta x . \qquad \text{(A.05)}$$

And the total absorbed photons is given by

$$N_T = N_0(1-e^{-\mu L}) . \qquad \text{(A.06)}$$

The final overall avalanche gain, g_{av}, is the weighted avalanche multiplication $M(x)$ at different depths:

$$g_{av} = \frac{\int_0^L M(x)dN}{N_T} = \frac{\int_0^L M(x)\mu N_0 e^{-\mu x}dx}{N_0(1-e^{-\mu L})} . \qquad \text{(A.07)}$$

Then Eq. 2.07 can be simplified into the form of Eq. 2.04. Here we suppose that photons are coming from the side of $x = 0$. If photons enter from the side of $x = L$, we have

$$g'_{av} = \frac{\int_0^L M(L-x)dN}{N_T} = \frac{\int_0^L M(L-x)\mu N_0 e^{-\mu x}dx}{N_0(1-e^{-\mu L})} , \qquad \text{(A.08)}$$

which is simplified to

$$g'_{av} = \frac{\mu(\beta-\alpha)(e^{\mu L}-e^{(\beta-\alpha)L})}{(\mu+\beta-\alpha)(e^{\mu L}-1)(\beta-\alpha e^{(\beta-\alpha)L})} . \qquad \text{(A.09)}$$

Appendix B: The electron trajectory and lateral spread for mesh-electrode-only design

In this appendix, the trajectory of the electrons and the resulting lateral spread is derived for the mesh-electrode-only design. The lateral spread is the product of the lateral component of the electron velocity, v_x and the time it takes the electron to travel from the gate to the HARP target, t_{gt}. The electrons were assumed to have an initial kinetic energy of $KE_0 = qV_g$ after emission from the gate electrode with an angle of θ (respect to z-axis), hence v_x is given by:

$$v_x = \sqrt{\frac{2qV_g}{m}} \sin\theta \,, \tag{B.01}$$

where m is the mass of an electron. Since the electric field is in the z direction, v_x remains unchanged as the electrons travel to the target. The potential $V(z)$ and the axial velocity component $v_z(z)$ change as functions of position z (z = 0 at gate electrode). The value of t_{gt} is given by the sum of the time it takes to travel from the gate to the mesh electrode, t_{gm}, and from the mesh electrode to the target, t_{mt}:

$$t_{gt} = t_{gm} + t_{mt} = \frac{v_z(L_{gm}) - v_z(0)}{a_{gm}} + \frac{v_z(L_{gm}) - v_z(L_{gt})}{a_{mt}} \tag{B.02}$$

where $a_{gm} = \frac{V_m - V_g}{L_{gm}} \times \frac{q}{m}$ is the electron acceleration between the gate and the mesh and $a_{mt} = \frac{V_m - V_t}{L_{mt}} \times \frac{q}{m}$ is the deceleration between the mesh and the target. Using energy conservation, i.e. $\frac{1}{2} m \left(v_z(z)^2 + v_x{}^2 \right) = qV(z)$, we can obtain:

$$v_z(z) = \sqrt{\frac{2qV(z)}{m} - \frac{2qV_g}{m} \sin^2\theta} \,. \tag{B.03}$$

By substituting $v_z(L_{gm})$ and $v_z(L_{gt})$ into Eq. B.02, t_{gt} can be obtained using:

$$
\begin{aligned}
t_{gt} &= t_{gm} + t_{mt} \\
&= \frac{L_{gm}}{V_m - V_g}\sqrt{\frac{2m}{q}}\left(\sqrt{V_m - V_g \sin^2\theta} - \sqrt{V_g}\cos\theta\right) \\
&+ \frac{L_{mt}}{V_m - V_t}\sqrt{\frac{2m}{q}}\left(\sqrt{V_m - V_g \sin^2\theta} - \sqrt{V_t - V_g \sin^2\theta}\right)
\end{aligned}
\quad . \qquad \text{(B.04)}
$$

Thus the x and z location of an electron at any time t is given by

$$
x = v_x \times t\,, \qquad \text{(B.05)}
$$

and

$$
\begin{aligned}
z &= v_z(0)t + \frac{1}{2}a_{gm}t^2 \\
&= t\sqrt{\frac{2eV_g}{m}}\cos\theta + \frac{V_m - V_g}{2L_{gm}} \times \frac{q}{m}t^2
\end{aligned}
\qquad \text{when } t > t_{gm}
$$

$$
\begin{aligned}
z &= L_{gm} + v_z(L_{gm})(t - t_{gm}) + \frac{1}{2}a_{mt}(t - t_{gm})^2 \\
&= L_{gm} + (t - t_{gm})\sqrt{\frac{2qV_m}{m} - \frac{2qV_g}{m}\sin^2\theta} + \frac{V_m - V_t}{2L_{mt}} \times \frac{q}{m}(t - t_{gm})^2
\end{aligned}
\qquad \text{when } t > t_{gm}
$$

(B.06)

The final lateral spread is given by $x(t = t_{gt})$ as:

$$
\begin{aligned}
LS &= v_x \times t_{gt} \\
&= 2\sqrt{V_g}\sin\theta \cdot L_{gm}\left(\frac{\sqrt{V_m - V_g \sin^2\theta} - \sqrt{V_g}\cos\theta}{V_m - V_g}\right) \\
&+ 2\sqrt{V_g}\sin\theta \cdot L_{mt}\left(\frac{\sqrt{V_m - V_g \sin^2\theta} - \sqrt{V_t - V_g \sin^2\theta}}{V_m - V_t}\right)
\end{aligned}
\quad . \qquad \text{(B.07)}
$$

The lateral spread increases as θ increases while the other factors are kept constant. The condition for electrons to reach the target is $v_z \geq 0$ at $z = L_{gt}$. The critical θ_c occurs when $v_z = 0$. Thus Eq. B.03 can be simplified to:

$$\sin\theta_c = \sqrt{\frac{V_t}{V_g}}. \tag{B.08}$$

The maximum lateral spread (LS_{max}) can be obtained by substituting Eq. B.08 into Eq. B.07:

$$LS_{\max} = 2\sqrt{V_t}\cdot L_{gm}\left(\frac{\sqrt{V_m - V_t} - \sqrt{V_g - V_t}}{V_m - V_g}\right) + 2\sqrt{V_t}\cdot L_{mt}\left(\frac{1}{\sqrt{V_m - V_t}}\right) \tag{B.09}$$

Appendix C: The electron trajectory and lateral spread for magnetic focusing design

In this appendix, the trajectory of the electrons and the resulting lateral spread is derived for the magnetic focusing design. Since the magnetic field only changes the direction of v_x, the travel time t_{gt} and the location $z(t)$ are the same as in Eqs. B.02 and B.06, respectively. The spiral trajectory of the electron is projected to a circle in the x-y plane, which has a radius of $r_B = \frac{mv_x}{qB}$ and an angular velocity of $\omega = \frac{qB}{m}$. Thus the lateral spread is given by the chord of the circle from the starting to the finishing point of the trajectory. The trajectory can be translated from the Cartesian coordinate system (x, y, z) to a cylindrical coordinate system (r, ψ, z). The lateral component, r, at any time t, is given by:

$$r = 2r_B\left|\sin\left(\frac{\omega t}{2}\right)\right| = \frac{2}{B}\sqrt{\frac{2mV_g}{q}}\sin\theta\cdot\left|\sin\left(\frac{qBt}{2m}\right)\right|. \tag{C.01}$$

The final lateral spread is given by $r(t = t_{gt})$ as:

$$LS = 2r_B\left|\sin\left(\frac{\omega t}{2}\right)\right| = \frac{2}{B}\sqrt{\frac{2mV_g}{q}}\sin\theta\cdot\left|\sin\left(\frac{qBt_{gt}}{2m}\right)\right|. \tag{C.02}$$

Appendix D: The energy spread due to the angular distribution of emitted electrons

If we assume the same kinetic energy of qV_g for all the emitted electrons when they pass through the gate electrode [99], only the electrons with smaller emission angles (i.e., higher v_z) can reach the target. Therefore there exists a critical emission angle θ_C, within which all the emitted electrons can reach the target [99]. The accepted electron beam current, I_a, can be obtained by integrating the emitted beam intensity up to θ_C:

$$I_a = N\int_0^{2\pi}\int_0^{\theta_C} I(\theta)\sin\theta d\theta d\varphi = 2\pi N\int_0^{\theta_C} I(\theta)\sin\theta d\theta \qquad \text{(D.01)}$$

where N is a normalization factor to ensure $I_a = I_e$ when all electrons are collected. We also have

$$I_a = \int_{qV_g\cos^2\theta_C}^{qV_g} P_z(E_z)dE_z\ , \qquad \text{(D.02)}$$

where $E_z = qV_g\cos^2\theta$ is the axial (vertical) kinetic energy. Since $dE_z = -2qV_g\sin\theta\cos\theta d\theta$, Eqs. D.01 and D.02 can be combined to obtain:

$$P(E_z) = N_0\frac{I(\theta)}{\cos\theta}, \qquad \text{(D.03)}$$

where $N_0 = \dfrac{\pi N}{qV_g}$.